

1 a Coriolis tutorial, Part 4:
2 Wind-driven ocean circulation; the Sverdrup relation

3 James F. Price

4 Woods Hole Oceanographic Institution,
5 Woods Hole, Massachusetts, 02543

6 <https://www2.whoi.edu/staff/jprice/> jprice@whoi.edu

7 Version 7 23rd Nov, 2020 at 09:44

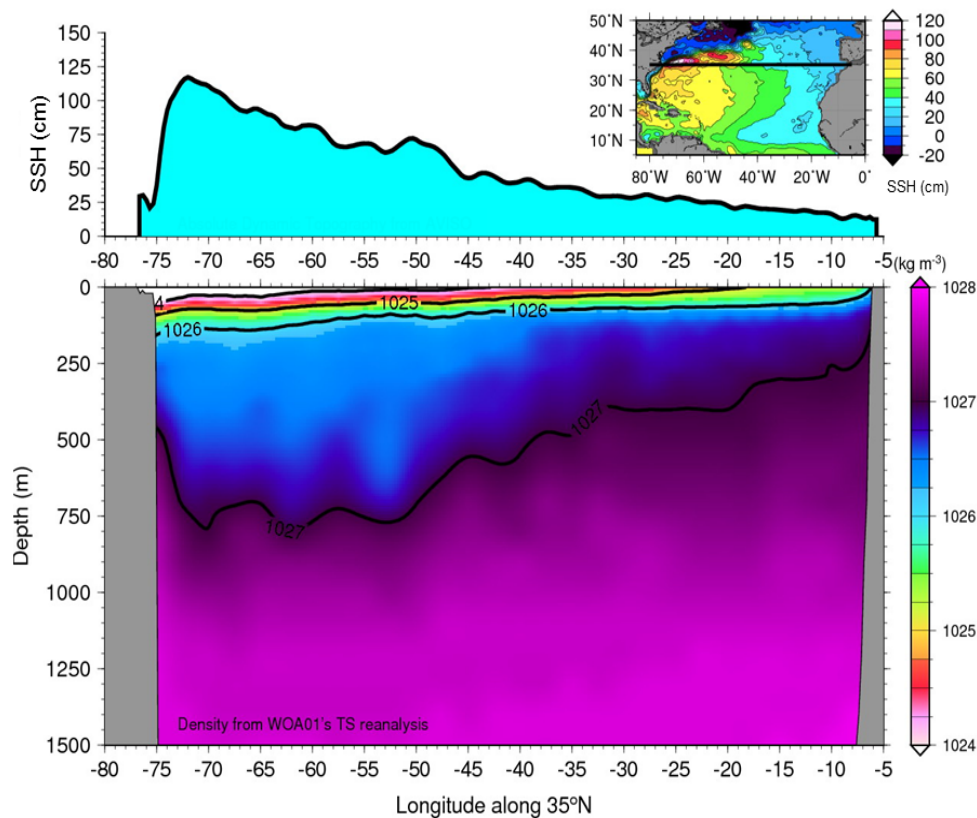


Figure 1: A zonal section through the thermocline of the North Atlantic subtropical gyre viewed toward the north. **(upper)** Sea surface height (SSH) from satellite altimetry. **(lower)** Potential density from *in situ* observations. This section shows the remarkable zonal asymmetry that is characteristic of all of the major, upper ocean gyres. Within a narrow western boundary region, longitude -76 to -72, the SSH slope is positive and very large, and the inferred geostrophic current is northward and very fast: the Gulf Stream. Over the rest of the basin, the SSH slope is negative and much, much smaller. The inferred geostrophic flow is southward and correspondingly very slow. This southward flow is at least roughly consistent with the overlying, negative wind stress curl and the Sverdrup relation, the central topic of this essay.

8 **Abstract.** This essay is the fourth of a four part introduction to Earth's rotation and the fluid dynamics
9 of the atmosphere and ocean. The theme is wind-driven ocean circulation, and the motive is to develop
10 insight for several major features of the observed ocean circulation, *viz.* western intensification of upper
11 ocean gyres and the geography of the mean and the seasonal variability. A key element of this insight is
12 an understanding of the Sverdrup relation between wind stress curl and meridional transport. To that end,
13 shallow water models are solved for the circulation of a model ocean that is started from rest and driven
14 by a specified wind stress field: westerlies at mid-latitudes and easterlies in subpolar and tropical regions.
15 This gives three regions of stress curl, negative over the subtropics, and positive over subpolar and
16 tropical regions.

17 The model described first and used most extensively has just one active layer and makes the reduced
18 gravity approximation. This is essentially the model used in Parts 2 and 3 and is here dubbed 1l-rg. The
19 dynamics of this model are thus baroclinic only. The second model includes three active layers, including
20 a thick, active abyssal layer and a free sea surface and hence, 3l-fs. This more complete model includes
21 the baroclinic dynamics of the 1l-rg model as well as fast, barotropic dynamics.

22 **Baroclinic response in the 1l-rg solution.** The developing baroclinic circulation can be described in
23 terms of four stages. Stage 1 is the direct, local response to the imposed wind stress and includes
24 inertia-gravity oscillations and Ekman transport within the upper, surface layer. The inertial-gravity
25 oscillations die away after a couple of weeks with no evident lasting effect. The Ekman transport remains,
26 and is very consequential for the long term ocean circulation. Ekman transport varies spatially on account
27 of the latitudinal variation of the wind stress and of the Coriolis parameter, f . The resulting divergence of
28 Ekman transport modifies the thickness of the upper layer field and thus the mass field, the pressure field,
29 and hence the circulation. Over the central subtropics, where wind stress curl is negative, the Ekman
30 transport is convergent, which leads to a slowly thickening thermocline (about 30 meters per year in the
31 central subtropics) and a high pressure in the upper ocean. This induces a nearly geostrophic zonal
32 circulation which increases in step with the thickness field. This local response to wind stress curl is
33 called the Stage 2 response, and goes on for about three years until the slow westward, Rossby-wave like
34 propagation ($-\beta R_d^2 = -3 \text{ km day}^{-1}$ in the subtropics) of the zonal thickness gradient balances Ekman
35 convergence and gives a steady state thickness. The steady circulation is then a baroclinic Sverdrup flow,
36 dubbed Stage 3. The transition from Stage 2 to Stage 3 sweeps westward across the basin, just like the
37 westward propagation of a long baroclinic Rossby wave emanating from the eastern boundary. Baroclinic
38 Sverdrup flow thus occurs much sooner in the tropics (months) than in the subpolar region (decades).

39 The central subtropical gyre reaches steady-state Sverdrup flow in about three years, but the layer
40 thickness continues to increase very slowly and uniformly (spatially) over the next several decades as the
41 subtropical gyre absorbs water expelled from the subpolar region where the wind stress curl is positive
42 and the upper layer becomes dramatically thinner. A basin-wide steady state, Stage 4, arises only after
43 the subpolar gyre has also been swept by a slowly moving long baroclinic Rossby wave. Along the

44 northern boundary of the 1l-rg model, that requires about 30 years.

45 The observed, basin-scale horizontal structure of the wind-driven ocean circulation, including
46 western intensification and several of the qualitative differences between tropical, subtropical and
47 subpolar gyres, have a plausible analog in solutions of the baroclinic shallow water model. In particular,
48 the Sverdrup relation plus the observed pattern of wind stress curl provide a concise and convincing
49 explanation of the sense of the circulation over the majority of an ocean basin, e.g., equatorward
50 (southward) meridional flow in the subtropics of the North Atlantic, where the wind stress curl is
51 negative, and the opposite sign in the tropical and subpolar regions. The Sverdrup relation is valid where
52 the dominant terms of the potential vorticity balance are just two: the beta effect acting on a slow
53 meridional flow, and the curl of the wind stress. In practice, this holds in the interior of a basin, where the
54 currents and the friction are both very weak, and well away from zonal or meridional boundaries.

55 The net transport through any given basin-wide zonal section must vanish in steady state, and the
56 meridional Sverdrup transport in the interior of the basin is balanced in this volumetric sense by a very
57 intense western boundary current (wbc) having a width of order the baroclinic radius of deformation,
58 $O(100 \text{ km})$ in the subtropics. The baroclinic transport of a wbc reaches approximate steady state after the
59 ocean interior to the east of the wbc has reached steady baroclinic Sverdrup flow, about five years in the
60 subtropical gyre. In that sense, the wbc follows the interior circulation, despite that it is far more
61 energetic.

62 The meridional transport must vanish on zonal boundaries, and in the present model the affected
63 zonal boundary regions are fairly wide, up to 1000 km in north-south extent. Within these wide zonal
64 boundary regions, the meridional transport has the sign of the expected Sverdrup transport, but
65 considerably reduced amplitude, going to zero on the boundary.

66 Experiments with an annually-varying zonal wind stress show that the baroclinic wbc transport
67 responds only weakly to even a large, $\pm 50\%$ annual cycle of the wind stress. In the subtropical gyre, the
68 resulting annual cycle of baroclinic wbc transport is only about $\pm 4\%$ of the mean transport. The annual
69 cycle of wbc transport is even less in the subpolar gyre, and somewhat greater though still not prominent
70 in the tropical gyre. There are some specific regions that do show an appreciable, baroclinic response to
71 an annually varying wind stress, most notably the eastern half of the tropical gyre. There the annual cycle
72 of upper ocean (baroclinic) zonal currents is about $\pm 50\%$ of the mean, or roughly proportional to the
73 wind stress variation. This vigorous seasonal cycle of tropical zonal currents appears to be a mainly local
74 response to the seasonal variation of stress curl, here called Stage 2, but includes a contribution from an
75 annual period, eastern boundary Rossby wave.

76 **A barotropic and then a baroclinic response, 3l-fs.** What happens when the same start up experiment
77 is carried out with the three layer, free surface model, 3l-fs? In one key respect the results are strikingly
78 different from that described above, *viz.*, the circulation comes to a nearly steady, *barotropic* Sverdrup
79 flow within just a few weeks, even at subpolar latitudes. The comparatively very short response time of

80 the barotropic circulation is consistent with the very fast zonal propagation of barotropic long Rossby
81 waves, about $-1200 \text{ km day}^{-1}$ at 30 N. The basin-scale pattern of the barotropic transport, including the
82 western boundary currents and the zonal boundary regions, is very similar to that of the baroclinic
83 Sverdrup flow found in the 1l-rg model solution described above. This barotropic Sverdrup transport is
84 almost depth-independent (as barotropic usually implies) and thus occurs mainly within the thick, abyssal
85 layer. Consequently the amplitude of upper ocean currents and the SSH anomaly associated with the
86 barotropic response are quite small compared to the observed SSH, for example.

87 Over the following several years, a baroclinic adjustment occurs in the 3l-fs model solution in just
88 the way it does in the 1l-rg solution. In the central subtropical gyre, a first mode, long baroclinic Rossby
89 wave arrives from the east after about three years. As it passes, the abyssal layer comes to rest, and the
90 Sverdrup transport is thereafter confined to the two upper ocean layers, i.e., it is baroclinic. After about
91 another five years and the passage of a second mode wave, the Sverdrup transport is extinguished in the
92 unforced, lower thermocline layer and thereafter is present only in the uppermost, wind-forced layer. The
93 amplitude of the across-basin SSH anomaly is then fairly realistic, about 1 m across the subtropical gyre.
94 In all, the results from the 3l-fs model make a good case for the reduced gravity assumption, which takes
95 a quiescent abyssal layer for granted.

96 **More on Fig. 1** The SSH data in the upper panel are the monthly average for September over about
97 twenty years of measurement compiled by the AVISO Project (<https://www.aviso.altimetry.fr>). The lower
98 panel is the long-term, September average of density along 35°N from the World Ocean Atlas 2001
99 (http://www.nodc.noaa.gov/OC5/WOA01/pr_woa01.html). Notice that the tilt of the thermocline mirrors
100 the tilt of SSH so that high SSH corresponds to a thick, low density upper layer (this occurs also within
101 the narrow western boundary region, which is not resolved in this climatology). The net result of this
102 mass distribution is a comparatively small horizontal gradient of hydrostatic pressure at depths of about
103 1500 meters. This is suggestive of a reduced gravity approximation that will be utilized in many of the
104 numerical experiments to follow. At greater depths, there are cold, mainly southward flowing currents
105 that constitute the lower limb of the meridional overturning circulation. This figure was kindly provided
106 by Iam-Fei Pun of WHOI.

107 **Contents**

108 **1 Earth’s rotation and its effects upon large-scale flows** **7**

109 1.1 Two observed properties of the upper ocean circulation 7

110 1.1.1 O1, Space scales: Upper ocean gyres are markedly asymmetric east to west 7

111 1.1.2 O2, Time scales: The subtropical gyre is remarkably steady, while tropical circu-
112 lation shows large amplitude seasonal variation 9

113 1.2 The premise and the plan 10

114 1.3 A brief review of the Coriolis force, and the beta effect* 13

115 1.4 Aspects of depth-dependence* 16

116 **2 Shallow water models of wind-driven circulation** **20**

117 2.1 Boundary and initial conditions 20

118 2.2 Wind stress and its curl 21

119 2.3 An expedient parameterization of drag on ocean currents* 24

120 2.4 Momentum and vorticity balances 25

121 2.5 Models of stratification and pressure 26

122 2.5.1 Single layer, reduced gravity model, 1l-rg 26

123 2.5.2 Three layer, free surface model, 3l-fs 26

124 2.6 Understanding the Sverdrup relation; models, models, models* 31

125 **3 The baroclinic circulation of the 1l-rg solution develops in four stages** **32**

126 3.1 Stage 1: Short time, local response of the surface layer 32

127 3.1.1 Inertial oscillations* 35

128 3.1.2 Ekman currents and Ekman transport 36

129 3.2 Stage 2: Zonal geostrophic currents 37

130 3.2.1 Divergent Ekman transport changes the mass field 37

131 3.2.2 Geostrophic currents accompany the changing stratification 39

132 3.3 Stage 3: Blocking by the meridional boundaries and the onset of Sverdrup flow 42

133 3.3.1 Sverdrup flow in the basin interior 43

134 3.3.2 Western boundary currents 45

135 3.3.3 Changing stratification* 48

136 3.3.4 A simple model of transport in a time-dependent wbc* 50

137 3.4 Stage 4: Intra- and inter-gyre exchange, and basin-wide steady state 51

138	4 The (almost) steady circulation	52
139	4.1 A streamfunction depiction of the circulation	53
140	4.2 Dynamics of the steady circulation: the balance of potential vorticity	55
141	4.2.1 Sverdrup interior	56
142	4.2.2 Western boundary currents	58
143	4.2.3 Zonal boundary regions	60
144	4.3 A trip around the subtropical gyre	62
145	4.3.1 Momentum balance and energy exchanges	64
146	4.3.2 Potential vorticity balance	66
147	4.3.3 Depth dependence*	66
148	4.4 Another way to view the Sverdrup relation	68
149	5 Experiments with other wind fields and basin configurations	69
150	5.1 Annually-varying winds and circulation	70
151	5.2 A stress field with no curl*	73
152	5.3 Meridional winds over a basin without sidewalls (a channel)*	74
153	6 Barotropic and baroclinic circulation of the three layer, free surface model, 3l-fs	77
154	6.1 Inertial motion and Ekman transport in the surface layer	79
155	6.2 Transient, barotropic flows	79
156	6.3 Basin scale circulation; barotropic Sverdrup flow	84
157	6.4 Baroclinic adjustment to a surface intensified, steady state	85
158	7 Summary and closing remarks	87
159	7.1 O1: East-west asymmetry of the subtropical and subpolar gyres	87
160	7.2 O2: Time scales of the wind-driven circulation	90
161	7.3 What's gone missing?	93
162	7.4 Acknowledgements	94
163	8 Supplemental material	94
164	8.1 Links to models and updated manuscripts	94
165	8.2 Homework problems	95
166	9 Index	97

167 **1 Earth's rotation and its effects upon large-scale flows**

168 This essay is the fourth in a four-part introduction to fluid dynamics on a rotating Earth. These essays
 169 were written for students who have some background in classical fluid dynamics, and who are beginning
 170 a study of geophysical fluid dynamics (GFD).

171 Earth's rotation gives rise to some of the most distinctive, important and subtle phenomena of GFD.
 172 The first three of essays introduced the Coriolis force in Part 1, geostrophic adjustment in Part 2, and
 173 westward propagation in Part 3. These topics are about equally relevant for students of atmospheric and
 174 oceanographic science. The present essay continues the study of rotation effects, but now with an
 175 avowedly oceanic theme — wind-driven ocean circulation.

176 **1.1 Two observed properties of the upper ocean circulation**

177 The motive for this essay comes from two important, observed properties of the upper ocean circulation
 178 evident in Figs. (1) and (2): quasi-steady horizontally rotating gyres that fill the subpolar and subtropical
 179 basins, and zonally elongated, seasonally-varying SSH features that span the tropics (Fig. 2).

180 **1.1.1 O1, Space scales: Upper ocean gyres are markedly asymmetric east to west**

181 SSH sampled along 35° N across the subtropical gyre in Fig. (1) shows two distinctly different regions of
 182 SSH zonal slope, $\partial\eta/\partial x$ (Fig. 1, upper and Fig. 2). Going from the western boundary toward the east,
 183 there is a narrow region adjacent to the western boundary of width L_{wb} that is $O(100 \text{ km})$ within which
 184 the SSH increases eastward to a maximum $\delta\eta \approx 1 \text{ m}$. The inferred geostrophic current in this western
 185 boundary current, the Gulf Stream, is poleward (northward) and comparatively swift, $U_{wb} \approx g\delta\eta/(L_{wb}f)$
 186 is $O(1 \text{ m sec}^{-1})$. To the east, there is a broad interior region, essentially all the rest of the basin, width
 187 $L_i \approx 7000 \text{ km}$, over which there is a gradual decrease of η to approx. zero on the eastern boundary. The
 188 inferred geostrophic current in the interior is equatorward (southward) and very slow compared to the the
 189 western boundary current, $U_i \approx U_{wb}L_{wb}/L_i$ is $O(0.01 \text{ m sec}^{-1})$ when averaged over zonal scales of
 190 $O(1000 \text{ km})$. This slow southward flow is mainly wind-driven Sverdrup flow, about which much more
 191 below.

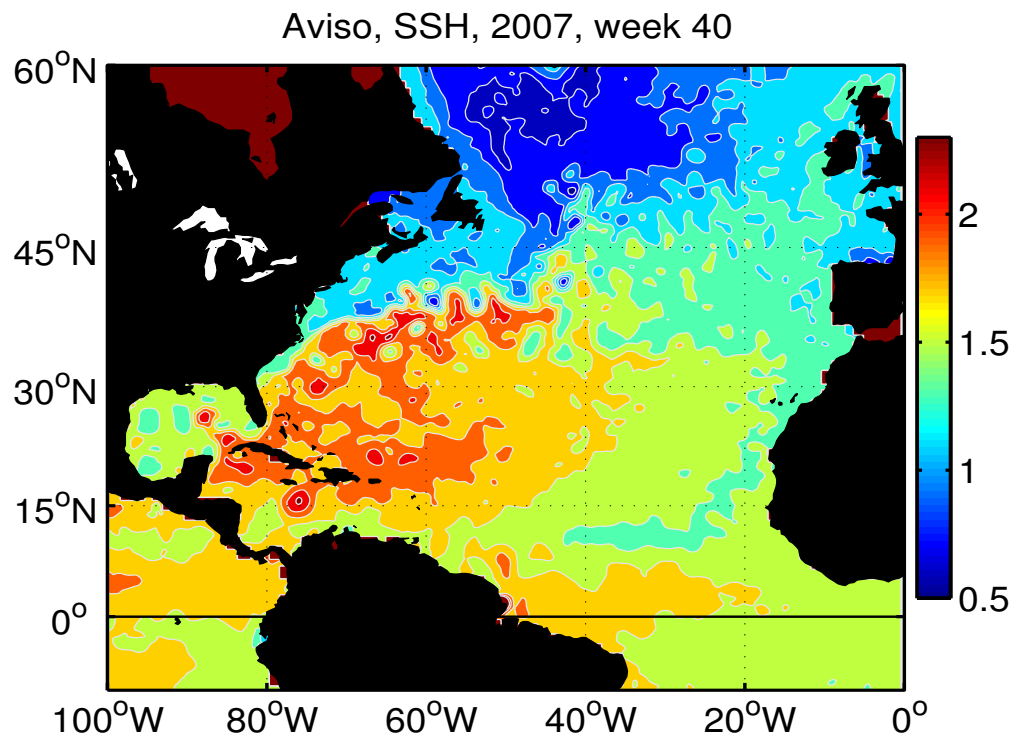


Figure 2: A snapshot of sea surface height (SSH) over the North Atlantic (repeats Fig. 1 of Part 3). The color scale at right is in meters. The largest SSH variability occurs primarily on two spatial scales — basin scale gyres (thousands of kilometers), a clockwise rotating high in the subtropics and a counter clockwise rotating low in the subpolar basin — and mesoscale eddies (several hundred kilometers) that are both highs and lows. The subtropical and subpolar gyres are clearly present in both instantaneous and time-averaged views, while mesoscale eddies are significantly time-dependent, including marked westward propagation. An animation of a year of this data is available at www.whoi.edu/jpweb/Aviso-NA2007.flv and see also the AVISO homepage: <https://www.aviso.altimetry.fr>

192 A similar structure of rapid western boundary current and much slower interior flow is found also in
 193 the subpolar gyre, though with the sense of the SSH anomaly and the circulation reversed. From this it is
 194 evident that the east-west asymmetry of wind-driven circulation, often called western intensification, is
 195 very pronounced, $L_i/L_{wb} \approx U_{wb}/U_i$ is $O(50)$, which is typical of all of the major upper ocean gyres.

196 **1.1.2 O2, Time scales: The subtropical gyre is remarkably steady, while tropical circulation**
197 **shows large amplitude seasonal variation**

198 The subtropical gyre is always present in the sense that every basin-wide snapshot of SSH (as in Fig. 2)
199 and every across-basin hydrographic section (as in Fig. 1 lower) will show an easily recognizable,
200 poleward-flowing Gulf Stream near the western boundary and an equatorward Sverdrup flow over most
201 of the rest of the basin. Said a little differently, the subtropical gyre and its wbc are evident on long-term
202 average and instantaneously. This holds just as well for the subpolar gyre (with signs reversed). The
203 systematic, annual variation of the subtropical gyre, often represented by the Gulf Stream transport, is
204 only about 5% of the time-mean.¹ Such a small annual variation is somewhat surprising, given that the
205 wind stress and air-sea heat flux over the North Atlantic exhibit a substantial annual variation, up to
206 $\pm 50\%$ in the northern North Atlantic. This implies that the response time of the gyre-scale circulation of
207 the subtropical and higher latitudes to a time-changing wind stress is considerably longer than a year.²

208 Tropical ocean circulation appears to be markedly different in both respects. Tropical SSH is
209 characterized by one or several narrow, zonally elongated ridges and troughs. The associated, zonal
210 geostrophic currents have alternate signs, e.g., between about 20 °N and 10 °N a westward flowing North
211 Equatorial Current, a little further south an eastward flowing North Equatorial Countercurrent, and still
212 further south, a westward flowing South Equatorial Current that spans the equator.³ The amplitude of
213 these tropical currents is comparable to that found in the subtropical and subpolar gyres, but the SSH
214 amplitude evident in Fig. (1) is considerably less, a straightforward consequence of geostrophy.

¹Rossby, T. C. Flagg and K. Donohue, 2010, 'On the variability of Gulf Stream transport from seasonal to decadal', *J. Mar. Res.*, 68, 503-522.

²Mesoscale eddies are ubiquitous, and impose large amplitude, but comparatively short time (periods of several months) and space (several hundred kilometers) scale variations on the gyre-scale SSH and currents, Fig. 2. For example, the SSH slope in the interior, if measured on scales of O(100 km), will be dominated by mesoscale eddy variability. Thus the instantaneous (time and space) meridional geostrophic current in the basin interior is just about as likely to be northward as southward. Similarly, any single estimate of the instantaneous Gulf Stream transport may vary by $\pm 15\%$ around the long term mean due to superimposed, apparently random mesoscale eddy variability.¹

³The connection of these zonal currents with a western boundary current is not clear from observations. There does appear to be a northward-flowing western boundary current in Fig. 2 that crosses the equator and continues northwestward along the coast of South America. This North Brazil Current is thought to be the shallow side of the the global-scale, overturning circulation that imports warm South Atlantic water into the North Atlantic basin and returns cold water at great depth. The meandering North Brazil Current frequently sheds large (several hundred kilometer diameter) eddies that transport a significant part of the warm water flow. The presence of the strong and highly variable North Brazil Current makes it difficult to discern a relationship between the western boundary current and the mainly zonal currents to the east. A concise discussion of equatorial ocean circulation including the annual variability of winds and currents is by Philander, S. G., 2001, 'Atlantic ocean equatorial currents', Academic Press, doi:10.1006/rwos.2001.0361. An excellent depiction of surface currents generally is provided by <http://oceancurrents.rsmas.miami.edu/atlantic/north-brazil.html>

215 In marked contrast to the quasi-steady subtropical and subpolar gyres noted above, some of these
 216 tropical circulation features exhibit systematic, large amplitude seasonality, e.g., the North Equatorial
 217 Counter Current is strongest in summer and disappears in winter, while the South Equatorial Current
 218 fluctuates annually by about $\pm 50\%$ (To see this important annual variability, you will need to follow the
 219 links to animations noted with Fig. 2, and see also the references in footnote 3).

220 1.2 The premise and the plan

221 The premise of this essay is that insight for the observations O1 and O2 will follow from an
 222 understanding of the classic Sverdrup relation,

$$223 \quad M_{Sv}^y = \frac{1}{\rho_o \beta} \nabla \times \tau \quad (1)$$

224 which is widely recognized as one of the bedrocks of ocean circulation theory.⁴ The righthand side of (1)
 225 is the curl of the wind stress, $\tau(x, y)$, a vector field that has to be given from observations (if taking an
 226 ocean-only perspective, as here). The left hand side is the meridional (north-south) volume transport per
 227 unit width (units are velocity times a thickness, or $\text{m sec}^{-1} \times \text{m}$). In general, meridional transport is

$$228 \quad M^y(x, y) = \int_{-d}^0 v(x, y, z) dz. \quad (2)$$

229 Two important aspects of the Sverdrup relation are that it involves the meridional component of the
 230 velocity and transport only, and, it gives no clue to the appropriate depth, d of the transport integral. It is
 231 expected that in common circumstances, e.g. Fig. 1, the Sverdrup transport will be found within the main
 232 thermocline and above, termed the upper ocean, and hence d is $O(1000 \text{ m})$. However, Sverdrup transport
 233 can just as well occur over the full depth of the ocean, as we will see in examples to follow.

⁴Sverdrup's pioneering paper that introduced the equivalent of Eqn. (1) is unfortunately not easily read or appreciated, but nevertheless: Sverdrup, H. U., 1947, 'Wind-driven currents in a baroclinic ocean, with application to the eastern Pacific', *Proc. Natl. Acad. Sci. U. S. A.*, **33**, 318-326, which is available online at <http://www.pnas.org/content/33/11/318> The first model of a western-intensified wind-driven gyre was by Stommel, H., 1948, and the time-dependent, gyre spin-up problem was discussed by Stommel, H., 1957, 'A survey of ocean current theory', *Deep Sea Res.*, **4**, 149-184. Be sure to see also Stommel's masterpiece, 'The Gulf Stream', 1966, Univ. of California Press. Time-dependence was treated in greater detail by Anderson, D. L. T. and Gill A. E., 1975, 'Spin-up of a stratified ocean with applications to upwelling', *Deep-Sea Research* **22**. These classic research papers are highly readable and may be found at <http://www.aos.princeton.edu/WWWPUBLIC/gkv/history/oceanic.html> The GFD texts noted in Part 1 each have very good discussion of the Sverdrup interior. Ch. 1 of Pedlosky, J., 1998, 'Ocean Circulation Theory', and Ch. 10 of Marshall, J. and R. A. Plumb, 2008, 'Atmosphere, Ocean and Climate Dynamics', and Ch. 14 of Vallis, G., 2006, 'Atmospheric and Oceanic Fluid Dynamics', are all highly recommended.

234 The Sverdrup relation is extraordinarily concise and in that respect, simple, but it is also very
235 abstract, and evidently incomplete. The Sverdrup relation makes no reference to time; either it holds
236 instantaneously (no), or it applies to steady flows and wind stress (steady conditions seldom if ever occur
237 in the oceans or atmosphere), or, it applies to a time-average of the wind stress and circulation. Wind
238 stress varies significantly on time scales of hours to seasons, and in some important cases, year-to-year.
239 The wind stress appropriate to (1) should then be a time-average over an interval that is consistent with
240 the ocean's response to a fluctuating stress curl. In a similar way, the Sverdrup relation is local in space;
241 the Sverdrup transport at a given point depends only upon the stress curl and the β at that point,
242 regardless of the surroundings, e.g., even a nearby landmass. This can not be true of real ocean currents,
243 which are, of course, blocked by land masses.

244 The conclusion from this first look at the Sverdrup relation is that there must be important
245 qualifications on the time and the space scales over which Eqn. (1) may be valid. In other words, the
246 Sverdrup relation, important though it is, is far from being a complete, coherent story of an ocean
247 circulation. The (refined) premise of this essay is that when we understand the origin and the limitations
248 of the Sverdrup relation, we will have gone a considerable distance toward insight for O1 and O2. The
249 objectives of this essay are then to:

250 i) Learn how the Sverdrup relation arises when the circulation of a model ocean is started
251 from rest, and so gain a sense of the time scales and mechanisms implicit in the
252 time-independent Sverdrup relation (relevant to O2).

253 ii) Show that the Sverdrup relation holds over most of the interior of a model ocean basin and
254 thus the sign of the wind stress curl determines the sense (clockwise or anti-clockwise) of
255 wind-driven gyres (relevant to O1).

256 iii) Observe that the Sverdrup relation fails near solid boundaries and is supplanted by
257 western or zonal boundary current dynamics (relevant to O1).

258 These are among the foundational problems of physical oceanography and have been addressed
259 many times over, and from a variety of perspectives. Recently and most notably, modern observational
260 methods applied to both the atmosphere and the ocean have made possible detailed analyses of the
261 Sverdrup relation over the global ocean.⁵ In a nutshell, these studies concur that the Sverdrup relation is
262 reasonably accurate (is valid) over most of the interior of the North Atlantic and North Pacific subtropical

⁵Three excellent, observation-based studies of the Sverdrup relation are by Gray, A. R. and Riser, S. C., 2014, 'A global analysis of Sverdrup balance using absolute geostrophic velocities from Argo', *J. Phys. Oceanogr.*, 1213-1229, doi: 10.1175/JPO-D-12-0206.1, and by Wunsch, C., 2011, 'The decadal mean ocean circulation and Sverdrup balance', *J. Mar. Res.*, **69**, 417-434. online at dspace.mit.edu/openaccess-disseminate/1721.1/74048 and by Thomas, M. D. et al., 2014, 'Spatial and temporal scales of Sverdrup balance', *J. Phys. Oceanogr.*, **44**, 2644-2660. doi: 10.1175/JPO-D-13-0192.1

263 gyres, provided that winds and currents are averaged over multi year periods and over horizontal scales of
264 $O(500 \text{ km})$ or greater. The Sverdrup relation is not valid near western boundary currents (wbc), which is
265 no surprise, nor is it valid in the eastward extension of the subtropical wbc (Gulf Stream) into the North
266 Atlantic Current. The subpolar gyres of the North Pacific and North Atlantic have a sense of circulation
267 (counterclockwise) that is qualitatively consistent with the Sverdrup relation, but there is only a rather
268 poor correlation in the magnitude of the observed and Sverdrup-inferred transport. The difference is
269 especially marked in the northerly half, roughly, of the subpolar gyres, where the observed meridional
270 transport is considerably less than the expected Sverdrup transport.

271 The plan here is to address objectives i) - iii) by the analysis of solutions from two shallow water
272 (layered) models. The first model is familiar from Parts 2 and 3 — one active layer and pressure anomaly
273 computed from the baroclinic density field assuming a quiescent abyssal ocean. This is dubbed the 1l-rg
274 model, and can be thought of as a 'baroclinic only' model. This 1l-rg model configuration is
275 comparatively simple and economical and is appropriate to the main goals of this essay. A second model
276 has three active layers and a free (moving) sea surface and dubbed 3l-fs. This model includes the
277 baroclinic dynamics of the first model, as well as a very fast barotropic response that makes this model
278 very expensive computationally. For both models the shallow water model equations are extended to
279 include wind forcing and dissipation. These new features are described in Section 2, which may be
280 skipped by readers not interested in the fine details (who should nevertheless take a look at the wind stress
281 fields in Figs. 4 and 5). The experiments are started from a state of rest and continue until the circulation
282 reaches a basin-wide steady state, requiring about 30 years of model ocean time (a few hours (1l-rg) or a
283 few days (3l-fs) of computer time). The transient baroclinic circulation is described in Section 3 in terms
284 of four overlapping stages, and e.g., Stage 3 begins with the onset of baroclinic Sverdrup flow. The steady
285 circulation varies a great deal over the basin. Over the majority of the basin, the steady potential vorticity
286 balance is that of the Sverdrup relation. However, near the western boundary, the balance includes a
287 significant torque due to drag on an energetic western boundary current, discussed in Section 4. Section 5
288 considers several experiments with other wind fields including one with an annual cycle, especially
289 relevant to the annual variation of tropical ocean circulation noted in O2 above. Section 6 describes the
290 solutions from the free surface model, 3l-fs. You could say that this second model solution changes
291 everything, or, you could equally well argue that it changes nothing. Closing remarks are in Section 7,
292 and links to the shallow water model and a few homework problems are in Section 8. Sections that are
293 mainly a review of earlier material, or that may be skipped over with little loss of continuity toward the
294 main goal of this essay are noted by a trailing asterisk on the title, starting with the next subsection.

295 1.3 A brief review of the Coriolis force, and the beta effect*

296 The Part 1 essay of this series examined the classical dynamics of moving parcels observed from a
297 steadily rotating coordinate frame.⁶ An immediate consequence of Earth's rotation is the Coriolis force,

$$298 \text{Coriolis force} = -2\boldsymbol{\Omega} \times \mathbf{V},$$

299 where $\boldsymbol{\Omega}$ is Earth's rotation vector which has a magnitude $7.292 \times 10^{-5} \text{ sec}^{-1}$ and \mathbf{V} is the parcel velocity
300 having (east, north, up) components (u, v, w) . The Coriolis force is, like gravity, an inertial force, that is
301 exactly proportional to the mass of an object (and hence it might be more appropriate to call it the
302 Coriolis acceleration). The Coriolis force deflects all moving objects, without doing work. For most
303 everyday objects and motions, the Coriolis force is small to the point of being negligible. It is, however,
304 of first importance for the horizontal motions of the atmosphere and oceans, i.e., winds and currents, in
305 large part because all of the other possible horizontal forces are also small. The horizontal component of
306 the Coriolis force acting on a horizontal velocity V is

$$307 -f e_z \times V = f v e_x - f u e_y \quad (3)$$

308 where e_x, e_y and e_z are the usual east, north and up unit vectors, and

$$309 f = 2\Omega \sin(lat) \quad (4)$$

310 is the all-important Coriolis parameter evaluated at a latitude lat . (Homework problem 1, Sec. 7.2.)

311 Part 2 went on to consider geostrophic balance, the defining property of large scale, low frequency
312 (extra-equatorial) geophysical flows of the atmosphere and ocean. In a geostrophic balance, the
313 horizontal component of the Coriolis force is balanced by a pressure (or geophysical height) gradient,

$$314 f v_{geo} = g' \frac{\partial h}{\partial x} \quad \text{and} \quad f u_{geo} = -g' \frac{\partial h}{\partial y} \quad (5)$$

315 where $g' \partial h / \partial x$ is the hydrostatic pressure gradient in the special case of a reduced gravity, single layer,
316 shallow water model (as in Parts 2 and 3). Geostrophic balance may be understood using an f -plane
317 approximation in which the latitudinal dependence of the Coriolis parameter (4) is, purely for
318 convenience, represented by a constant evaluated at the central latitude of a model domain, lat_o ,

$$319 f\text{-plane approximation: } f_o = 2\Omega \sin(lat_o) = \text{const.}, \quad (6)$$

320 and the coordinates are rectangular. For this to be appropriate to a given flow, the horizontal scale of the
321 motion should be limited to $O(100 \text{ km})$. The dynamics of an f -plane model are isotropic, having no

⁶These essays, including the most recent version of this essay, are available online from <https://www2.whoi.edu/staff/jprice/>

322 favored direction (recall the isotropic dispersion relation of inertia-gravity waves and geostrophic motion
323 of Part 2, Sec. 2.3).

324 In contrast to the isotropy of the f -plane, observations of the atmosphere and ocean show that
325 large-scale, low frequency, nearly geostrophic phenomena are often markedly anisotropic in one or more
326 properties. Part 3 studied the striking example offered by mid-latitude, mesoscale eddies, which are
327 observed to propagate westward, slowly but relentlessly, at a speed that depends upon latitude: at 30° N,
328 the propagation speed is about -3 km per day. In an f -plane model, an isolated, geostrophically balanced
329 mesoscale eddy may be exactly stationary in the sense of being unmoving in space and unchanging in
330 time. However, when the northward increase of f is acknowledged, the same eddy will propagate
331 westward much like observed mesoscale eddies. In Part 3 and here, the northward increase of f is
332 represented by the β -plane approximation, a linear expansion of (1) around a central latitude,

$$333 \quad \beta - \text{plane approximation: } f_1 = f_o + \beta(y - y_o), \quad (7)$$

334 with y the north coordinate and

$$335 \quad \beta = (2\Omega/R_e) \cos(lat_o)$$

336 and a constant. For this study, $lat_o = 30^\circ$ N and hence $f_o = 7.29 \times 10^{-5} \text{ sec}^{-1}$, and
337 $\beta = 1.98 \times 10^{-11} \text{ sec}^{-1} \text{ m}^{-1}$. A β -plane model is sufficient to reveal some of the most important
338 consequences of the northward variation of f , but once again the spatial scale of the phenomena should
339 be somewhat limited, say $O(1000 \text{ km})$, or less than fully global.

340 The mechanism of westward propagation may be understood as a consequence of geostrophic
341 momentum balance, (5), in combination with continuity (volume balance),

$$342 \quad \frac{\partial h}{\partial t} = -\left(\frac{\partial hu}{\partial x} + \frac{\partial hv}{\partial y}\right) \quad (8)$$

343 and, most notably, presuming $f(y)$ via Eqn. (13). Assuming that the motion has small enough amplitude
344 that variations of h are small compared to the nominal h , and that the velocity is geostrophic, then Eqns.
345 (5) and (8) may be combined in a way that reveals the very important beta effect,

$$346 \quad \boxed{\frac{\partial h}{\partial t} = \frac{\beta h}{f} v_{geo}} \quad (9)$$

347 that meridional geostrophic motion is divergent on account of the equatorward increase of geostrophic
348 motion (Fig. 3). In other words, if there is meridional motion on a beta plane, then something is going to
349 happen, either the stratification is going to change with time, or, if the flow is steady, then something

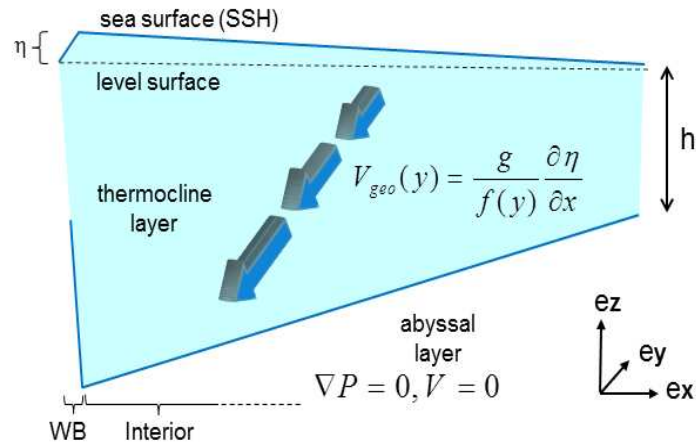


Figure 3: A schematic cross section of the North Atlantic subtropical thermocline, sliced east-west and viewed looking toward the north as in Fig. (1). The thermocline is here modeled as a single active layer. The tilt of the thermocline largely compensates the tilted sea surface so that the pressure gradient and velocity vanishing are vanishingly small in the very thick abyssal layer. This appears to be the case with the actual subtropical North Atlantic (Fig. 1), but isn't guaranteed in all circumstances. The comparatively narrow western boundary region is noted at lower left, and the much wider interior region is all of the rest. The meridional geostrophic current in the interior is equatorward; the three bold arrows are meant to depict the geostrophic current amplitude at three latitudes and assuming constant zonal gradient of the SSH. The meridional geostrophic current increases toward the equator, simply because because f decreases toward the equator. A meridional geostrophic current is thus divergent, which is here said to be 'the' beta effect. In this case having equatorward flow, the resulting layer thickness tendency is thinning, $\partial h / \partial t < 0$.

350 more has to be involved than just geostrophy.⁷ Consider the former case: Eqn. (9) may be rewritten as the
 351 first order wave/advection equation (Sec. 8.2, Problem 3),

352
$$\frac{\partial h}{\partial t} = \beta R_d^2 \frac{\partial h}{\partial x}, \tag{10}$$

353 where

354
$$R_d = \frac{\sqrt{g'h}}{f} = \frac{C}{f}$$

355 is the radius of deformation. C is the gravity wave speed; in the subtropics, $C \approx 3 \text{ m sec}^{-1}$, and at 30° N ,
 356 $R_d \approx 40 \text{ km}$.

⁷There does not appear to be a wide consensus on the meaning of the phrase 'beta effect'. Many authors, including the Glossary of the American Meteorological Society, use the term to signify anything that happens on a beta plane that would not have happened on an otherwise similar f -plane. That sort of beta effect may thus be a different thing in every different setting.

Eqn. (13) is appropriate for free motions, e.g., elementary waves $h(x, t) \propto \sin(kx - \omega t)$, and so may be characterized by a dispersion relation that connects the wavenumber, $k = 2\pi/\lambda$, and the frequency, ω ,

$$\omega = -k\beta R_d^2. \quad (11)$$

This is the long wave limit of baroclinic Rossby waves (Part 3, Sec. 2.3). In this limit, phase and group speeds are equal, at the long Rossby wave speed,

$$C_{longRo} = \frac{\omega}{k} = \frac{\partial \omega}{\partial k} = -\beta R_d^2 \leq 0. \quad (12)$$

C_{longRo} is independent of k and ω , and so this propagation is nondispersive and westward ($\beta \geq 0$). Eqn. (10) is thus a first order wave/advection equation,

$$\frac{\partial h}{\partial t} = -C_{longRo} \frac{\partial h}{\partial x} \quad (13)$$

C_{longRo} varies quite a lot with f , but at a fixed cite, C_{longRo} is, insofar as h is concerned, a constant, westward advection velocity. Using values from 30° N, $C_{longRo} \approx -3 \text{ km day}^{-1}$, which is about 1% of the gravity wave speed, C , and is consistent with the observed propagation of mesoscale eddies noted above.

What is most important is that all free (unforced) large scale ($\lambda \gg R_d$), low frequency ($\omega \ll f$) phenomena that share (5), (8) and (13) will propagate westward, regardless of planform. If there are indeed no small horizontal scales involved, then the planform will be conserved and will appear to be shifted steadily westward, as if by advection, at the constant rate, C_{longRo} . It seems appropriate to call such westward propagating phenomena 'Rossby waves', even if the planform may look nothing like an elementary wave.⁸ As we will see in Sec. 3.1.3, an appreciation for this generalized Rossby wave propagation is a key concept needed to understand the response of an ocean circulation to a transient wind. (For a little more on this see Homework problem 3, Sec. 8.2.)

1.4 Aspects of depth-dependence*

The shallow water model used here (modified as described in the Appendix to include several layers) is simplified considerably compared to the real ocean or a comprehensive general circulation model in that

⁸Much of the pioneering research on the topics discussed in this essay appeared in a series of classic papers by Carl G. Rossby and colleagues published in the late 1930s. A collection of Rossby's highly readable papers is available online at <http://www.aos.princeton.edu/WWWPUBLIC/gkv/history/general.html>

381 it represents ocean currents by means of just one (the default) or at most a few active layers (the
 382 Appendix). Thus the shallow water horizontal velocity within a layer is, *per force*, depth-independent;
 383 east and north velocity components are u and v , and e.g., u is $u(x, y, t)$, but not $u(x, y, z, t)$.

384 As a prelude to a shallow water model, it is helpful to consider briefly what amounts to its
 385 complement, a three-dimensional system that is presumed to be steady, linear and inviscid and that does
 386 admit depth-dependence. The three dimensional velocity components of this system are u , v , and w , and
 387 e.g., u is $u(x, y, z)$ (note that this holds for the present section only). The three dimensional continuity and
 388 momentum equations of this system are

$$389 \quad 0 = \frac{\partial u}{\partial x} + \frac{\partial v}{\partial y} + \frac{\partial w}{\partial z}, \quad (14)$$

$$391 \quad 0 = -fv - \frac{1}{\rho_o} \frac{\partial p}{\partial x} + \frac{1}{\rho_o} \frac{\partial \tau^x}{\partial z}, \quad (15)$$

$$392 \quad 0 = fu - \frac{1}{\rho_o} \frac{\partial p}{\partial y} + \frac{1}{\rho_o} \frac{\partial \tau^y}{\partial z}. \quad (16)$$

394 The Coriolis parameter f is $f(y)$ via the β -plane approximation, Eqn. (7), and the β effect is crucially
 395 important in what follows. There are two steady forces recognized here, the horizontal gradient of the
 396 hydrostatic pressure, p ,

$$397 \quad p(x, y, z) = \int_{-z}^{\eta(x, y)} g \rho(x, y, z) dz,$$

398 which, like the velocity components, is an unknown. In principle, the density field and the SSH anomaly
 399 η that contribute to the hydrostatic pressure are within the scope of a comprehensive ocean circulation
 400 model, though we are not claiming that for this system. A second important force is the vertical gradient
 401 of a turbulent momentum flux,

$$402 \quad \tau^x(x, y, z) = \rho_o \langle u'(x, y, z, t) w'(x, y, z, t) \rangle$$

403 where the brackets $\langle \ \rangle$ indicate a time average over tens of minutes. The small scale,
 404 three-dimensional motions u' , w' that propagate a turbulent momentum flux are far outside the scope of
 405 large scale circulation model. We will, however, presume to know the surface value, $\tau_o = \tau(x, y, z = 0)$,
 406 which may be estimated from observations of wind over the oceans, i.e., τ_o is said to be the wind stress.
 407 And we also know something about the vertical scale over which the stress is divergent, discussed below.

408 Given that the balances are steady and linear, we can rewrite the force terms on the right hand side of
 409 (15) and (16) in terms of geostrophic and Ekman velocity components, say for the meridional component,

$$410 \quad v_{geo} = \frac{1}{\rho_o f} \frac{\partial p}{\partial x} \quad \text{and} \quad v_{Ek} = -\frac{1}{\rho_o f} \frac{\partial \tau^x}{\partial z}$$

411 with no loss of generality. Thus, in this steady, linear model

$$412 \quad v = v_{geo} + v_{Ek}.$$

413 Similarly, the meridional transports associated with these velocities may be written

$$414 \quad M^y = M_{geo}^y + M_{Ek}^y \quad (17)$$

415 where

$$416 \quad M_{geo}^y = \int_{-d_{geo}}^0 v_{geo} dz, \quad (18)$$

417 and

$$418 \quad M_{Ek}^y = \int_{-d_{Ek}}^0 v_{Ek} dz = -\frac{1}{\rho_o} \frac{\tau_o^x}{f}. \quad (19)$$

419 The lower limit of depth in these transport integrals is significant. The wind-driven geostrophic velocity
 420 of the major ocean gyres is appreciable to at least the depth of the lower main thermocline, d_{geo} is
 421 O(1000 m), and geostrophic currents associated with the global-scale overturning circulation extend over
 422 the full depth water column, noted in the discussion of Fig. (1). The Ekman velocity will be significant
 423 within an upper ocean surface layer that is mixed and stirred by the turbulent stress imposed at the
 424 surface by the wind, and so is quasi-homogeneous with respect to density. In density-stratified regions,
 425 such as the subtropical gyre, this Ekman layer may be as deep as the top of the seasonal thermocline, d_{Ek}
 426 is O(100 m), and hence almost always much less than d_{geo} . This important effect of stratification is
 427 something we will come back to when it is time to consider what is missing from a shallow water model
 428 (Secs. 4.3.2 and 6.3).

429 Assuming that the wind stress on the sea surface is known, then the Ekman transport Eq. (19) is also
 430 known. The geostrophic transport (18) remains completely unconstrained, however, and so we can't go
 431 any further with momentum balance and continuity alone. To find out what we can learn about this
 432 system, it is very helpful to form the vorticity balance: take the partial x derivative of (16) and subtract
 433 the y derivative of (15); then eliminate the horizontal divergence $\partial u/\partial x + \partial v/\partial y$ using the continuity
 434 equation (14). This has the effect of eliminating pressure and yields the (steady, linear) vorticity balance,

$$435 \quad \beta v = f \frac{\partial w}{\partial z} + \frac{1}{\rho_o} \frac{\partial}{\partial z} \left(\frac{\partial \tau^y}{\partial x} - \frac{\partial \tau^x}{\partial y} \right), \quad (20)$$

436 that holds at all z where (15) - (14) are valid. The depth-dependence of w and of the wind stress-induced
 437 momentum flux are not knowable within this system alone, and so it is very helpful to depth-integrate
 438 (20) from some great depth $z = -d$ where the wind stress may be presumed to vanish, up to the sea
 439 surface where the wind stress is presumed known and the vertical velocity must vanish, *to wit*, the depth
 440 integral of (20) is

$$441 \quad \beta \int_{-d}^0 v dz = \beta M_{-d}^y = -fw(-d) + \frac{1}{\rho_o} \left(\frac{\partial \tau_o^y}{\partial x} - \frac{\partial \tau_o^x}{\partial y} \right). \quad (21)$$

442 While this depth-integrated vorticity equation (21) has given up on depth-dependence, the transport that it
 443 helps uncover is of great interest. The first term on the right is the vortex stretching effect of the vertical
 444 velocity at $z = -d$, $fw(-d)$. With this term included, (21) is as general as Eqns. (15) - (14), and M_{-d}^y of
 445 (21) is the meridional transport regardless of what the ultimate cause may be, i.e., whether wind-driven in
 446 the Ekman or Sverdrup sense or geostrophic flow associated with the global-scale, overturning
 447 circulation.

448 The depth-integrated vorticity equation (21) is still not closed as there are two unknowns, the
 449 transport above $z = -d$, M_{-d}^y , and the vortex stretching term, $fw(-d)$. To make a closed estimate of the
 450 transport we have to evaluate the latter. The simplest assumption is that $w(-d)$ vanishes under one of
 451 three possible scenarios: If the sea floor was both flat and frictionless, then w at the sea floor would
 452 vanish. However, the sea floor is only rarely flat, and in any event, not truly frictionless so that a bottom
 453 Ekman layer may provide a form of Ekman pumping or suction near the bottom (Ekman pumping is
 454 discussed in Sec. 3.1.2). Another argument for dropping the $w(-d)$ term is that the wind-driven
 455 circulation of a density-stratified ocean should be somewhat surface intensified, and may be negligible at
 456 some depth below the thermocline, typically 1000 - 2000 m, implying that $w(-d) = 0$ at that depth as
 457 well. The almost flat isopycnal surfaces at approx. 1500 m in Fig. (1) suggest that this could be
 458 appropriate for much of the subtropical gyre in the North Atlantic. An important exception, already
 459 noted, is that the western basin shows evidence of significant deep flows associated with the global-scale,
 460 meridional overturning circulation and so clearly, $d = 1500$ m is not valid generally. Finally, the best
 461 rationale for dealing with the deep vortex stretching term is that since the balances have already been
 462 presumed to be linear, the meridional transport may be imagined to be a superposition from more than
 463 one source, i.e., wind-driven, Sverdrup transport plus overturning transport which is not related to the
 464 local wind. To get at the former, we can assert that $w(-d) = 0$ for a plausibly deep d , and then Eqn. (21)
 465 reduces to the Sverdrup relation, Eqn. (1),

$$466 \quad \boxed{\beta M_{-d}^y = \frac{1}{\rho_o} \nabla \times \tau_o} \quad (22)$$

467 We could just as well write the transport on the left side as M_{Sv}^y since that is what we have defined the
 468 Sverdrup transport to be. Setting aside questions of the appropriate d , this last result shows that Sverdrup
 469 transport is the total meridional transport, regardless of the momentum balance. In the present system, the
 470 transport is just geostrophic plus Ekman, Eqn. (17) and so

$$471 \quad \boxed{\beta M_{Sv}^y = \beta (M_{geo}^y + M_{Ek}^y) = \frac{1}{\rho_o} \nabla \times \tau_o} \quad (23)$$

472 (The superscript y on M_{Sv}^y is redundant since Sverdrup transport is solely meridional.) Said a little

473 differently, the Sverdrup relation can be seen as a mode, i.e., a two term balance, of the steady, linear
 474 *vorticity* balance (21) in which deep vortex stretching is argued to be negligible. Geostrophic and Ekman
 475 balances are modes of the *momentum* balance and hence they come from a different class than does the
 476 Sverdrup relation. Geostrophic and Ekman flows are important in virtually all large scale ocean
 477 circulation problems. However, other forces and processes are possible too, e.g., horizontal eddy fluxes
 478 of potential vorticity may also contribute to the mean vorticity balance and to meridional transport.⁹

479 The meridional Ekman transport (19) may be subtracted from (23) to yield the geostrophic
 480 component of the Sverdrup transport,

$$481 \quad M_{Svgeo}^y = \frac{f}{\rho_o \beta} \nabla \times \left(\frac{\tau_o}{f} \right) \quad (24)$$

482 Notice that the geostrophic transport, which is generally appreciable at depths well below the Ekman
 483 layer that is driven directly by a turbulent wind stress, can nevertheless be written in terms of the curl of
 484 the wind stress at the sea surface if the assumptions behind the Sverdrup relation are valid. This implies a
 485 connection between the Ekman layer and the deeper ocean via vortex stretching that will be discussed in
 486 Section 4.3.

487 2 Shallow water models of wind-driven circulation

488 The shallow water model introduced in Part 2 can be made into a useful tool for studying some important
 489 facets of the wind-driven circulation by 1) defining an appropriate domain and boundary conditions, 2)
 490 adding a new term that represents wind forcing, and 3) including a very simple form of dissipation.

491 2.1 Boundary and initial conditions

492 The ocean domain is taken to be a square basin with sides of length $2L$ centered on 30°N . Rotation is
 493 treated by a β -plane approximation and the basin size is then chosen so that the southern boundary will
 494 correspond to the equator, $f = 0$. Given $\beta(30^\circ)$, this requires $L = 3600$ km. The resulting basin width,

⁹Holland, W. R. and P. B. Rhines, 1980, 'An example of eddy-induced ocean circulation', *J. Phys. Oceanogr.*, **10**, 1010-1031.

495 $2L = 7200$ km, is roughly comparable to the average width of the North Atlantic Ocean, but is only about
 496 half the width of the mighty Pacific Ocean. The intention is to model a self-contained circulation, and so
 497 the boundaries of the model domain are made impermeable by setting the normal component of velocity
 498 to zero,

$$499 \quad \mathbf{V} \cdot \mathbf{n} = 0, \quad (25)$$

500 on all of the boundaries.¹⁰

501 The initial condition is a state of rest throughout the basin and isopycnals are everywhere flat,

$$502 \quad \mathbf{V}(x, y) = 0 \text{ at } t = 0, \text{ and } h(x, y) = \text{constant} \text{ at } t = 0 \text{ and for all } (x, y). \quad (26)$$

503 The specification of the initial thickness is deferred to Sec. 2.5.

504 2.2 Wind stress and its curl

505 The energy source in these experiments is a wind stress, $\tau(x, y)$, a tangential force per unit area imposed
 506 on the sea surface (the subscript o needed in Sec. 1.3 has been dropped since only the surface value of
 507 wind stress will be relevant from here on). The wind stress field has to be specified from outside the
 508 model, and here it will be represented by an idealization of the time-mean wind stress that has been
 509 computed from observed winds over the oceans, Fig. (4).¹¹ So far as the Sverdrup relation is concerned,
 510 the crucial property of the wind stress field is the curl, $\nabla \times \tau(x, y)$. The shallow water model requires the
 511 wind stress itself, and here, just to keep it simple, we will specify the zonal component τ^x only, and
 512 assume that τ^x is independent of x , thus

$$513 \quad \tau^x(y) = \xi \sin(n\pi y/L), \quad (27)$$

¹⁰The southern and northern boundaries of the real North Atlantic basin are not barriers as the present model domain implies. There is instead a significant poleward flow of warm water from the southern hemisphere into and through the North Atlantic. In the equatorial region this occurs largely within a western boundary current evident in Fig. 2, usually called the North Brazil Current. At the northern boundary, some of this warm inflow continues poleward into the Norwegian-Greenland Sea as the North Atlantic Current (or Drift). The shallow, warm poleward flow is balanced by a deep, cold equatorward flow (deeper than the thermocline layer shown in Fig. 1). The cross-equatorial exchange of warm and cold water is a very important component of the global-scale, meridional overturning circulation. The overturning circulation is not driven directly by basin-scale winds, as are the upper ocean gyres of Fig. 2, and so an overturning circulation does not arise in the present experiment.

¹¹A particularly handy reference for such climate data is by Peixoto and Oort, 1992, *Physics of Climate*, American Inst. of Physics, New York, NY. There are now more than a dozen wind stress climatologies that are consistent at the semi-quantitative level needed here (see Townsend, T. L., H. E. Hurlburt and P. J. Hogan, 2000, 'Modeled Sverdrup flow in the North Atlantic from 11 different wind stress climatologies', *Dyn. Atmos. Oceans*, **32**, 373-417.) The differences in detail between the various wind stress climatologies make an easily detectable and in some ways important difference in the computed Sverdrup flow, as does the basin topography.

514 where the amplitude ξ is a positive constant. For the standard case of Sec. 3, $n = 1$, and the wind stress
 515 is eastward over the northern half of the basin, which mimics westerly winds, and westward on the
 516 southern half of the basin, i.e., easterlies (Fig. (5)). The amplitude is taken to be $\xi = 0.1$ Pa, or about what
 517 is estimated for the mean wind stress by the westerlies. In the experiment of Sec. 3, this wind stress field
 518 is assumed to be constant in time once it is switched on. (In Sec. 5.1, the amplitude, ξ , will be made to
 519 oscillate with an annual cycle, and in Sec. 5.3 the wind stress will be made meridional.)

520 A very important parameter of (27) is

521 the meridional length scale of the wind field; for $n = 1$, $L_\tau = L/n\pi \approx 1200$ km.

522 This is comparable to though a little less than two other important horizontal scales in this problem,

523 the basin scale, $L = 3600$ km, and,

524 the planetary scale on which f varies, $R_f = R_E/2 \approx 3300$ km,

525 where R_E is the radius of the Earth. All of these length scales are much greater than the natural horizontal
 526 length scale of the baroclinic ocean,

527 the baroclinic radius of deformation at 30° latitude, $R_d \approx 40$ km.

529 The wind stress is applied to the surface layer of the model ocean as if it was a body force absorbed
 530 evenly throughout the surface layer and hence the acceleration due to wind stress alone is just

$$531 \quad \frac{D\mathbf{v}_1}{Dt} = \frac{\boldsymbol{\tau}}{\rho_o h_1}, \quad (28)$$

532 which is a valid approximation of the full momentum balance for very short times, $t \ll 1/f$, a few hours
 533 or less. In a shallow water model, $d_{Ek} = h_1$, and here we have chosen $h = 250$ m (three layer model), or
 534 500 m (single layer reduced gravity model), in order to have a realistic baroclinic wave speed. In the real,
 535 stratified ocean, d_{Ek} is much less, typically 25 - 100 m. We will consider some of the implications of this
 536 as we go along, but for now note that the Ekman current in this model is considerably weaker than in the
 537 real ocean, but the Ekman transport and the Sverdrup transport are the same whether the wind stress is
 538 absorbed in a comparatively thin surface layer (as actually occurs) or over the entire upper ocean layer
 539 that is wind-driven in the Sverdrup sense, as happens in a shallow water model.

540 The curl of the wind stress given by (27) is

$$541 \quad \nabla \times \boldsymbol{\tau}(x, y) = -\frac{\partial \tau^x}{\partial y} = -\frac{n\pi\xi}{L} \cos(\pi y/L), \quad (29)$$

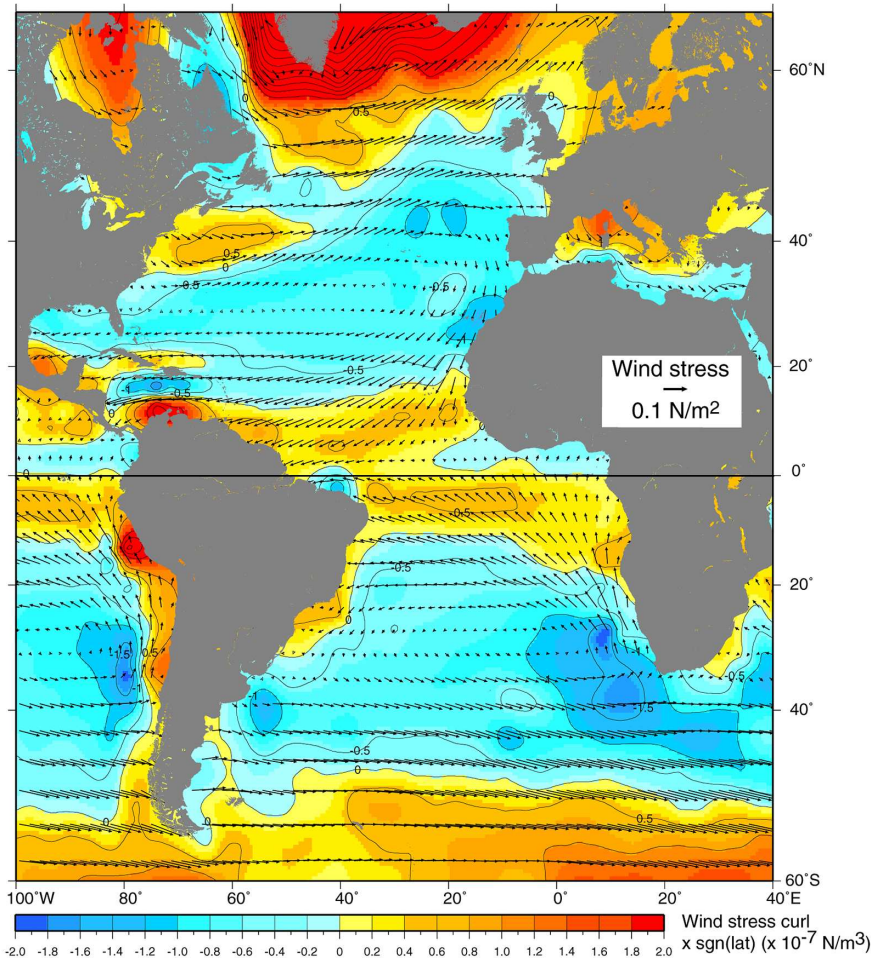


Figure 4: The vector field is the climatological mean wind stress (scale at center right), the color contours are proportional to the wind stress curl (scale at the bottom). These data were computed from a reanalysis of observed wind compiled by the National Center for Environmental Prediction. Over both the North Atlantic and South Atlantic basins the broad pattern includes westerly winds from roughly 35° to 50° , and easterly winds in tropical regions, latitude less than 20° , and also in subpolar regions, latitude greater than roughly 55° . The stress curl is thus negative over the subtropics and positive over the equatorial and subpolar regions. This beautiful and informative figure is thanks to L. D. Talley et al., *Descriptive Physical Oceanography*, Elsevier, Fig. S09.3, <http://booksite.elsevier.com/DPO/chapterS09.html>

542 which has an amplitude $\xi/L_\tau \simeq 0.8 \times 10^{-7} \text{ N m}^{-3}$ ($n = 1$). This is comparable to typical values of
 543 stress curl seen in Fig. (4), but less than the maximum values, which are roughly $2 \times 10^{-7} \text{ N m}^{-3}$. The
 544 sign of the wind stress curl defines three regions: a central subtropical region where the stress curl is
 545 negative (clockwise turning), and tropical and subpolar regions where the curl is positive
 546 (anti-clockwise), Fig. (5).

547 This idealized stress field is least realistic for the tropical region insofar as it omits a secondary
 548 maximum of the easterly winds often present near the equator (most pronounced in the Pacific). This
 549 gives a narrow region of negative stress curl within a few degrees of the equator that, if included here,
 550 would give two smaller tropical gyres vs. one rather large tropical gyre that results from (27). This error
 551 in the tropical winds is left in place because the goal is not so much a realistic simulation of the observed
 552 ocean circulation — which would require much more than just a better wind field — but rather to
 553 investigate how the wind-driven circulation varies with latitude. The idealized stress field Eqn. (27) is

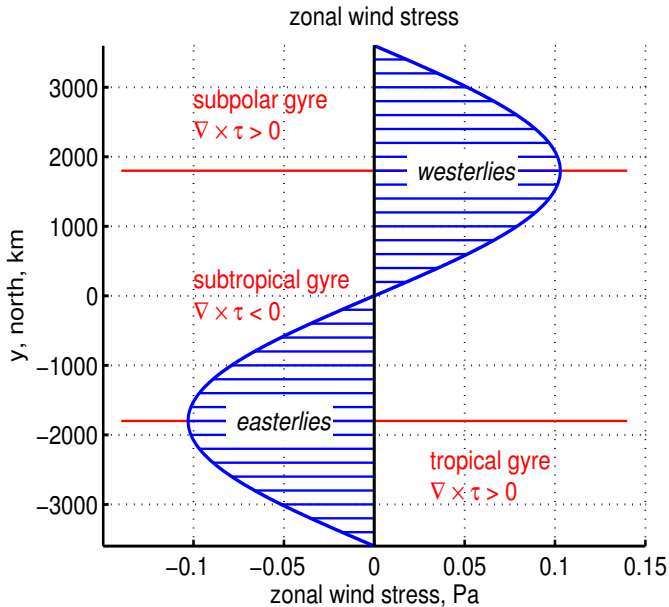


Figure 5: An idealized, zonal wind stress field that is applied to the shallow water model. The horizontal red lines appear in subsequent figures to show the axes of the easterly and westerly wind maxima, and thus the boundaries of the stress curl — negative (clockwise) in the large subtropical region between the westerly and easterly axes, and positive (anti-clockwise) over the smaller tropical and subpolar regions. These red lines correspond closely to the gyre boundaries.

554 appropriate to this goal since the wind stress curl magnitude of (27) is the same over the three regions
 555 (tropical, subtropical and subpolar). β is also the same, and hence so too is the Sverdrup transport. The
 556 *actual* transport is, *not* the same, however, because of zonal boundary effects that extend many hundreds
 557 of kilometers into the tropical and subpolar gyres and reduce the transport to values below that expected
 558 from the Sverdrup relation (Sec. 4.2.3).

559 2.3 An expedient parameterization of drag on ocean currents*

560 With a wind stress included, and if we intend to compute up to a possible steady state, then there has to
 561 be some mechanism to dissipate the energy and potential vorticity that are supplied by the wind. The
 562 present model follows the classic treatment by Stommel (1948)⁴ in choosing a linear drag that is
 563 proportional to and anti-parallel to the velocity,

$$564 \quad \text{drag} = -r h_o \mathbf{V}, \quad (30)$$

565 sometimes called Stokes drag. This has the dimensions of a stress/density, and the resulting acceleration
 566 is $-r h_o \mathbf{V}/h$ (as in the single particle model of Part 1, Section 5, aside from varying layer thickness). The
 567 coefficient r is taken to be $r = 1/(15 \text{ days})$, the smallest value of r that will allow the ocean circulation in
 568 this system (wind stress included) to reach a near steady state. Given a nominal layer thickness, $h \approx h_o$,
 569 the Ekman number at 30°N is $E = r/f \approx 0.01$. This E may seem quite small, but nevertheless, the

570 model dynamics are almost certainly more viscous overall than is the real ocean. In Secs. 3 and 4 we will
 571 find out how this value of r is related to the natural width of the western boundary current, the radius of
 572 deformation.

573 In some contexts it might be argued that the Stokes drag represented by Eqn. (30) is a crude
 574 treatment of bottom drag. However, that is not plausible here since the active layer is not imagined to be
 575 in contact with a sea floor. It is probably better to think of the Stokes drag as nothing more than the
 576 simplest form of a drag or dissipation process that permits a steady state in this model. Given this *ad hoc*
 577 basis for (30), we will have to be careful not to over interpret those aspects of the solution that depend
 578 sensitively upon the value of r , most notably the zonal boundary current width of Sec. 4.3.

579 2.4 Momentum and vorticity balances

580 With wind stress and drag included, the shallow water continuity (thickness balance) and momentum
 581 equations (derived in Part 2) are

$$582 \quad \frac{Dh}{Dt} = \frac{\partial h}{\partial t} + \mathbf{V} \cdot \nabla h = -h \nabla \cdot \mathbf{V}, \quad (31)$$

$$583 \quad \frac{D\mathbf{V}}{Dt} = \frac{\partial \mathbf{V}}{\partial t} + \mathbf{V} \cdot \nabla \mathbf{V} = -\nabla P / \rho_o - f \mathbf{k} \times \mathbf{V} + \frac{\boldsymbol{\tau}}{\rho_o h} - \frac{r h_o}{h} \mathbf{V}. \quad (32)$$

584 The P is hydrostatic pressure anomaly defined in the next subsection. Notice that the thickness balance
 585 (31) is adiabatic in the sense that the thickness can change only by way of a divergent thickness flux, and
 586 hence the net (basin integral) thickness is conserved.¹² This is not true for the momentum balance
 587 because of the wind stress source term and the Stokes drag dissipation term.
 588

589 The shallow water potential vorticity is

$$590 \quad q = \frac{\nabla \times \mathbf{V} + f}{h}, \quad (33)$$

591 and the q -balance is

$$592 \quad \frac{Dq}{Dt} = \frac{\partial q}{\partial t} + \mathbf{V} \cdot \nabla q = \frac{1}{\rho_o h} \nabla \times \frac{\boldsymbol{\tau}}{h} - \frac{r h_o}{h} \nabla \times \frac{\mathbf{V}}{h}. \quad (34)$$

¹²This adiabatic property is especially convenient for some diagnostics of the time-changing stratification. However, it is also a liability, insofar as the layer thickness given by (31) can vanish under some plausible forcing regimes, especially at high latitudes. Vanishing layer thickness means instant death for a numerical integration. A partial remedy is to start with a fairly thick initial layer, 500 m, as is done here. Better would be the inclusion of a vertical mixing process that kept the upper layer thickness finite at all times, but which is not attempted here.

593 Part 3 studied free Rossby waves that could be described via the mechanisms of q conservation,
 594 $Dq/Dt = 0$. Rossby wave-like motions are possible also in (34) and are a crucial part of the
 595 time-dependent dynamics discussed in Sec. 3.3.

596 2.5 Models of stratification and pressure

597 The last piece is to connect the hydrostatic pressure P with the mass field, i.e., the stratification. Two
 598 models are used here.

599 2.5.1 Single layer, reduced gravity model, 1l-rg

The stratification model used most extensively here is exactly the shallow water, single layer, reduced gravity model of Parts 2 and 3, *viz.*, a single active upper ocean layer above a quiescent (infinitely deep) abyssal layer. In that event, the hydrostatic pressure anomaly within the upper ocean layer is just

$$P = g\delta\rho(h - h_o)$$

which gives a high pressure (anomaly) where the layer thickness is large. The equivalent SSH is just

$$\eta_1 = \frac{\delta\rho}{\rho_0}(h - h_o).$$

600 The initial thickness is chosen to be fairly large, $h_o = 500$ m, and the density difference fairly small,
 601 $\delta\rho = 2 \text{ kg m}^{-3}$. The nominal gravity wave speed is thus $= \sqrt{g\delta\rho h_o/\rho} = 3 \text{ m sec}^{-1}$, which is a realistic
 602 baroclinic gravity wave speed for the subtropics, but a little high for the tropics and subpolar regions of
 603 the ocean. The radius of deformation at 30° is $R_d = 42$ km, and the equatorial radius of deformation is
 604 $R_{deq} = \sqrt{C/\beta} = 400$ km.

605 2.5.2 Three layer, free surface model, 3l-fs

606 In this somewhat more realistic model, the stratification is represented by two upper ocean layers, and a
 607 comparatively thick abyssal layer (Fig. 6). This is still quite truncated, but sufficient to make a few

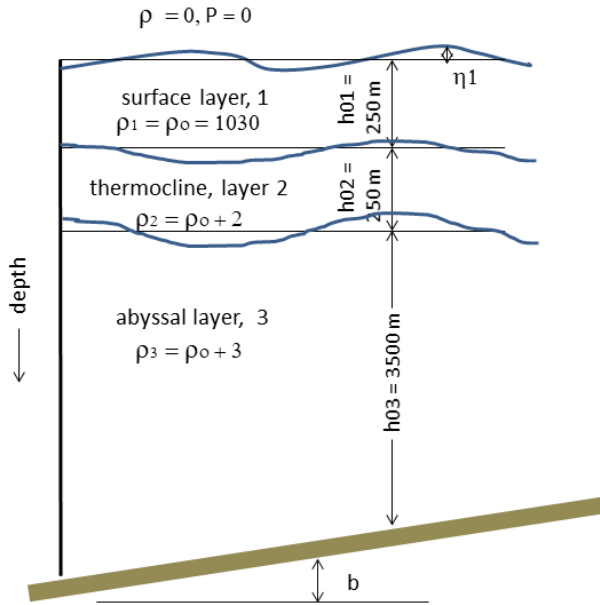


Figure 6: A three layer representation of the density stratification of the open ocean. The density and the thickness of each layer is noted. These thickness and density values are most apropos the subtropical ocean, but are presumed to hold throughout the basin. In this study the bottom depth b is presumed constant, i.e., a flat bottom.

608 important points (Sec. 6). The surface layer, h_1 , is presumed to absorb all of the wind stress. Layer 2 is
 609 the thermocline, which follows the same momentum balance as does layer 1, though with zero wind
 610 stress, and layer 3 is the thick abyssal layer, same comment. In general, the thickness of the abyssal layer
 611 should include a significant term due to the spatially variable sea floor depth, which for now is taken to be
 612 uniform, $b = 0$. This three layer model is a straightforward generalization of the shallow water (layered)
 613 model of Parts 2 and 3, sometimes referred to as a stacked shallow water model. The initial thickness and
 614 the constant density difference, $\delta\rho$, across the top of these layers is taken to be

	h_{0i}, m	$\rho_i, kg\ m^{-3}$	$\delta\rho_i, kg\ m^{-3}$
615	250	1030	1030
	250	1032	2
	3500	1033	1

616 The density and pressure of the overlying atmosphere are presumed to vanish and hence the density
 617 contrast across the sea surface, the top of layer 1, is $\delta\rho_1 = \rho_o = 1030\ kg\ m^{-3}$, the nominal density of sea
 618 water. The density contrast across the top of layers 2 and 3 is very much less, $\delta\rho_2 = 2\ kg\ m^{-3}$ and
 619 $\delta\rho_3 = 1\ kg\ m^{-3}$. In that sense, the ocean is very weakly stratified internally. Nevertheless, this internal
 620 stratification is of first importance for many oceanic phenomenon. The surface layer thickness is taken to

621 be 250 m to delay the occurrence of $h \rightarrow 0$, and so is too large by a factor of about five. Hence the
622 wind-driven surface layer currents in this model are weak compared to observations.

623 Layer thickness is a conserved quantity, barring vertical mixing (which undoubtedly occurs),
624 meaning that the thickness of a given layer can change only if there is a divergence of volume flux within
625 that layer, i.e.,

$$626 \quad \frac{\partial h_1}{\partial t} = - \left(\frac{\partial(h_1 u_1)}{\partial x} + \frac{\partial(h_1 v_1)}{\partial y} \right), \quad (35a)$$

$$627 \quad \frac{\partial h_2}{\partial t} = - \left(\frac{\partial(h_2 u_2)}{\partial x} + \frac{\partial(h_2 v_2)}{\partial y} \right), \quad (35b)$$

$$628 \quad \frac{\partial h_3}{\partial t} = - \left(\frac{\partial(h_3 u_3)}{\partial x} + \frac{\partial(h_3 v_3)}{\partial y} \right). \quad (35c)$$

630

631 The horizontally-varying pressure anomaly is due to the displacement of the density surfaces away
632 from their nominal, resting, flat state. From the bottom up, the interface displacements are

$$633 \quad \eta_3 = h_3 - h_{03} - b, \quad (36a)$$

$$634 \quad \eta_2 = \eta_3 + h_2 - h_{02}, \quad (36b)$$

$$635 \quad \eta_1 = \eta_3 + \eta_2 + h_1 - h_{01}. \quad (36c)$$

637 The motions of interest have very gentle accelerations compared to g , and so the pressure anomaly that
638 accompanies the displaced density field may be assumed hydrostatic, i.e., due to the weight of the
639 overlying water column. The hydrostatic pressure anomaly within each layer is then, from the surface
640 layer down,

$$641 \quad P_1 = g \rho_0 \eta_1, \quad (37a)$$

$$642 \quad P_2 = P_1 + g \delta \rho_2 \eta_2, \quad (37b)$$

$$643 \quad P_3 = P_2 + g \delta \rho_3 \eta_3. \quad (37c)$$

645 The height of a given density interface thus depends upon the thickness of the fluid layers below, while
646 the pressure depends upon the displaced density surfaces above. This bottom-up density/thickness
647 relationship and top-down pressure/density relationship is what you would expect physically from
648 hydrostatic pressure.

649 The description of motions that develop in this system is oftentimes aided by reference to the normal
 650 modes of the system. In fact, the normal modes show up fairly distinctly in the solutions that follow. A
 651 method for computing the normal modes was discussed in Part 2, Sec. 4.2 (and implemented via the
 652 Matlab script `twolayer_eig.m` available online, Sec 7.1) and so we will go straight to the results, the
 653 eigenvectors of velocity and thickness, and the eigenvalues that are the gravity wave (non-rotating) phase
 654 speeds of the modes,

655 Barotropic mode

gravity wave phase speed $C \approx \sqrt{g(h_1 + h_2 + h_3)} = 200 \text{ m sec}^{-1}$	$\begin{pmatrix} u & h \\ 1 & 0.07 \\ 1 & 0.07 \\ 1 & 1 \end{pmatrix}$
radius of deformation at 30° N , $R_d = C/f = 2800 \text{ km}$	
long Rossby wave speed at 30° N , $\beta R_d^2 = 142 \text{ m sec}^{-1} = 1230 \text{ km day}^{-1}$.	

656 Baroclinic mode 1

phase speed $\approx \sqrt{g(\delta\rho_2 + \delta\rho_3)(h_1 + h_2)/\rho_o} = 2.9 \text{ m sec}^{-1}$	$\begin{pmatrix} u & h \\ 1 & -0.7 \\ 0.41 & -0.3 \\ -0.1 & 1 \end{pmatrix}$
radius of deformation, 42 km	
long Rossby wave speed, $0.033 \text{ m sec}^{-1} = 2.9 \text{ km day}^{-1}$.	

657 Baroclinic mode 2

phase speed $\approx \sqrt{g \delta\rho_3 h_1/\rho_o} = 1.5 \text{ m sec}^{-1}$	$\begin{pmatrix} u & h \\ 1 & 1 \\ -1 & -1 \\ 0 & 0 \end{pmatrix}$
radius of deformation, 22 km	
long Rossby wave speed, $0.009 \text{ m sec}^{-1} = 0.8 \text{ km day}^{-1}$.	

658 The eigenvectors of velocity are normalized so that the surface layer has an amplitude of 1; the thickness
 659 eigenvectors are normalized so that the largest amplitude in any layer is 1, Fig. (7).

660 Compared with the reduced gravity model, the crucial new property of this system is that it supports
 661 a barotropic wave having a very, very fast phase speed, $200 \text{ m sec}^{-1} \approx 1700 \text{ km day}^{-1}$. Thus, a
 662 barotropic wave can traverse an entire ocean basin in a few days, vs many months for a baroclinic wave.
 663 The interface displacements of the barotropic mode are in phase with depth, but are largest at the sea
 664 surface and decrease linearly to zero at the bottom (not apparent in this figure). The pressure gradient is
 665 determined almost entirely by the displacement of the sea surface, and the associated barotropic velocity
 666 is essentially uniform with depth. Such a barotropic motion would be the only thing possible a model
 667 having no internal stratification whatever. There are two baroclinic normal modes that, are, by
 668 comparison, quite sluggish, having phase speeds approx. 3 m sec^{-1} and 1.5 m sec^{-1} . The velocity in
 669 these baroclinic normal modes is depth-dependent, and has vanishing transport when integrated over the
 670 full water column.

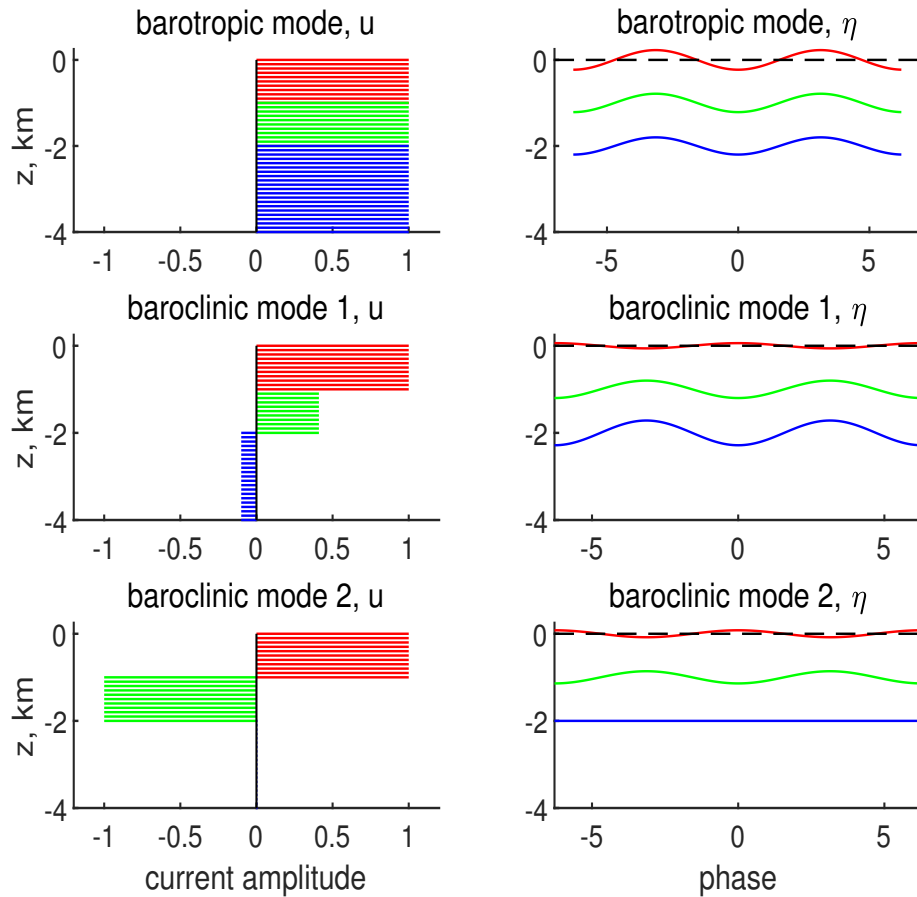


Figure 7: **(left)** Eigenvectors of the velocity from the three layer model. The layer-to-layer relative amplitudes of the velocity eigenvectors are meaningful, but their apparent thickness and thus depth is not to scale in this figure (the upper layer thicknesses have been quadrupled for the purpose of illustration). **(right)** Interface displacement computed from the eigenvectors of thickness by integrating from the bottom up, as in Eqn. (36). The amplitude of the interface displacements is schematic only but the phases are meaningful. For example, in the first baroclinic mode, the surface layer and the thermocline move up and down in phase in a 'sinuous' mode. Baroclinic mode 2 is confined almost entirely to the thermocline and surface layers, and is a 'varicose' mode in which the thickness changes in these layers are of almost equal magnitude and are out of phase.

671 These normal modes are orthogonal, and span the space, in the sense that any arbitrary free motion
672 (any wave) that can occur in the three layer model can be formed as the linear sum of these modes. Since
673 all of the eigenvectors are required to make a complete set, we can't really claim that any one of them is
674 more important than the others. However, the first baroclinic mode does have the most prominent role in
675 the basin-scale adjustment process to an imposed wind, *viz.* the changeover from a (largely) barotropic
676 state that forms very quickly after the wind starts, to a baroclinic, surface intensified state (Sec. 3.3) at
677 much longer times. This is implicit in the choice of parameters of the single layer, reduced gravity model
678 that was intended to mimic the first baroclinic mode of this more complete multi-layered model or of the
679 real ocean.

680 2.6 Understanding the Sverdrup relation; models, models, models*

681 The goal of this essay is to develop some insight for the observed, basin-scale, wind-driven circulation as
682 depicted in Figs. (1) and (2). To go beyond just the flat facts of these field data, we have to grasp at some
683 underlying mechanism or process that links these observations and provides a somewhat deep
684 explanation of O1 and O2 (or other major properties). Here we have chosen the Sverdrup relation. Thus
685 the path toward understanding these fairly straightforward field observations seems to have veered onto a
686 rather abstract and even slightly obtuse vorticity (or thickness) balance.

687 What would it mean to understand the Sverdrup relation, and, how would you know if you have
688 gotten there? Three progressive steps of learning and levels of understanding might be as follows: 1) To
689 begin, you should be able to write down the Sverdrup relation and define the terms in some detail. Then
690 describe the parameter dependence and the geographic variation that follows. 2) Replay a derivation of
691 the Sverdrup relation beginning from a fairly general framework, the time-mean balance of potential
692 vorticity say, and explain the approximations that are appropriate for the basin interior vs. boundary
693 regions. 3) Explain when and where the Sverdrup relation fails, and what else happens instead, at least
694 qualitatively.

695 This kind of abstract understanding derives from models, which in this case are rather drastic
696 idealizations that certainly will not mimic everything that can happen in nature. Some physical processes
697 are represented crudely, especially dissipation by Stokes drag. Nevertheless, the analysis will seek to
698 describe and understand the solutions as they are, warts and all, and then try to draw a bright line
699 distinction between aspects of the shallow water solutions that are in common with comprehensive
700 models — time-dependence and the pattern of Sverdrup transport, especially — and those that are not —
701 anything dependent upon highly resolved vertical structure and the details of the dissipation process. In

702 reaching these judgments we can draw upon the results from much more comprehensive general
703 circulation models, along with data-based studies of the Sverdrup relation.⁶

704 **3 The baroclinic circulation of the 1l-rg solution develops in four** 705 **stages**

706 Now, finally, we are ready to integrate and find a solution. The wind stress is switched on at time = 0 and
707 held constant for about 30 years. This long time is necessary to allow the solution to reach a (nearly)
708 basin-wide steady state, (Fig. 37, bottom panel). The transient circulation develops in four more or less
709 distinct, temporal stages. These are not necessarily contiguous, but rather are characterized by the onset
710 of specific phenomenon.

711 **3.1 Stage 1: Short time, local response of the surface layer**

712 The currents sampled at a high frequency along the south side of the (soon-to-be) subtropical gyre,
713 $(x, y) = (0, -1000)$ km are in Fig. (34). This site has both a significant westward wind stress,
714 $\tau_x = -0.07$ Pa, and a negative stress curl, $\nabla \times \tau = -0.5 \times 10^{-7}$ N m⁻³. This y is equivalent to about 21
715 °N, and $f = 5.11 \times 10^{-5}$ sec⁻¹ and the inertial period is 1.42 days.

716 The surface layer currents (shown as red lines in Fig. 34) exhibit a wide range of phenomena, fast
717 and slow time scales, Ekman flow and geostrophic flow, among others. One way to help sort these out is
718 by a comparison of the full model solution with a comparable solution from a very simple, local, linear,
719 one layer model,

$$720 \quad \frac{\partial u_1}{\partial t} = f v_1 - r u_1 + \frac{\tau^x}{\rho_0 h}, \quad (38)$$

$$721 \quad \frac{\partial v_1}{\partial t} = -f u_1 - r v_1.$$

722 You may notice that these equations are exactly the form used to model the motion of a dense parcel
723 released onto a slope (Part 1, Sec. 5), though here the external force is a wind stress rather than buoyancy.
724 These equations are local in the sense that they apply to what amounts to a single parcel, or since the
725 equations are linear, a single position, that does not interact in any way with its surroundings, i.e., there is

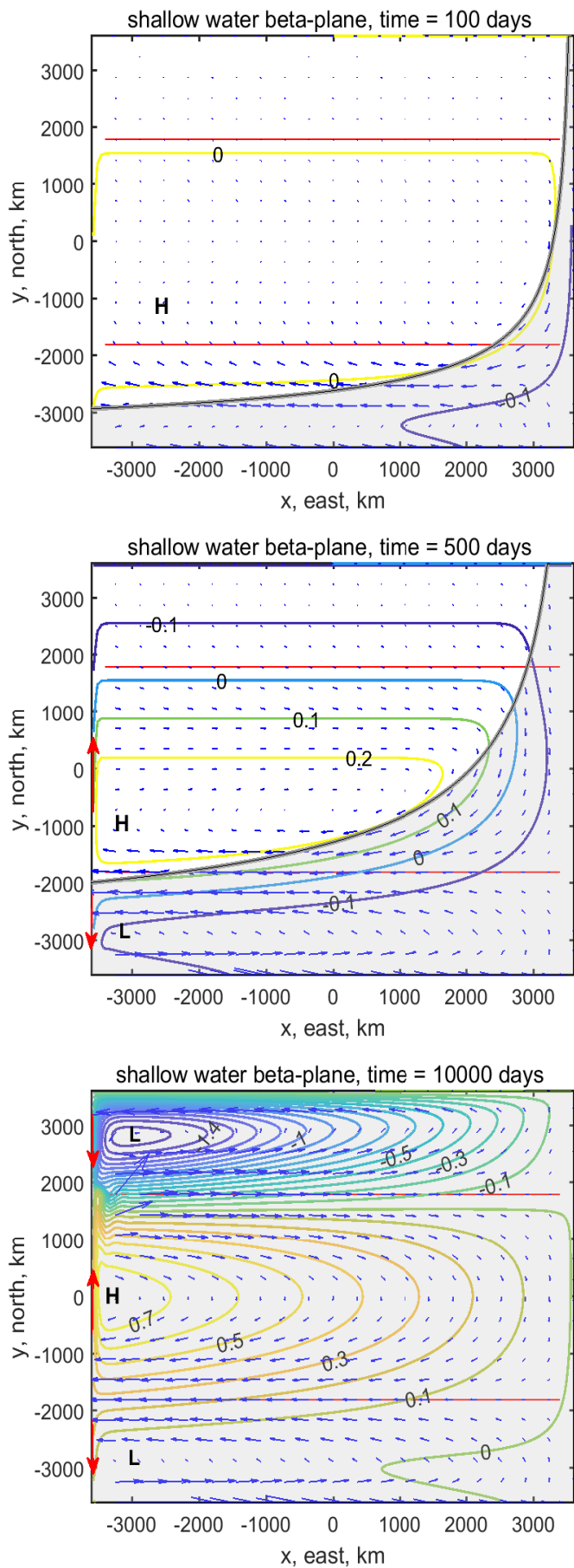


Figure 8: Three snapshots from a wind-driven experiment taken at, from top to bottom, 100, 500 and 10,000 days after the wind stress was switched on. The last time appears to be in a near-steady state throughout the interior of the basin. The thin red horizontal lines are the axis of the westerly and easterly wind stress (Fig. 5). The contours are SSH anomaly computed from thickness anomaly via the reduced gravity approximation; units are Ξ_τ . The small blue arrows are the current, though with the comparatively very large currents within the wbc omitted (shown in Sec. 4.2). The sense of the wbc is indicated by the red arrows on the west edge of the model domain. The largest currents shown here are approx. 0.3 m sec^{-1} . The gray shading extends westward from the eastern boundary at the y-dependent speed of a long Rossby wave, βR_d^2 , and was sketched on top of the solution. Notice that the onset of meridional flow is approximately coincident with the passage of this so-called eastern boundary Rossby wave. An animation of these data is at www.whoi.edu/jpweb/threegyres.mp4

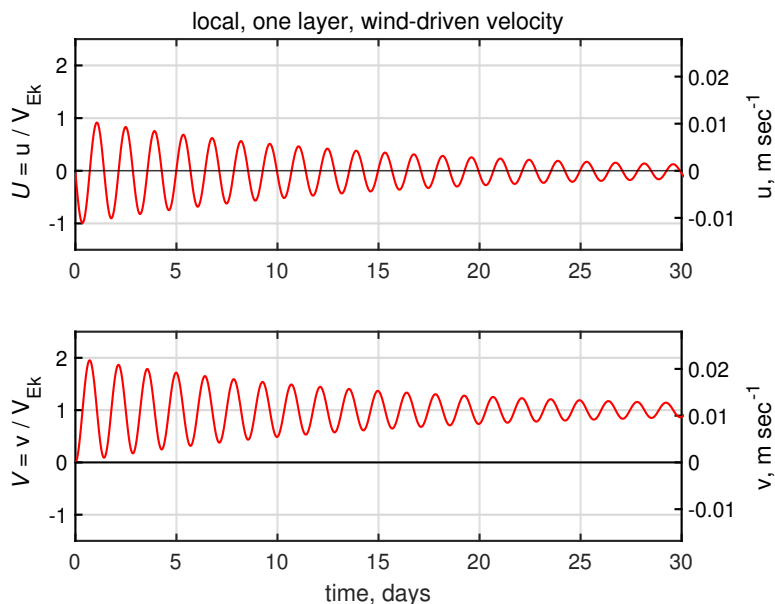


Figure 9: The solution for purely local, damped wind-driven motion, Eqn. (41), that may be compared to the three layer model solution of Fig. (34). There is only one layer in this model, which may be compared to the surface layer of the three layer model. The currents seen here are solely a damped inertial oscillation, and steady Ekman flow, which is northward.

726 no pressure gradient and no advection, very important *non*-local processes that we will get to shortly.
 727 Given an initial condition that is a state of rest $(u, v) = (0, 0)$, the solution for the purely local,
 728 wind-driven velocity is,

$$729 \quad \begin{pmatrix} u_1 \\ v_1 \end{pmatrix} = \frac{\tau^x}{\rho_o f h} \begin{pmatrix} -1 \\ 1 + (r/f)^2 \end{pmatrix} \begin{pmatrix} r/f + \exp(-rt)(\sin(ft) + (r/f)\cos(ft)) \\ -1 + \exp(-rt)(\cos(ft) + (r/f)\sin(ft)) \end{pmatrix}, \quad (39)$$

730 If the intent was to compare this solution to field observations then it would be appropriate to
 731 evaluate (39) for the dimensional currents. However, the goal here is to explore some aspects of the
 732 parameter dependence of the three-layer model and solution, and so it is preferable to use
 733 nondimensional variables, at least in part. We are going to use nondimensional variables for the
 734 dependent variables, here a velocity, but not for the independent variables, i.e., the location and time will
 735 be presented throughout in kilometers and days. An appropriate scale for velocity is the leading factor in
 736 (39), the Ekman velocity scale,

$$737 \quad V_{Ek} = \frac{|\tau^x|}{\rho_o f h}. \quad (40)$$

738 Notice that this is just the wind-stress induced acceleration, Eqn. (28), times the rotation time scale, $1/f$.
 739 Given the wind stress and f at this site the Ekman velocity scale is

$$740 \quad V_{Ek} = 0.005 \text{ m sec}^{-1}$$

741 and the Ekman number

$$742 \quad E = \frac{r}{f} = 0.015.$$

743 In this partially non-dimensional form the solution is

$$744 \begin{pmatrix} u_1 \\ v_1 \end{pmatrix} / V_{Ek} = \left(\frac{\text{sgn}(\tau_x)}{1 + E^2} \right) \begin{pmatrix} E + \exp(-Eft)(\sin(ft) + E \cos(ft)) \\ -1 - \exp(-Eft)(\cos(ft) - E \sin(ft)) \end{pmatrix}. \quad (41)$$

745 By inspection this velocity is the sum of a time-dependent inertial oscillation and a time-independent
746 Ekman flow (Fig. 9).

747 3.1.1 Inertial oscillations*

748 Inertial oscillations are a clockwise rotation of the velocity at a rate close to the local inertial frequency, f .
749 At this site the inertial period is 1.42 days. The amplitude of the inertial oscillation is close to 1 in the
750 nondimensional units, as expected. A check at some other sites verifies that the amplitude does indeed
751 vary as Eqn. (40) suggest that it should. The f (latitudinal) dependence is quite important, since it
752 implies that the amplitude and the phase will vary with y and thus lead to divergent flow and pressure
753 anomalies. The dimensional amplitude is $5 \times 10^{-3} \text{ m sec}^{-1}$, which is unrealistically small because of the
754 excessively thick wind-driven (Ekman) surface layer of the layered model, $h = 250 \text{ m}$, where 50 m or
755 even 25 m would be more appropriate to the subtropical ocean. If the amplitude of inertial oscillations
756 played an important part in the low frequency response (they do not), then this would be a significant
757 shortcoming of a shallow water model. The inertial oscillation of (9) decays with time as $\exp(-Eft)$,
758 e-folding in 15 days due to Stokes drag.

759 There are comparable inertial oscillations in the solution computed by the three layer model of Fig.
760 (34), though with a host of differences in detail. The frequency of rotation is a few percent greater than f
761 (hard to see this in the present figure) and the amplitude decay is considerably faster than is given by
762 frictional e-folding alone as occurs in Fig. (9). There is also an appearance of near-inertial motion in the
763 thermocline layer of Fig. (34) (the green line) where there was no direct wind-forcing. These features
764 taken together indicate that the inertial oscillations in the three layer model solution are the velocity
765 signature of long wavelength, near-inertial gravity waves which propagate vertically and horizontally.
766 The longer term (several weeks) evolution of the inertia-gravity waves is significantly influenced by the
767 variable f of the three layer model, which leads to propagation towards the equator.

768 **3.1.2 Ekman currents and Ekman transport**

769 Along with near-inertial oscillations, the surface layer current in both models also has a time-mean value,
 770 $(\bar{\cdot})$, consistent with Ekman balance modified very slightly by friction, i.e., an Ekman velocity

$$771 \begin{pmatrix} \bar{u}_1 \\ \bar{v}_1 \end{pmatrix} / V_{Ek} = -\text{sgn}(\tau_x) \begin{pmatrix} 1 \\ 1 + E^2 \end{pmatrix} \begin{pmatrix} E \\ 1 \end{pmatrix} \approx \text{sgn}(\tau_x) \begin{pmatrix} 0 \\ -1 \end{pmatrix}. \quad (42)$$

772 The amplitude of the Ekman velocity is equal to the amplitude of the inertial oscillation. The direction is
 773 perpendicular and to the right of the wind stress, and so is northward at the site $(x, y) = (0 - 1000)$ km,
 774 where the wind stress is westward. The Ekman velocity is present within hours of the start-up of the
 775 experiment, and persists for the duration of the experiment, since the wind stress is held steady. The fact
 776 that the Ekman velocity is about the same in the two models means just that the Ekman velocity is the
 777 dominant contributor to the velocity in the surface layer of the three layer model, at least for the first few
 778 weeks.

779 Transport, Eqn. (2), for a layered model is just the velocity multiplied by the appropriate layer
 780 thickness, e.g., for the surface layer, $h_1 v_1$. Insofar as the surface layer alone goes, this doesn't add much
 781 that is new beyond the velocity. However, transport has some very important properties. In the first place,
 782 transport is the amount of water that is in motion at a given spot. At the site shown in Fig. (34), the
 783 surface layer transport is consistent with the expected Ekman transport,

$$784 M_{Ek}^y = \frac{\tau^x}{\rho_o f} \approx 1.3 \text{ m}^2 \text{ sec}^{-1},$$

785 which is a significant magnitude. To find the consequent *volume* transport, this M has to be multiplied by
 786 a horizontal distance, say the width of the North Atlantic basin, to find a volume transport, N , at this y
 787 (latitude) $N_{Ek} = M_{Ek} * 2L = 9.6 \times 10^6 \text{ m}^3 \text{ sec}^{-1}$, or roughly 10 Sv northward. This is about a third of
 788 the total wind-driven meridional transport at this latitude. The Ekman transport will be made up of the
 789 shallowest and generally the warmest water in the water column, and so makes an important contribution
 790 to the heat flux carried by the ocean circulation.

791 It is notable that the amplitude of Ekman transport of (43) goes as $1/f$, and so for a given wind
 792 stress, the Ekman transport is considerably larger in the tropics than in the subpolar region. The same
 793 applies for a given pressure gradient and the amplitude of geostrophic currents, and is a part of the reason
 794 that tropical SSH anomalies are comparatively small (Fig. 2).¹³

¹³The equator is noteworthy with respect to latitudinal dependence insofar as $1/f$ is singular, and hence geostrophy and the Ekman relation imply a blowup of the currents. However, rotation, and thus the Coriolis force, is not a dominant process on

In the specific experiment studied here,

$$M_{Ek}^y = -\frac{\tau^x}{\rho_o f} = -\frac{\xi}{\rho_o f} \sin(\pi y/L). \quad (43)$$

3.2 Stage 2: Zonal geostrophic currents

3.2.1 Divergent Ekman transport changes the mass field

While Ekman transport is significant in its own right, it has an even more important indirect role in generating the changes in layer thickness that lead to geostrophic and Sverdrup transports, discussed in this section and forward. An indirect effect of the wind and Ekman transport becomes apparent within only a few days as a wind-induced change in the mass field (stratification) and thus the pressure field. The sense of the change depends upon the wind stress field: over the northern half of the subtropical gyre, westerly winds produce a southward Ekman transport, while over the southern half of the gyre, easterly winds produce a northward Ekman transport. The Ekman transport thus converges over the region between the westerly and easterly wind maxima, roughly the middle half of the model domain (Fig. 5) and the region that will become the subtropical gyre. The thickness tendency, $\partial h/\partial t$, due to the converging Ekman transport may be calculated from the continuity equation, Eqn. (31) and Eqn. (43),

$$\frac{\partial h_{Ek}}{\partial t} = -\nabla \cdot (h \mathbf{V}_{Ek}) = -\frac{1}{\rho_o} \nabla \times \left(\frac{\boldsymbol{\tau}}{f} \right), \quad (44)$$

where the subscript *Ek* indicates that this accounts for the Ekman transport divergence only, and not the full thickness tendency that will include beta-induced divergence of the geostrophic transport and more. In the special case considered here that $\boldsymbol{\tau}$ is $\tau^x(y)$ only, then

$$\frac{\partial h_{Ek}}{\partial t} = \frac{1}{\rho_o} \frac{\partial}{\partial y} \left(\frac{\tau^x}{f} \right) = \frac{1}{\rho_o f} \left(\frac{\partial \tau^x}{\partial y} - \frac{\beta}{f} \tau^x \right), \quad (45)$$

and includes terms proportional to the wind stress curl and to β times the meridional component of the Ekman transport. Both terms are important (Fig. 10).

or very near the equator, as the Ekman and geostrophic relations presume, and such a blowup does not occur in the numerical solution. A somewhat trivial and parochial reason is that the wind stress has been assumed to vanish on the equator. But even with a significant equatorial stress included, which is more realistic of the real ocean, near-equatorial wind-forced currents are effectively limited by a rapid baroclinic response manifested in (or by) equatorial Kelvin wave propagation (Part 3, Sec. 4), which sets up a pressure gradient that opposes the wind stress within a couple of weeks. In the experiments that we discuss here, the circulation very near the equator is a consequence mainly of the larger scale circulation in the tropical gyre, and so (unfortunately) we won't have much occasion to discuss distinctly equatorial phenomena. We will, however, see this apparent equatorial singularity crop up again.

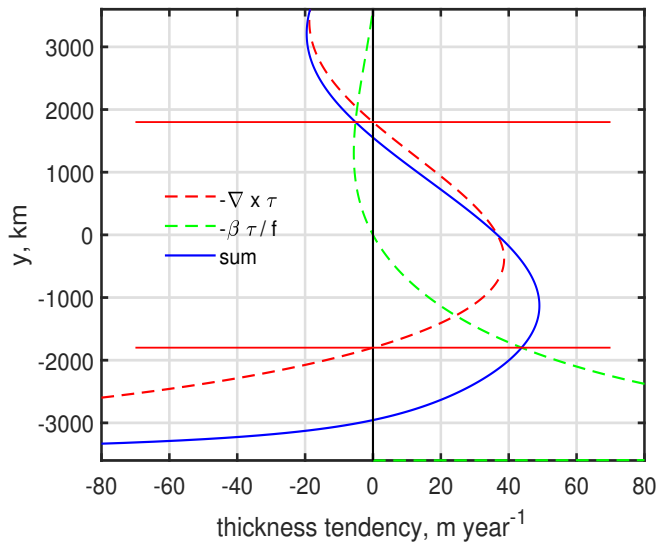


Figure 10: The divergence of the Ekman transport, Eqn. (45) (blue line), given the wind stress field Eqn. (27). Divergence of Ekman transport causes thickness tendency, which is a very significant aspect of the wind forcing on the ocean. At higher latitudes the divergence is due mainly to the curl of the wind stress (dashed red line). At lower latitudes, the beta-induced divergence of the Ekman transport (dashed green line) is appreciable.

816 during the Stage 2 response and notice that the greatest magnitude of thickness change within the
 817 (eventual) subtropical gyre occurs at about $y = -1000$ km during the initial several hundred days (Fig.
 818 10, upper) . As the flow continues to develop, the location of the greatest thickness change migrates
 819 northward and eventually stabilizes on $y = 0$, which is the center of the subtropical gyre and the
 820 maximum magnitude of the negative (clockwise) stress curl. There the thickness tendency is 35 m year^{-1}
 821 and positive, indicating an increasing layer thickness. Since the interface is pushed downwards by the
 822 converging Ekman transport, this sign of thickness tendency is often called 'Ekman pumping'. When
 823 converted to SSH perturbation via the reduced gravity approximation (??), this layer thickness change is
 824 equivalent to a SSH change of about $+0.10$ m per 500 days, see Fig. (11). This raised SSH implies also a
 825 growing high pressure that characterizes the subtropical gyre. Over the tropical and subpolar regions, the
 826 stress curl is positive and hence the interface is raised ('Ekman suction'), the SSH is lowered and
 827 pressure is reduced. Notice in Eqn. (45) that for a given wind stress curl, the thickness tendency and thus
 828 the rate of change of the pressure is $\propto 1/f$ and so for a given stress curl, is greater at lower latitudes.

829 Because the wind stress is constant once the wind stress is switched on, the Ekman
 830 pumping-induced thickness tendency given by Eqn. (45), which starts almost immediately, is also
 831 constant in time (the first 50 days are shown in Fig. 34, lower panel). The actual thickness rate of change
 832 (inferred from Fig. 11) is constant for a period of time that defines what is called here Stage 2 of the
 833 transient response. The duration of Stage 2 depends very much upon location: at $(x, y) = (0, 0)$ the
 834 thickness rate of change is constant for about 1000 days, and then becomes very small as Stage 3
 835 Sverdrup flow begins to develop at that site (more on this in the next section). In this experiment —
 836 conducted in a closed basin and with a wind stress field that is independent of x — it is very compelling

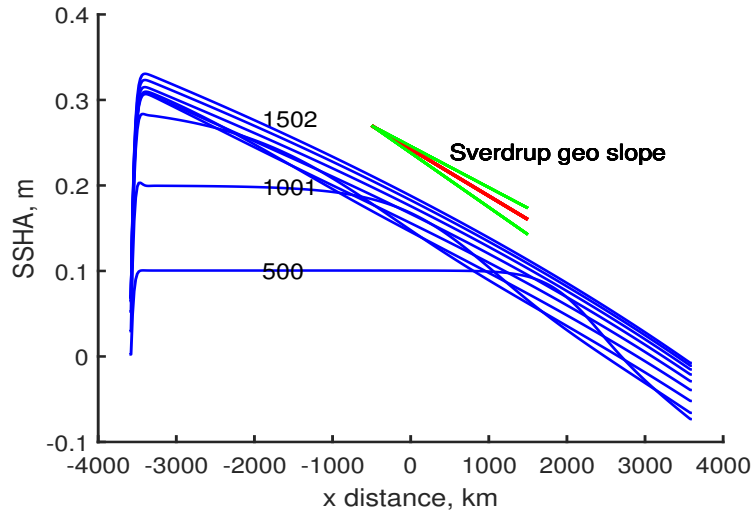


Figure 11: A sequence of sea surface height sections, $\eta(x)$, sampled at 500 day intervals up to 5000 days along $y = 0$, the center of the subtropical gyre (the colors here are random). These were computed from the layer thickness via the reduced gravity approximation, $\eta = (\delta\rho/\rho_o)(h - h_o)$. The Stage 2 response is a uniform rise of the sea surface, approx. 0.1 m per 500 days at this y . Stage 3 begins when the sea surface slopes down to the east and becomes quasi-steady; at $x = 2000$ km (eastern side of the basin) this starts at about 500 days, and at $x = -2000$ km (western side of the basin) the same thing starts much later, at about 1400 days. At this latitude $\tau^x = 0$, and the Ekman transport vanishes. Thus the steady or almost steady meridional transport over the interior region, $x \geq -3400$ km, is geostrophic transport and may be characterized by sea surface slope. The geostrophic sea surface slope expected from the Sverdrup relation Eqn. (1) for this latitude and average layer thickness, $h = 580$ m, is the black line that tilts down to the east. The flanking dashed lines are the sea surface slope for $h = 500$ and $h = 660$ m, which are found at the eastern and western ends of the section where the slope is slightly less and slightly greater than the average.

837 that the duration of Stage 2 is greater with greater distance from the eastern boundary. However, this need
 838 not be the case if the important zonal length scale comes from the wind field rather than the basin
 839 geometry (an experiment considered in Sec. 5.3).

840 3.2.2 Geostrophic currents accompany the changing stratification

841 The change in layer thickness causes an SSH anomaly, η , and thus a hydrostatic pressure anomaly,

842
$$g\eta = g \frac{\delta\rho}{\rho_o}(h - h_o).$$

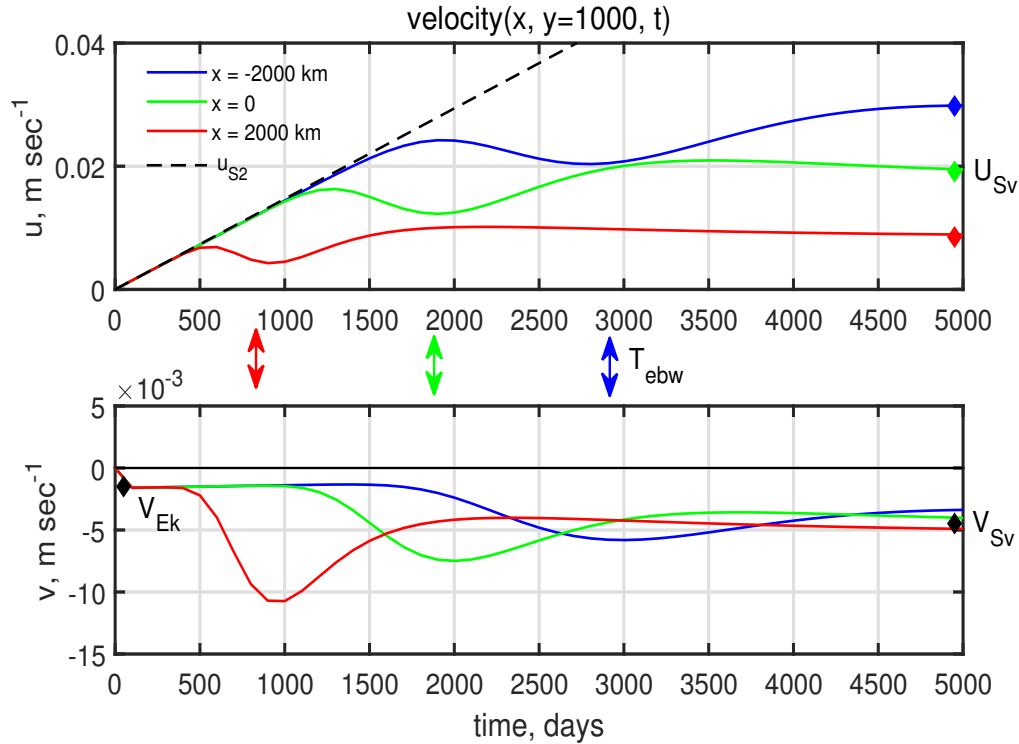


Figure 12: Current components sampled along the northern side of the subtropical gyre, $y = 1000$ km, at three sites: $x = 2000$ km (red line), $x = 0$ (green line), and $x = -2000$ (blue line), which are nearest to farthest from the eastern boundary. The sampling time interval in this figure, 100 days, misses the inertial motions generated at start up (Fig. 34). (This is, admittedly, a complex figure, but one that will repay patient study.) **(upper)** Zonal or east current component. The dashed black line is the estimate by Eqn. (48) of the zonal geostrophic current produced by Ekman pumping at this y and is the same at all x . The actual current follows this very closely for a few hundred or a few thousand days, depending upon distance from the eastern boundary, and then shows a low frequency oscillation as it settles into a quasi-steady state consistent with the expected Sverdrup flow, shown by the colored diamonds on the right margin. Notice that the steady state zonal current increases approximately linearly with distance from the eastern boundary. **(lower)** Meridional or north current component. For short times, $t \leq 300$ days, this is Ekman flow, Eq. (42), which at this y is small. The expected Ekman current is noted by the black diamond at left margin. The red, green and blue double arrows denote the time, T_{ebw} , when a long Rossby wave starting on the eastern boundary at $t = 0$ is expected to arrive at the corresponding x . Notice that this coincides approximately with the transition from Ekman flow to Sverdrup flow in the meridional component (lower panel) and to the end of the constant acceleration of the zonal flow (upper panel). The expected Sverdrup flow at this y and for a nominal h is noted by the black diamond at right.

843 This pressure anomaly develops very slowly compared to $1/f$, and so is accompanied by zonal currents
844 that are very close to geostrophic balance,

$$845 \quad u_{geo} = -\frac{g'}{f} \frac{\partial \eta}{\partial y}. \quad (46)$$

846 Substitution of (45) into (46) gives the time rate change of the geostrophic current due to Ekman
847 pumping alone,

$$848 \quad \frac{\partial u_{S2}}{\partial t} = -\frac{g'}{\rho_o f} \frac{\partial^2}{\partial y^2} \left(\frac{\tau^x}{f} \right), \quad (47)$$

849 and again the subscript $S2$ denotes that this is relevant to the transient Stage 2 only. Because the stress is
850 constant once switched on,

$$851 \quad u_{S2}(y, t) = -\frac{g'}{\rho_o f} \frac{\partial^2}{\partial y^2} \left(\frac{\tau^x}{f} \right) t, \quad (48)$$

852 where t is the time elapsed since the start. In this experiment, the Stage 2 geostrophic current is purely
853 zonal, since the Ekman pumping varies with y only, and it is independent of x , as is the wind stress. This
854 is bound to fail near an impermeable meridional boundary. It fails also on or very near the equator, where
855 the Ekman balance is not appropriate.

856 The Stage 2 geostrophic zonal current (48) evaluated at $y = 1000$ km is sketched onto Fig. (12) as a
857 dashed black line. It gives a very good account of the actual zonal currents in the interior of the basin for
858 a period of time — within the central subtropical gyre, (Fig. 12, the green line was sampled at $x = 0$) Eqn.
859 (48) is valid for about 1000 days, just as noted before in the discussion of the Stage 2 layer thickness. The
860 duration of Stage 2 depends upon both the latitude, being longer at higher latitudes, and longer also with
861 increasing distance from the eastern boundary (the red, green and blue lines of Fig. (12) are at the same y ,
862 but increasing distance from the eastern boundary). An explicit estimate of the duration of Stage 2 will
863 become apparent when we consider the onset of Stage 3 in the next section.

864 The Stage 2 geostrophic current given by (48) is proportional to $1/f^2$, and, all else equal, is much
865 larger at lower latitudes than at higher latitudes (Fig. 13). Most of this essay emphasizes Sverdrup flow
866 and western boundary currents, since these transport sea water properties equatorward and poleward
867 (subtropical gyre) and so are generally of greater significance for Earth's climate. However, this locally
868 wind stress curl-forced, zonal current is a robust signal of the time-dependent circulation, and for
869 example the response of the tropical ocean to an annually-varying wind (O2 of Sec. 1.1.2) appears to be
870 at least in part of this kind (more on this in Sec. 5.1).

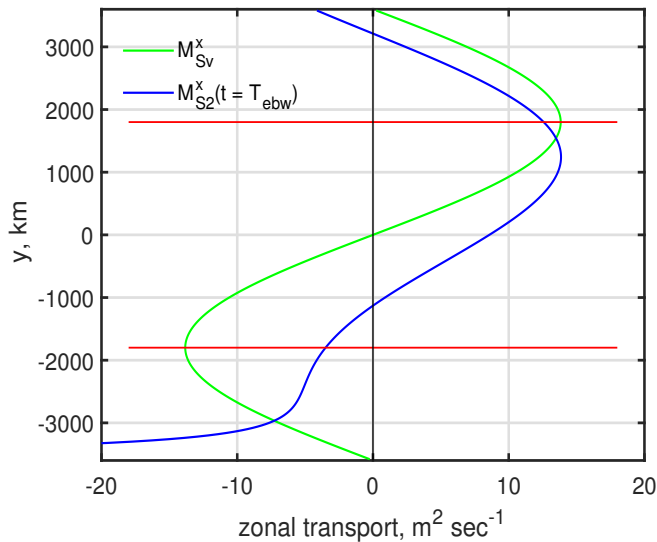


Figure 13: The zonal transport (per unit width) that accompanies the Sverdrup relation (green line) and the Stage 2 zonal current evaluated at $t = T_{ebw}$ (blue line) argued in Sec. 3.1.3. At higher latitudes these currents are somewhat similar, but they are quite different at lower latitudes. The initial zonal currents in the interior closely match the Stage 2 profile, while the steady state zonal currents follow the Sverdrup profile.

871 3.3 Stage 3: Blocking by the meridional boundaries and the onset of Sverdrup 872 flow

873 Imagine that the meridional boundaries are removed, and that the no-flow boundary condition on those
874 boundaries is replaced by a symmetric or reentrant condition that $u(x = -L) = u(x = L)$, and the same
875 for other variables. The domain would then be an east-west oriented channel, as more or less actually
876 occurs in the Antarctic Circumpolar region. In a channel domain, the zonally-oriented thickness
877 anomalies and geostrophic currents of the Stage 2 response would grow until the currents either became
878 unstable and began to spread vertically and horizontally, or, drag on the current reached an equilibrium
879 with the wind stress. Because the present experiment is set within an enclosed, finite basin having
880 impermeable meridional boundaries, something quite different happens first: the zonal flow that
881 approaches a meridional boundary is blocked, and must turn either north or south. The meridional
882 boundaries thus have the effect of breaking the zonal symmetry that characterizes the Stage 2 response.
883 As this 'blocking effect' of meridional boundaries becomes important, the overall pattern of the layer
884 thickness anomaly and geostrophic currents begins to resemble a closed, gyre-like circulation, e.g.,
885 within the eastern part of the subtropical gyre, $x > 2000$ km, this is evident by about 500 days (Fig. 37).

886 The meridional flows can be described in two distinctly different regions: by far the greatest part of
887 the basin develops a very slow Sverdrup flow, and there is a comparatively narrow western boundary
888 region having a width of about 100 km.

889 **3.3.1 Sverdrup flow in the basin interior**

890 The blocking effect of the eastern meridional boundary — a zonal tilt of SSH and thus a change from
 891 purely zonal to at least partly meridional flow — propagates westwards into the interior of the basin. At
 892 $y = 0$, equivalent to 30° N, the propagation occurs at the slow but steady rate of about 3 km per day (Fig.
 893 37), which is roughly the westward propagation speed of mesoscale eddies at that latitude (Part 3, and
 894 reviewed briefly in Sec. 1.1).

895 There are two fairly compelling reasons to conclude that this westward propagation of eastern
 896 boundary blocking is the same thing as the westward propagation of a long, divergent Rossby wave
 897 reviewed in Sec 1.1 (and more detail in Part 3, Sec. 2.5). First, the balance of potential vorticity is
 898 consistent with long Rossby wave motions. A β -effect (Part 3) begins immediately with the meridional
 899 component of the current. Because the horizontal scale of the currents is the scale of the wind stress and
 900 very much larger than the radius of deformation, the β -effect produces mainly a change in layer thickness
 901 rather than a change of relative vorticity (Part 3, Section 2.4), which remains very, very small, i.e.,
 902 $\nabla \times \mathbf{u} \ll f$ (this is not true near the western boundary, however). Thus the potential vorticity balance in
 903 the vicinity of the spreading eastern boundary blocking is linear and divergent, Eqn. (2), in common with
 904 long Rossby waves. The motion is also very nearly geostrophic, and so the first order wave equation (13)
 905 is expected to be valid and predicts this westward propagation. Second, judging from Fig. (37), the
 906 westward propagation of eastern boundary blocking is markedly faster at lower latitudes. This invites a
 907 direct comparison to the long Rossby wave speed (Eqn. 12), which has been used to define a gray-shaded
 908 mask that extends westward from the eastern boundary by

$$909 \quad X = C_{longRo} t = -\beta \frac{C^2}{f^2} t, \quad (49)$$

910 Fig. (37).¹⁴ The long Rossby wave speed varies strongly with latitude; the gravity wave speed C is
 911 somewhat reduced at higher latitudes due to reduced stratification, but much more important at this early
 912 stage is the $1/f^2$ dependence, which implies much larger C_{longRo} at lower latitudes. Notice that the
 913 disruption of the Stage 2, zonal geostrophic flow is indeed closely coincident with the expectations of
 914 (49) at all latitudes (equator aside, Fig. 37). Given this line of evidence, the westward propagation of the
 915 boundary blocking effect will be referred to as an 'eastern boundary Rossby wave', or 'ebw', despite that
 916 the profile $h(x,t)$ looks nothing like an elementary wave (Fig. 11).

917 The end of the Stage 2 local response to Ekman pumping and the start of the Stage 3 non-local or

¹⁴The equatorial limit $f \rightarrow 0$ is handled by assuming that the westward wave speed can be no faster than the fastest, westward propagating equatorial Rossby wave, $-2C/3 \approx -2 \text{ m sec}^{-1}$. See Part 3, Sec. 3 for a little more on equatorial wave dynamics.

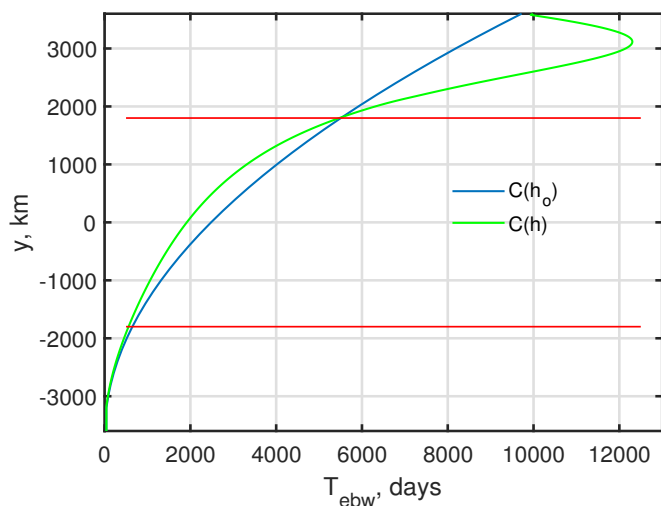


Figure 14: Transit time from the eastern boundary to the western boundary at the long Rossby wave speed. The blue line assumes the nominal layer thickness $h_o = 500$ m for evaluating the baroclinic gravity wave speed, while the green line uses the actual, steady, zonal average thickness, which is somewhat different, especially in the western part of the subpolar gyre where $h \approx 100$ m. The expected transit times for the gyre centers are: tropical gyre, 350 days; subtropical gyre, 2500 (2000) days; subpolar gyre, 7500 (12000) days.

918 basin scale response may then be estimated by

919
$$\text{Stage 2} \rightarrow \text{Stage 3} : t = T_{eww}, \tag{50}$$

920 where

921
$$T_{eww} = - \frac{(L-x)}{C_{longRo}} \tag{51}$$

922 with $(L-x)$ the distance from the eastern boundary. Thus T_{eww} is $T_{eww}(x,y)$ since C_{longRo} varies with y .
 923 Subsequent to T_{eww} , the volume transport has a significant meridional component that approximates
 924 Sverdrup balance, Eqn. (1), Figs. (11) and (12), lower.

925 Judging from Fig. (12), the flow does not switch instantaneously from zonal to purely Sverdrup at
 926 $t = T_{eww}$. The eastern boundary wave has a very gradual leading edge, Fig. (11), and a close Sverdrup
 927 balance requires as much as $2 * T_{eww}$, which can be another few hundred or even a thousand days,
 928 depending upon latitude and distance from the eastern boundary. The key point is that the time required
 929 for the eastern boundary (blocking) effect to reach a given point in the interior is proportional to T_{eww} , and
 930 thus is strongly dependent upon latitude and distance from the eastern boundary. In this important
 931 respect, low latitude oceans exhibit a comparatively fast response to changing wind stress. The
 932 latitudinal-dependence of the long Rossby wave speed Eqn. (12) is thus a very prominent, qualitative
 933 feature of the developing gyre circulation in this experiment, and often in the real ocean (Part 3, Sec. 2.6).
 934 (see Sec. 8.2, 5)

935 **3.3.2 Western boundary currents**

936 At the same time that the interior is developing very slow and broadly distributed currents, something
 937 quite different is happening near the western boundary. The Stage 2 response includes zonal currents that
 938 impinge on the western boundary just as much as occurs on the eastern boundary. The result is
 939 necessarily meridional currents along the western boundary that are subject to a beta effect. Propagation
 940 of this western boundary blocking into the interior by wave propagation requires an *eastward* group
 941 velocity. You may recall from Part 3, Sec. 2.3, that while short Rossby waves do have an eastward group
 942 velocity, the maximum eastward group velocity of baroclinic Rossby waves is very, very slow, only a few
 943 hundred meters per day, which is just a few percent of the western group velocity of long waves, C_{longRo} .
 944 Moreover, eastward group velocity obtains only for short waves, $kR_d \leq -1$ and $k \leq 0$. Such short waves
 945 are just barely resolved in the present numerical solution, and so it is not too surprising there is very little
 946 evidence of eastward propagation, and the meridional currents along the western boundary are effectively
 947 trapped to the boundary on a width of 50 - 100 km (Fig. 15). As we will see below, the e-folding width of
 948 the wbc is roughly the local radius of deformation. The resulting western boundary current is
 949 comparatively very fast, up to 1 m sec^{-1} . Within the subtropical gyre, the flow near the western boundary
 950 is northward, opposite the Sverdrup flow in the interior. It begins to appear within a few hundred days
 951 after the start of the wind stress, and reaches its full, steady state amplitude in about 1500 days. This is
 952 about the same time scale on which the subtropical gyre reaches steady state Sverdrup flow.

953 The water that makes up the western boundary current of the subtropical gyre flows into the
 954 boundary current from the eastern side. This inflow begins with the start of the Stage 2 zonal current, and
 955 continues into the steady state. Assuming that the inflowing water conserves its potential vorticity and
 956 that the across stream momentum balance is geostrophic, we can make an estimate of the boundary
 957 current profile and width. (See Stommel (1966)⁴, Ch. 8, who has an interesting discussion of this applied
 958 to the actual Gulf Stream.) The relative vorticity is approximated well by the x variation of the north
 959 component of the current, and hence the potential vorticity inside and just outside of the western
 960 boundary current are

$$961 \quad \frac{f + \frac{\partial v}{\partial x}}{h} = \frac{f}{h_0}, \quad (52)$$

962 where h_0 is the thickness just outside the boundary current. If we evaluate this at $y = 0$, $h_0 \approx 600 \text{ m}$. The
 963 momentum balance is very nearly geostrophic,

$$964 \quad fv = g' \frac{\partial h}{\partial x},$$

965 which may be combined with (52) to form a single equation for the boundary current velocity,

$$966 \quad \frac{\partial^2 v}{\partial x^2} = \frac{f^2}{g'h_0} v. \quad (53)$$

967 This has exponential solutions

$$968 \quad v(x) = V_0 \exp(\pm((x+L)/R_d), \quad (54)$$

969 where $R_d = \sqrt{g'h}/f$ is the familiar radius of deformation. Suitable boundary conditions are that $v \rightarrow 0$
 970 as $x+L$ becomes large, which selects the minus sign in the exponential, and then we are free to choose
 971 the amplitude, V_0 . For the central latitude of the subtropical gyre, $y = 0$ of Fig. (17), $V_0 = 1.0 \text{ m sec}^{-1}$.
 972 The solution for $v(x)$ is then complete, and the corresponding geostrophic thickness, represented here by
 973 the SSH anomaly η , may then be easily computed as well (Fig. 17, red lines). These make quite good
 974 representations of the actual velocity and thickness (or η), and hence we can conclude that the width of
 975 the western boundary current is approximated well by the radius of deformation, the natural length scale
 976 of the shallow water model. That is a neat and satisfying result that we will cite repeatedly in the
 977 description of the circulation. However, closer inspection and thought suggests that there may be more to
 978 this than the simple, local inflow model takes account of. First, this simple model doesn't work so well
 979 along the northern side of the subtropical gyre, $y = 1000 \text{ km}$ (upper panel of Fig. 15) where the boundary
 980 layer current appears to have a reversal offshore that is not captured by the monotonic profile (54). In one
 981 respect that is not all bad, since that region is characterized by *outflow* from the wbc into the interior, not
 982 an inflow. So, there is evidently more to the wbc dynamics than just (53). Second, the water that makes
 983 up the wbc at $y = 0$, say, came mostly from lower latitudes, not from a local inflow. If the wbc current
 984 was q conserving along stream, then the q at that latitude should be lower than the local q . Later we will
 985 see that frictional effects are expected to be significant in the western boundary current, and friction acts
 986 to increase q along the path of the current. Friction implies a length scale that, for the r used here, is the
 987 same order as R_d (Sec. 4.2.2). It appears that while Eqn. (53) works very well in a numerical sense, local
 988 inflow and q conservation are not a complete explanation.

989 A very important bulk property of a western boundary current (or any current) is volume transport,

$$990 \quad N_{wb} = \int_{-L}^{-L+L_{wb}} v h dx,$$

991 where $L_{wb} = 150 \text{ km}$, by inspection (or several times R_d). The speed and the volume transport of the
 992 western boundary currents (Fig. 16) increase roughly linearly with time until reaching full amplitude and
 993 steady state several hundreds of days after arrival of the eastern boundary Rossby wave on the western
 994 boundary; at $y = 0$, equivalent to 30° N , this occurs at about 1500 days. As discussed above, the arrival of
 995 an eastern boundary Rossby wave is not the dramatic event that the words seem to promise. And too, the
 996 coincidence in time does not imply that the eastern boundary Rossby wave is the cause of the western
 997 boundary current except in a very indirect way: the arrival of the eastern boundary wave implies that the
 998 interior region to the east and equatorward (subtropical gyre) is close to being in steady state with regards
 999 to meridional transport and the Sverdrup relation.

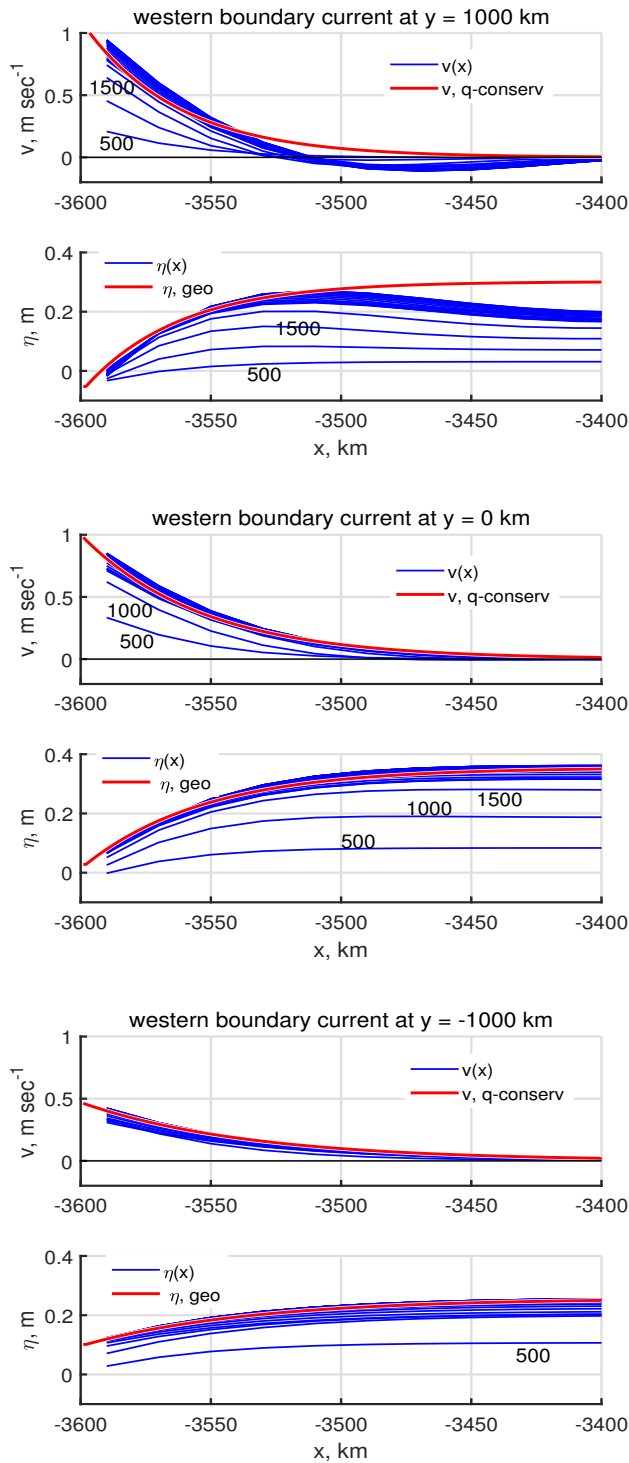


Figure 15: Zonal profiles of the north velocity and the SSH anomaly within 200 km of the western boundary at three sites within the developing subtropical gyre: **(upper)** $y = 1000$ km, on the north side of the subtropical gyre, **(middle)**, $y = 0$, the center of the subtropical gyre, and **(lower)** $y = -1000$ km, the south side of the subtropical gyre. Profiles are shown as the blue lines at 500 day intervals. The north velocity expected for a q-conserving inflow is shown as the red line, an exponential with the x scale being the radius of deformation, at $y = 1000$ km, $R_d = 36$ km; at $y = 0$, $R_d = 45$ km, and at $y = -1000$ km, $R_d = 64$ km (discussed in Sec. 3.2). The corresponding SSH anomaly profiles are computed from the respective q-conserving velocity using geostrophy (also plotted as a red line). Notice that currents and stratification at the more southerly site (lower panels) reach steady state in about 500 days, while the higher latitude site (upper panels) requires about 2000 days.

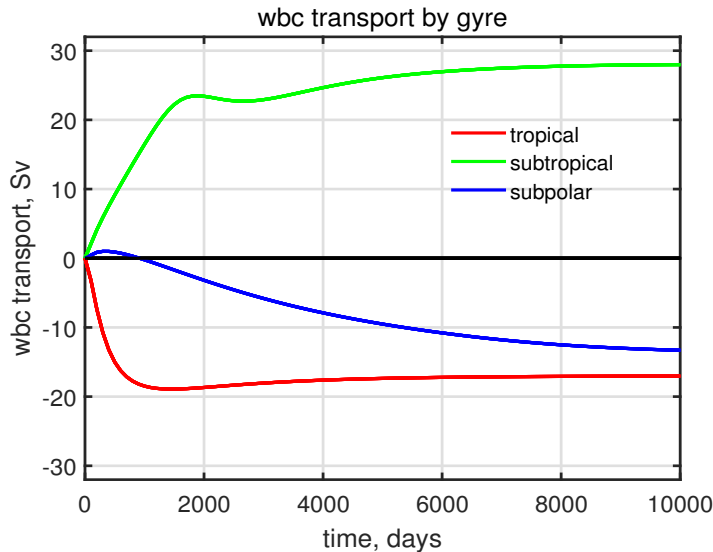


Figure 16: Meridional volume transport N_{wb} within the western boundary currents of the three gyres. These were sampled at the north-south center of the gyres. Notice that the wbc of the tropical gyre reaches a steady state within about 700 days after the start of the experiment, while the wbc of the subpolar gyre requires much longer, roughly 12,000 days.

1000 The immediate cause of a western boundary current is zonal inflow: in the subtropical gyre, there is
 1001 an inflow to the wbc at latitudes $0 > y > -L/4$, and an outflow at latitudes $L/4 > y > 0$. During the
 1002 first one thousand days of the experiment, the zonal current near the wbc is mainly the Stage 2
 1003 geostrophic flow discussed in the previous subsection. As time runs, the inflow is better described as the
 1004 Sverdrup zonal flow. From this we can infer that the time scale for development of the wbc is
 1005 proportional to U_{S2} and thus proportional to $1/f^2$, i.e., much faster at lower latitudes (Fig. 15, cf upper
 1006 and lower panels). The same attends the volume transports of the wbc in the three gyres: — wbc steady
 1007 state requires about 1000 days in the tropical gyre, and about 10,000 - 12,000 days in the subpolar gyre
 1008 (Fig. 16), a factor of roughly ten.

1009 3.3.3 Changing stratification*

1010 The western boundary currents of the tropical and subpolar gyres are southward, and opposite the
 1011 Sverdrup flow in those regions. This suggests that perhaps the wbc just mirrors (compensates) the
 1012 Sverdrup flow of the interior. To test this, we can evaluate the volume fluxes over a control volume that
 1013 we are free to choose: for this case, the entire southern half of the basin (the light green shading of Fig.
 1014 17). The areally integrated continuity equation appropriate to a control volume having an area A is

$$1015 \quad A \frac{dh_{avg}}{dt} = \oint h \mathbf{V} \cdot \mathbf{n} ds$$

1016 since our shallow water model has no source term, i.e., no mechanism to convert upper layer water to
 1017 abyssal water, for example. Thus the areal-average thickness of the layer within the control volume can

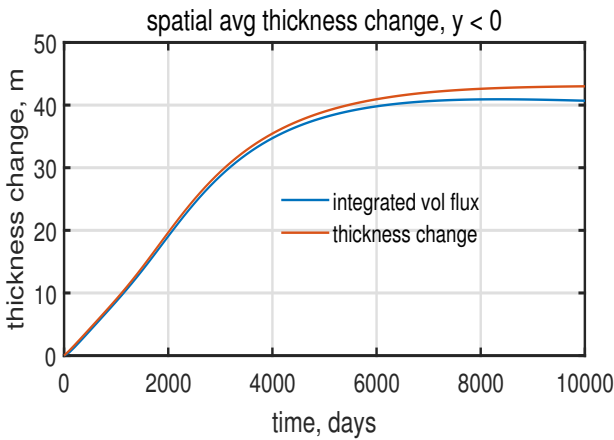
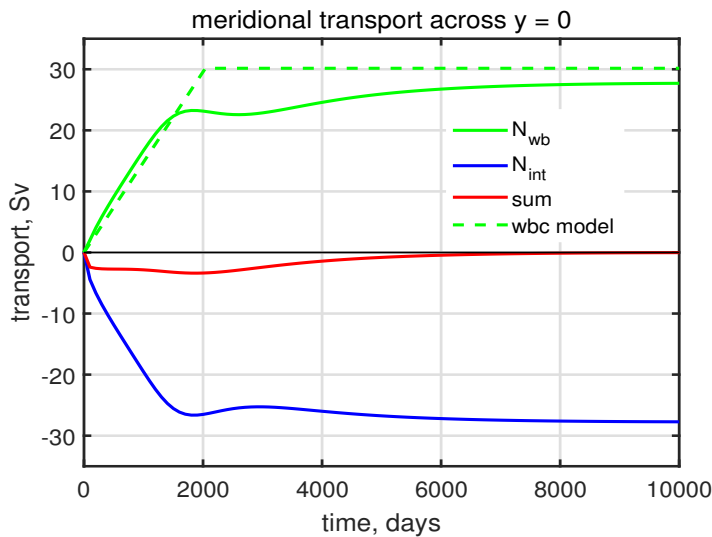
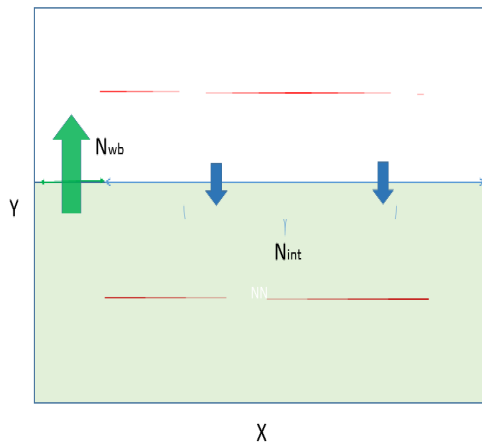


Figure 17: **(upper)** A control volume (light green area A) defined over the southern half of the basin. The volume transport through $y = 0$ is evaluated over a western boundary, N_{wb} , and an interior, N_{int} . **(middle)** The volume transports through $y = 0$ (green and blue lines) and their sum (red line). The dashed green line is a model of wbc transport, Eqns. (55) and (56). **(lower)** The time-integrated net volume flux into the control volume (blue line) and the observed thickness change over the control volume (red line), about 40 m. Given the adiabatic continuity equation (31), these should be exactly equal.

1018 change only if there is a net volume flux across the horizontal sides of the control volume. In practice we
 1019 can break up the line integral into pieces that represent the flow across specific sides of the control
 1020 volume, e.g., in this case

$$1021 \quad N_{int} = \int_{-L+L_{wb}}^L v h dx,$$

1022 is the volume transport across $y = 0$ in the interior of the basin (no need to identify this as Sverdrup flow),
 1023 and the volume flux of the comparatively very narrow and intense northward flowing western boundary
 1024 current (Fig. 15) is N_{wb} , already noted. The integrated mass balance (continuity equation) then reads

$$1025 \quad A \frac{dh_{avg}}{dt} = N_{int} + N_{wb}.$$

1026 Either of the volume flux terms are considerably larger than the storage term, but they do not sum to zero:
 1027 during the first several thousand days of the experiment there is a small but significant net meridional
 1028 transport across $y = 0$, $N_{Sv} + N_{wb}$, (the red line of Fig. 17, middle). The subtropical gyre is a region of
 1029 increased layer thickness, and thus elevated SSH and higher pressure. Indeed, the subtropical gyre is
 1030 characterized mainly by this high pressure (although we discuss mainly the associated currents). The
 1031 volume of fluid required to thicken the layer in the region south of $y = 0$ is provided by (must be provided
 1032 by) the net (basin-wide) meridional volume flux across $y = 0$ (Fig. 17, lower). As the region to the south
 1033 of $y = 0$ reaches a steady state and $\partial h / \partial t = 0$, which requires a little more than 5000 days, the net
 1034 volume flux across $y = 0$ also vanishes. Note that this is a considerably longer than the time required to
 1035 reach a steady state within the subtropical gyre alone.

1036 3.3.4 A simple model of transport in a time-dependent wbc*

1037 We can construct a very simple estimate of the time-dependent western boundary transport on the
 1038 assumption that the transport will be opposite and equal to the meridional Sverdrup transport to the east
 1039 of the eastern boundary Rossby wave, i.e., as if

$$1040 \quad N_{int} + N_{wb} = 0.$$

1041 and now $N_{int} = N_{Sv}$. While the eastern boundary wave is in transit across the basin,

$$1042 \quad 0 < t < T_{ebw}(x = -L, y); \quad N_{wb} = -\frac{\nabla \times \tau}{\rho_o \beta} C_{longRo} t = -N_{Sv} \quad (55)$$

1043 The wind stress curl and the long Rossby wave speed are evaluated at the y of the wbc observation, in Fig.
 1044 (16), the center of the subtropical gyre, $y = 0$. After the wave arrives on the western boundary, the

1045 western boundary transport is assumed to exactly compensate the steady state Sverdrup transport across
1046 the basin interior and so for longer times,

$$1047 \quad t > T_{ebw}; \quad N_{wb} = constant = - \frac{\nabla \times \tau}{\rho_o \beta} 2L. \quad (56)$$

1048 This estimate (55) and (56) is shown as the green dotted line of Fig. (17) middle, and is a plausible first
1049 description of the actual (numerical) boundary current transport, though far from perfect. There are two
1050 ways we know that this model and this estimate are inconsistent in detail with the numerical solution: the
1051 transition from Stage 2 purely zonal, local flow to Stage 3 Sverdrup flow is not instantaneous as Eqn. (55)
1052 assumes, and, the northward wbc transport does not return all of the southward Sverdrup transport during
1053 the first several thousand days of the experiment when some fluid is stored at the rate of several Sv within
1054 the thickening layer south of $y = 0$. Those fairly significant details aside, what is most striking and very
1055 robust is that a wbc develops much faster in the tropical gyre, within very roughly 1000 days, than in the
1056 subpolar gyre, where the time scale is closer to 10,000 days (Fig. 16). This very large difference in the
1057 rise time of the wbc in these gyres is a consequence of the $1/f^2$ dependence of the Stage 2, locally
1058 wind-forced geostrophic current, Eqn. (48), and of the long Rossby wave transit time, Eqn. (51).

1059 3.4 Stage 4: Intra- and inter-gyre exchange, and basin-wide steady state

1060 The three gyres come into steady state at quite different times, as described above, and clearly the laggard
1061 is the subpolar gyre. Even after 10 years, most of the subpolar region is still in Stage 2 and continuing to
1062 lose volume since $\nabla \times \tau > 0$ (Ekman suction). The decrease of layer thickness within the subpolar gyre is
1063 quite pronounced, with h eventually reaching a minimum of about 100 m just offshore of the western
1064 boundary current (Fig. 37, bottom). The basin-wide volume of the layer is conserved and so the fluid that
1065 is expelled from the subpolar gyre is absorbed into the subtropics and tropics where the layers continue to
1066 slowly thicken more or less uniformly over the basin. . A literal steady state of the subtropics, i.e.,
1067 constant h and constant \mathbf{v} , here dubbed Stage 4, requires that the entire basin, subpolar region included,
1068 must be swept by an eastern boundary Rossby wave. Thus a basin-wide steady state requires an elapsed
1069 time

$$1070 \quad \text{Stage 4: } t = \max(T_{ebw}) = \frac{2L(f_o + \beta L)^2}{\beta C^2},$$

1071 where \max is evaluated over the basin as a whole. If we use a nominal value of the gravity wave speed,
1072 $C = 3 \text{ m sec}^{-1}$, then we find $\max(T_{ebw}) \approx 9200$ days. In fact, the numerical solution indicates a
1073 somewhat longer time, closer to 10,000 -12,000 days, mainly because the gravity wave speed is
1074 significantly reduced within the subpolar gyre (Fig. 14) due to the greatly reduced layer thickness in
1075 especially the western part of the gyre (Fig. 37, lower panel). (see Sec. 8.2, 4)

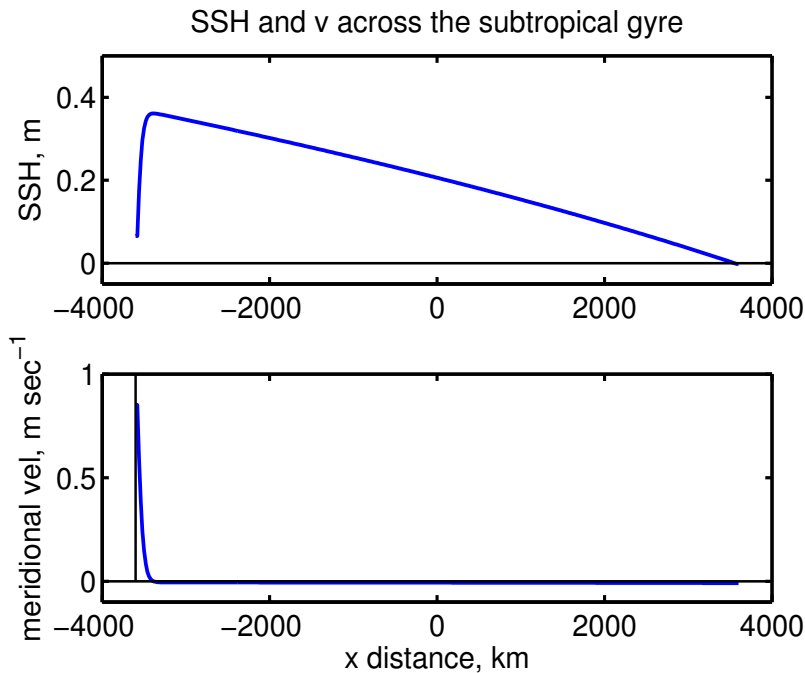


Figure 18: **(upper)** A zonal section of SSH across the center of the subtropical gyre, $y = 0$, computed from layer thickness anomaly via the reduced gravity approximation. The basin-scale variation of SSH is much like that seen in the North Atlantic (Fig. 1); a very narrow western boundary current and a broad interior with almost uniform slope down to the east. Notice, though, that the amplitude of the SSH high in this model solution is considerably less than is observed in the real North Atlantic subtropical gyre (about which more in Sec. 7). **(lower)** The meridional velocity along the section above. The velocity is very nearly geostrophic and is northward and very fast in a thin western boundary current, up to about 1 m sec^{-1} . The interior, meridional velocity is southward and very slow, a little less than 0.01 m sec^{-1} .

1076 4 The (almost) steady circulation

1077 The currents and stratification in the interior of the basin eventually reach an instantaneous steady state,
 1078 $\partial(\cdot)/\partial t = 0$. However, there is one region where the flow never becomes even approximately steady, the
 1079 confluence of the western boundary currents of the subtropical and subpolar gyres at around $y = 1800 \text{ km}$.
 1080 There the colliding western boundary currents meander and produce intense, mesoscale eddies of both
 1081 signs. The eddies remain close to the western boundary, and do not appear to affect the interior region.
 1082 The confluence region does become steady in the statistical sense that the eddy amplitude, size and
 1083 frequency are no longer changing after about 10,000 days. So, whenever we say 'steady' in reference to
 1084 the basin-wide circulation, read that as a shorthand for steady excepting the wbc confluence region.

1085 One straightforward way to characterize the basin-wide, steady circulation is to simply make a cut of
 1086 SSH anomaly and northward velocity through the center of the subtropical gyre Fig. (18), which may be
 1087 compared to Fig. (1). There is a comparatively very narrow western boundary region, e-folding on the
 1088 radius of deformation and so the full width is $O(100 \text{ km})$, within which SSH slopes up to the east and the

1089 current is northward and fast, up to 1 m sec^{-1} . Over the much broader interior region — the rest of the
 1090 basin — there is a quasi-linear decrease of SSH all the way to the eastern boundary (Fig. 18). Given the
 1091 zonally uniform wind stress curl of the model winds, this nearly constant slope of SSH would be
 1092 expected for a linear Sverdrup interior for which $\delta h \ll H_o$. This is the shallow water model-equivalent of
 1093 the east-west asymmetry of the observed wind-driven ocean circulation noted as O1 in Sec. 1.1.

1094 4.1 A streamfunction depiction of the circulation

1095 A second useful way to characterize the basin-wide steady circulation is to construct a map of the
 1096 streamfunction. When the solution is in steady state, $\partial h / \partial t = 0$, the volume transport, $\mathbf{M} = H\mathbf{V}$, is
 1097 nondivergent, $\nabla \cdot \mathbf{M} = 0$. In that case the vector field $\mathbf{M}(x, y)$ may be represented by a scalar field, the
 1098 streamfunction, $\Psi(x, y)$, without loss of information. The streamfunction is related to the east and north
 1099 components of \mathbf{M} by

$$1100 \quad \frac{\partial \Psi}{\partial y} = HU \quad \text{and} \quad \frac{\partial \Psi}{\partial x} = -HV, \quad (57)$$

or in a vector form,

$$\mathbf{M} = -\mathbf{k} \times \nabla \Psi$$

1101 where the upper case H and U, V are the steady state thickness and velocity components. The sign
 1102 convention of (57) is arbitrary, and may be reversed in some applications. The streamfunction may be
 1103 computed from the vector field by integrating either of (57). Here we integrate the HV term westward,
 1104 starting from the eastern boundary,

$$1105 \quad \Psi(x, y) = \Psi(L, y) - \int_L^x H(x, y)V(x, y)dx. \quad (58)$$

1106 The dimensions (units) of this streamfunction is volume transport, $\text{m}^3 \text{ sec}^{-1}$. The volume transport of
 1107 major ocean currents is in the range $1 - 150 \times 10^6 \text{ m}^3 \text{ sec}^{-1}$ and often reported in a non-SI but widely
 1108 used and accepted unit, 'Sverdrups', with $1 \text{ Sv} = 10^6 \text{ m}^3 \text{ sec}^{-1}$. The normal component of the velocity
 1109 vanishes on all of the side walls, and hence $\Psi(L, y) = \text{constant}$, that may as well be taken to be zero. It
 1110 would be equally valid to perform an integration of HU in the y direction. The resulting streamfunction
 1111 lines (Fig. 19, left) are everywhere parallel to \mathbf{M} , and hence the streamfunction makes a very clear
 1112 presentation of the direction of the underlying vector field. With this choice of sign, lower values of Ψ
 1113 are to the right of the vectors (which is opposite the geostrophic relationship for SSH). The density of
 1114 streamfunction lines is proportional to the magnitude of \mathbf{M} and notice that $\partial \Psi / \partial x$ is very large in thin
 1115 western boundary regions where the wbc current is correspondingly very large compared to the currents
 1116 in the interior of the basin.

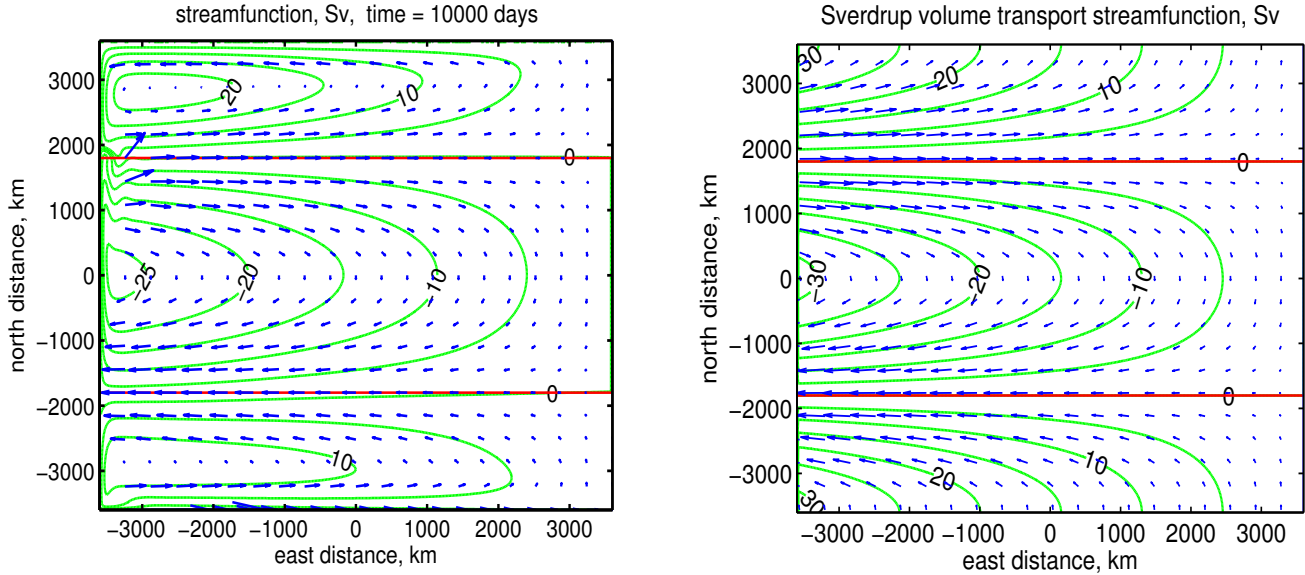


Figure 19: **(left)** The volume transport streamfunction (green lines) computed from the steady state numerical solution by integrating Eqn. (58) starting from the eastern boundary. Labeled in Sverdrups, $10^6 \text{ m}^3 \text{ sec}^{-1}$. The blue vectors are the volume transport per unit width, \mathbf{M} , and are parallel to lines of constant streamfunction. The very large \mathbf{M} vectors in the western boundary regions are omitted here but shown in a later Fig. 14. The red horizontal lines are the axes of the westerly and easterly winds, and also approximate gyre boundaries. **(right)** The Sverdrup volume transport streamfunction (green lines) computed from the wind stress of the numerical experiment (Fig. 5) and Eqn. (59) and starting from the eastern boundary. In the numerical model-computed streamfunction field at left, $\Psi = 0$ is found on all of the boundaries, indicating no normal flow through the boundaries, as should hold exactly. The Sverdrup streamfunction at right can not satisfy a zero normal flow condition on more than one boundary, here chosen to be the eastern boundary.

1117 Sverdrup transport may also be represented by a streamfunction (Fig. 19, right), here computed
 1118 from Eqns. (1) and (58) and integrating westward from the eastern boundary,

$$1119 \quad \Psi_{Sv}(x, y) = \Psi_{Sv}(L, y) + \frac{1}{\rho_o \beta} \int_L^x \nabla \times \tau(x, y) dx. \quad (59)$$

1120 The starting value is taken to be $\Psi_{Sv}(L, y) = 0$ for all y , which ensures that there is no normal flow
 1121 through the eastern boundary. Since only one integration is needed to compute Ψ_{Sv} , no other boundary
 1122 data may be applied and so the Sverdrup streamfunction can not satisfy a no normal flow condition
 1123 through any of the other boundaries. In this case the stress curl $\nabla \times \tau(x, y) = -\partial \tau^x / \partial y$ and independent
 1124 of x and hence the streamfunction is

$$1125 \quad \Psi_{Sv}(x, y) = -\frac{(L-x)}{\rho_o \beta} \frac{\partial \tau^x}{\partial y}. \quad (60)$$

1126 The zonal component of mass transport is then

$$1127 \quad HU = \frac{\partial}{\partial y} \Psi_{Sv}(x, y) = - \frac{(L-x)}{\rho_o \beta} \frac{\partial^2 \tau^x}{\partial y^2}, \quad (61)$$

1128 and the meridional component is Sverdrup transport,

$$1129 \quad HV = - \frac{\partial}{\partial x} \Psi_{Sv}(x, y) = - \frac{1}{\rho_o \beta} \frac{\partial \tau^x}{\partial y}, \quad (62)$$

1130 as expected.

1131 A comparison of the two streamfunction fields (Fig. 19) is one way to see where Sverdrup balance is
 1132 valid in the numerical solution. The steady circulation in this experiment consist of three gyres within
 1133 which the meridional flow has the sign of the wind stress curl, e.g., equatorward in the subtropical gyre
 1134 where $\nabla \times \tau < 0$, and so qualitatively consistent with the Sverdrup relation Eqn. (1). Each of these gyres
 1135 is very strongly compressed onto the western side of the basin in the sense that the largest SSH and thus
 1136 the largest pressure anomaly is found about a hundred kilometers offshore of the western boundary. (see
 1137 Sec. 8.2, 6)

1138 Another and more quantitative way is to evaluate the interior meridional transport for all y , Fig (20).
 1139 The Sverdrup relation gives a fairly accurate account of the meridional transport over the interior of most
 1140 of the subtropical gyre, and to a much lesser degree, the subpolar and tropical gyres. The Sverdrup
 1141 relation is clearly not valid within about 100 km of a western boundary as discussed in Sec. 3.3, nor is it
 1142 valid within roughly 500 - 1000 km of the northern and southern zonal boundary regions. In the zonal
 1143 boundary regions the Sverdrup relation indicates significant meridional flow which does not happen in
 1144 the numerical model solution. What is perhaps surprising is how broad the affected zonal boundary
 1145 regions are (more on this in Sec. 4.3). One consequence of such broad zonal boundary regions is that the
 1146 transport of the western boundary currents of the tropical and the subpolar gyres is somewhat less than is
 1147 the transport of the subtropical gyre, which is not similarly affected by a zonal boundary (Fig. 16).

1148 4.2 Dynamics of the steady circulation: the balance of potential vorticity

1149 The dynamics of the circulation may be described most fruitfully in terms of the balance of potential
 1150 vorticity, Eqn. (34), here expanded and multiplied by H ,

$$1151 \quad \beta VH = \frac{1}{\rho_o} \nabla \times \tau - rh_o \nabla \times \mathbf{V} + HOT, \quad (63)$$

$$1152 \quad \textit{beta} = \textit{curl tau} + \textit{curl drag} + \textit{higher order terms}.$$

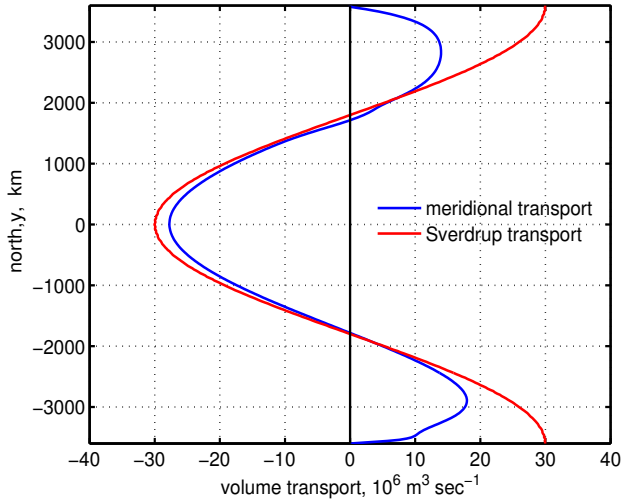


Figure 20: The north-south variation of the zonally-integrated meridional transport computed from the steady model solution (blue line) and computed via the ideal Sverdrup transport relation, Eqn. (1) (red line). The integration extends from the eastern boundary to just outside of the western boundary current. Notice that the actual (numerical) meridional transport vanishes on the zonal boundaries at $y = \pm 3600$ km due to a no normal flow boundary condition. This is something that the Sverdrup relation (red line) can take no account of. The north-south extent of the affected zonal boundary region is 500 - 1000 km, which is a significant part of the tropical and subpolar gyres.

1153 The higher order terms are the collected nonlinear terms involving the advection of potential vorticity and
 1154 the gradient of layer thickness;

$$1155 \quad HOT = -H\mathbf{V} \cdot \nabla \xi + h_o H Q \mathbf{V} \cdot \nabla H - \frac{1}{\rho_o h} \boldsymbol{\tau} \times \nabla H + \frac{r h_o}{H} \mathbf{V} \times \nabla H.$$

1156 In general, the steady potential vorticity balance includes a contribution from all of these terms, including
 1157 the HOT . However, in this solution the nonlinear HOT terms are important only in special places
 1158 (marked with red dots in Fig. 21) where large currents are combined with large horizontal gradients, e.g.,
 1159 the confluence of the subtropical and subpolar western boundary currents near
 1160 $(x, y) = (-L, L/2) = (-3600, 1800)$ km.

1161 4.2.1 Sverdrup interior

1162 Aside from these important but spatially limited regions, the steady potential vorticity balance can be
 1163 characterized by the regional distribution of two term balances or modes among the linear terms of Eqn.
 1164 (63), Fig. (21). One of these, the Sverdrup mode,

$$1165 \quad \beta V H = \frac{\nabla \times \boldsymbol{\tau}}{\rho_o}, \quad (64)$$

$$1166 \quad \textit{beta} = \textit{curltau},$$

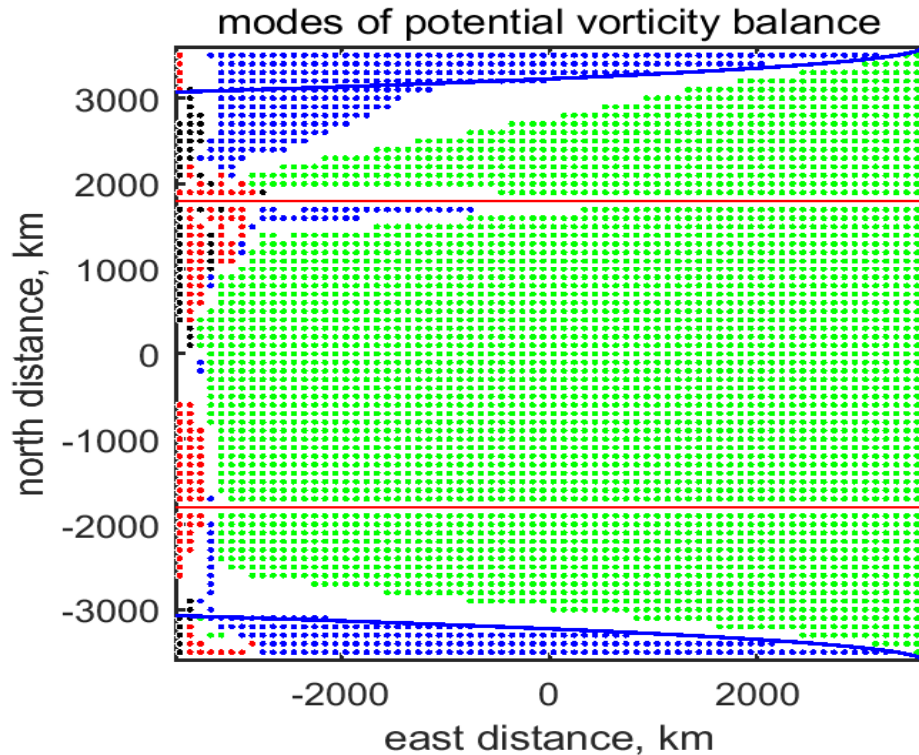


Figure 21: The steady potential vorticity balance characterized by the distribution of the modes (approximate two term balances) of Eqn. (63). Horizontal red lines are the gyre (wind stress curl) boundaries as before. A **green dot** indicates that the Sverdrup mode, $\beta = \text{curl}\tau$, accounts for more than 90% of the variance of the steady potential vorticity balance at that point. This (approximate) Sverdrup balance holds over about 75% of the basin. A **black dot**, shows where $\beta = \text{drag}$ is the dominant mode, mainly near the western boundary. A **blue dot** indicates the mode $0 = \text{curl}\tau + \text{drag}$ found near the northern and southern zonal boundaries. A **red dot** indicates that the *HOT*, the collection of nonlinear terms, was larger than two of the linear terms. If there is **no colored dot**, then there is no dominant mode, and the balance of potential vorticity is shared among at least three of the terms of Eqn. (63). The blue lines near the northern and southern zonal boundaries are a simple, linear estimate of zonal boundary region width that is discussed in Sec. 4.2.3.

1167 accounts for at least 90% of the variance of the potential vorticity balance over most of the interior region
 1168 of the basin (the green dots of Fig. 21), especially within the subtropical gyre, and which is often and
 1169 appropriately called the Sverdrup interior.

1170 Eqn. (34) describes the potential vorticity balance at a fixed point. Consider a site in the subtropical
 1171 gyre interior where the wind stress curl is negative, which by itself would cause Q to decrease with time.
 1172 A steady state will occur if the meridional flow advects higher Q water from the north at the same rate
 1173 (opposite sign) of the stress curl. Since the potential vorticity in the interior is approximated well by the

1174 planetary vorticity, $Q \approx f/h_o$ (with h_o a constant), then this occurs by the advection of planetary vorticity,
 1175 $V\partial f/\partial y$, as if f was a fluid property. For this steady, Sverdrup balance to exist throughout the interior of
 1176 the basin, there must be some mechanism that serves to recharge the higher latitudes (within the
 1177 subtropical gyre) with high Q water, or specifically, with water having $Q \approx f/h_o$. What is the source of
 1178 this high Q water? The western boundary current, described next. (see Sec. 8.2, 7)

1179 4.2.2 Western boundary currents

1180 The Sverdrup balance certainly does not hold within the western boundary currents (Figs. 18 and 19),
 1181 where the meridional current is counter to the Sverdrup flow. The beta effect on a fast-flowing wbc
 1182 current is in any case far larger than can be balanced by the curl of the wind stress (as occurs in the
 1183 Sverdrup interior), and so in this model the steady vorticity balance within a wbc is mainly between the
 1184 beta effect and the curl of the friction, 'drag',

$$1185 \quad \beta VH \quad \approx \quad - \quad rh_o \nabla \times \mathbf{V}, \quad (65)$$

$$1186 \quad \text{beta} \quad \quad \quad \text{drag}.$$

1187 For example, the western boundary current of the subtropical gyre has very large negative relative
 1188 vorticity (Fig. 15), and a correspondingly large, positive, curl of the friction, or 'drag'. This drag largely
 1189 balances the negative vorticity tendency of the beta effect, allowing a steady state within the subtropical
 1190 wbc. Regions where this frictional balance holds in the sense described above are denoted by the black
 1191 dots in Fig. (21), and are very near the western boundary in all three gyres.

1192 To characterize this balance we can define an Ekman number equivalent for the vorticity balance,

$$1193 \quad E_Q = \frac{\text{drag}}{\text{beta}} = \frac{r \nabla \times \mathbf{V}}{\beta V}, \quad (66)$$

1194 ignoring signs and taking $H = h_o$. The usual Ekman number is the ratio of frictional force to Coriolis
 1195 force, but in this case we have curl of the friction divided by (compared to) the beta effect (see Problem
 1196 11, Sec. 7.2). To evaluate E_Q it is helpful to use a streamfunction representation of the velocity and its
 1197 curl. Thus

$$1198 \quad V \approx \frac{\Psi}{L_{wb}},$$

1199 where L_{wb} is the east-west width of the wbc, which for now we will treat as an unknown. Within the
 1200 narrow western boundary current, the horizontal scale in the x direction (normal to the boundary) is much

1201 less than the scale in the y direction and hence the curl of the velocity (the Laplacian of the
1202 streamfunction) is approximately

$$1203 \quad \nabla \times \mathbf{V} = \nabla^2 \Psi \approx \frac{\partial^2 \Psi}{\partial x^2} \approx \frac{\Psi}{L_{wb}^2}.$$

1204 Using these estimates in (66) gives

$$1205 \quad E_Q = \frac{r}{\beta L_{wb}}. \quad (67)$$

1206 If the balance is indeed Eqn. (65), then we can assert $E_Q \approx 1$ and readily solve for the purely
1207 frictional wbc width, $L_{wb} = L_{fric}$ and find

$$1208 \quad L_{fric} = \frac{r}{\beta}. \quad (68)$$

1209 For the present values of r and β , $L_{fric} \approx 50$ km, which is numerically about the same as the (subtropical)
1210 radius of deformation (Sec. 3.3.2). Said a little differently, for the present r , the Q balance of a wbc
1211 having a width equal to the radius of deformation is significantly frictional. Recall (Sec. 2.3) that in this
1212 experiment, the value $r = 1/15$ days, was chosen in an *ad hoc* manner, the minimum r (least viscous)
1213 that permitted a near steady state solution. This is a partial rationalization of this choice. However, there
1214 is no independent means for identifying an appropriate value of r (that I know of), and so we have to be
1215 cautious about interpreting the present model solution as if it were a fully realistic model of a real wbc.

1216 To understand the shallow water model solution, at a minimum we need to know what happens
1217 when r is changed; say that r is doubled to $1/7.5$ days, which makes the solution more viscous. The
1218 pattern of the Sverdrup interior is unaffected, but the amplitude of the Sverdrup transport is reduced
1219 slightly, a few percent. The Sverdrup interior is thus not much affected by the choice of r . The wbc
1220 becomes somewhat thicker, as (68) indicates it should. Since the wbc transport is reduced and the wbc
1221 width increased, the wbc speed is reduced considerably, by about 30%. In that event the flow is steady
1222 throughout the model domain. More interesting is that r is reduced to half the present value, to $r = 1/30$
1223 days. The volume transport in the interior is then a few percent greater and so is a better match to the
1224 ideal Sverdrup transport. But again the overall pattern of the interior circulation is indistinguishable from
1225 the nominal experiment. The width of the subtropical wbc is slightly narrower, though not nearly as
1226 much as the purely frictional boundary layer width (68) suggests, and so it appears that $L_{wb} = R_d$ is a
1227 lower limit that obtains for smallish friction. The wbc current speed is slightly greater, by about 10%, and
1228 so the inertia of the wbc is also greater. The nonlinear terms of the q balance are enhanced, and the
1229 colliding western boundary currents at the subpolar/subtropical gyre confluence (on the western
1230 boundary at about $y = 1800$ km; the largest red dot region of Fig. 21) are considerably more vigorous
1231 than in the nominal experiment (Fig. 37, lower). This kind of unstable, eddying flow is an important and

1232 interesting characteristic of nearly all strong ocean currents that are not constrained by topography.
 1233 However, this aspect of boundary current dynamics is sensitively dependent upon details of the ocean
 1234 bottom topography and the vertical structure of currents, among others, and so is outside the scope of a
 1235 shallow water model and of this essay. (see Sec. 8.2, 9, 11)

1236 4.2.3 Zonal boundary regions

1237 There are extensive regions adjacent to the zonal boundaries (northern and southern boundaries) where
 1238 the ideal Sverdrup balance does not hold, as evident in the qualitative mismatch of Sverdrup transport
 1239 with the actual transport within about 500 to 1000 km of the zonal boundaries (Figs. 19 and 20). As
 1240 noted at the outset, the Sverdrup balance *per se* is unable to satisfy the boundary condition that the
 1241 meridional current must vanish on the zonal boundaries, and so if there is wind stress curl on these
 1242 boundaries (as there is here, Fig. 5) then the Sverdrup balance will necessarily fail; something else must
 1243 happen. Very near the zonal boundaries there is no meridional velocity and thus no β effect. The steady,
 1244 linear potential vorticity balance in this model must reduce to the steady, linear, forced, damped mode,

$$\begin{aligned}
 1245 \quad 0 &= \frac{1}{\rho_o} \nabla \times \tau - r h_o \nabla \times \mathbf{V} & (69) \\
 1246 &= \text{curltau} + \text{drag},
 \end{aligned}$$

1247 indicated by blue dots in Fig. (21).

1248 Like the wbc, this boundary region is also anisotropic, but in this case the meridional, north-south
 1249 scale is much less than the zonal, east-west scale and hence $\nabla^2 \Psi \approx \frac{\partial^2 \Psi}{\partial y^2}$. The balance (69) may then be
 1250 written via the streamfunction as

$$1251 \quad 0 \approx \frac{1}{\rho_o} \nabla \times \tau + r \frac{\partial^2 \Psi}{\partial y^2}.$$

1252 The curl of the drag has to be large enough to balance the wind stress curl in the zonal boundary region,
 1253 and the question is what zonal boundary layer width, L_{zb} , is required to achieve this? Estimating
 1254 $\partial(\)/\partial y \approx 1/L_{zb}$ and $\partial^2(\)/\partial y^2 \approx 1/L_{zb}^2$, then

$$1255 \quad 0 = \frac{1}{\rho_o} \nabla \times \tau - \frac{r \Psi}{L_{zb}^2}.$$

1256 It is not obvious what Ψ should be, but as a first guess, let's try the Sverdrup streamfunction, Eqn. (59),
 1257 even though we know for sure that the Sverdrup Ψ can not be correct right on the boundary. We can be a
 1258 little bit bold with this, since we can check the result against the numerical solution. Given a tentative

1259 estimate $\Psi = (L - x)\nabla \times \tau / \rho_o \beta$, where $L - x$ is the distance from the eastern boundary (positive), the
 1260 boundary layer width is easily found to be

$$1261 \quad L_{zb} = \sqrt{\frac{r(L-x)}{\beta}}. \quad (70)$$

1262 This is sketched onto Fig. (21 as blue lines near the southern and northern zonal boundaries. At the
 1263 midpoint of a zonal boundary, $x = 0$, $L_{zb} \approx 400$ km, which is a reasonable estimate of the half-width of
 1264 the zonal boundary region evident in Figs. (21) and (20). Notice that the region significantly affected by
 1265 the zonal boundary dynamics (the no dot transition region between the blue and green dot regions) is
 1266 about twice this width.

1267 The width of this boundary layer estimate decreases toward the east, which is qualitatively consistent
 1268 with the distribution of modal balances, i.e., a narrower blue region toward the east. An eastward
 1269 decrease of L_{zb} arises because, while the vorticity needed to achieve the balance $0 = \text{curl}\tau + \text{drag}$ on
 1270 the zonal boundary is uniform along the boundary (recall that $\text{curl}\tau$ is here taken to be uniform in x ,
 1271 which is generally not true over the real oceans, Fig. 4) and hence the zonal current, which is qualitatively
 1272 the zonal component implicit in the Sverdrup relation, decreases eastward. As a consequence, the
 1273 north-south horizontal scale over which the current varies must also decrease eastward in order to have
 1274 the necessary relative vorticity and thus curl of the friction sufficient to balance the curl of the wind stress.

1275 Like the western boundary layer, the width of the zonal boundary regions is expected to be
 1276 independent of f and thus should be the same along the southern and northern zonal boundaries since the
 1277 imposed wind stress is the same on those boundaries (Sec. 4.2). However, judging from the east-west
 1278 distribution of q -balance modes found in the numerical model solution (Fig. 21), the zonal boundary
 1279 layer is in fact markedly wider in the western-most third of the sub-polar zonal boundary region. The
 1280 reason for this discrepancy is mainly that the subpolar gyre of this numerical experiment has a
 1281 significantly reduced layer thickness compared to the initial thickness, h is as little as 100 m in the
 1282 western subpolar gyre, and hence there is considerably greater drag than is accounted for by the linear
 1283 equation (69) that presumed $H = h_o = 500$ m. A straightforward experimental test of this hypothesis
 1284 follows from setting the imposed wind stress small enough — $\tau_o = 0.01 \text{ N m}^{-2}$ suffices — that the
 1285 dynamics are linear in the respect that $H \approx h_o$ throughout the model domain. In that case the comparison
 1286 between the numerical and the estimated boundary layer width (70) is quite good throughout. Thus the
 1287 linear estimate of zonal boundary layer width (70) is valid for a linear problem, and it is straightforward
 1288 to understand the sense and the approximate magnitude of the finite amplitude effects that occur when
 1289 there are large spatial variations in layer thickness, as do occur in this numerical solution.

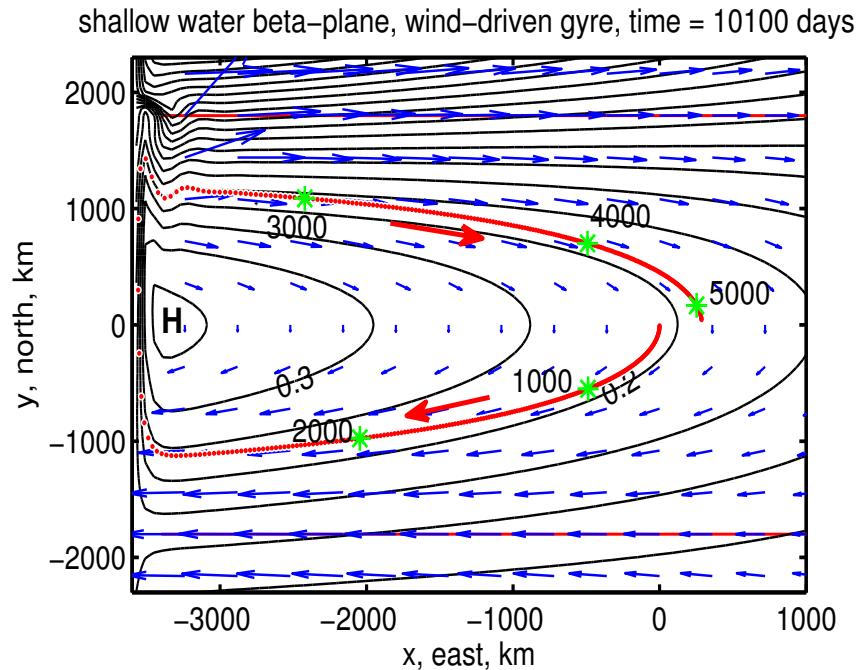


Figure 22: The (almost) steady subtropical gyre, shown by contours of SSH anomaly and a field of velocity vectors. A parcel trajectory that was started at $(x, y) = (0, 0)$ and followed for 5,500 days is the red line. The green asterisks along the trajectory are at 1000 day intervals. The parcel entered the western boundary current at about 2,600 days after starting, and it exited the western boundary current about 200 days later. The parcel returned close to its starting position. Notice that the trajectory is almost parallel to isolines of SSH, but not exactly so.

1290 4.3 A trip around the subtropical gyre

1291 In the previous section, our analysis considered the currents, vorticity, etc., as observed at fixed locations,
 1292 a point of view often dubbed 'Eulerian'. This is the natural starting point, since the shallow water
 1293 equations and their numerical implementation are Eulerian. However, our intuition for classical
 1294 mechanics has roots in a parcel-following, or 'Lagrangian' description, since the m and the a of $F = ma$
 1295 are the mass and acceleration of a specific chunk of material, and not the fluid properties observed at a
 1296 point in space (the Eulerian view). In this section we will take this kind of parcel-following view on a
 1297 complete trip around the gyre. Besides connecting a little better with our intuition for mechanics, this
 1298 also gives a holistic view of the circulation in that it shows how the western boundary current is an
 1299 essential component of a steady circulation.

1300 To construct a Lagrangian description we have to solve for parcel trajectories,

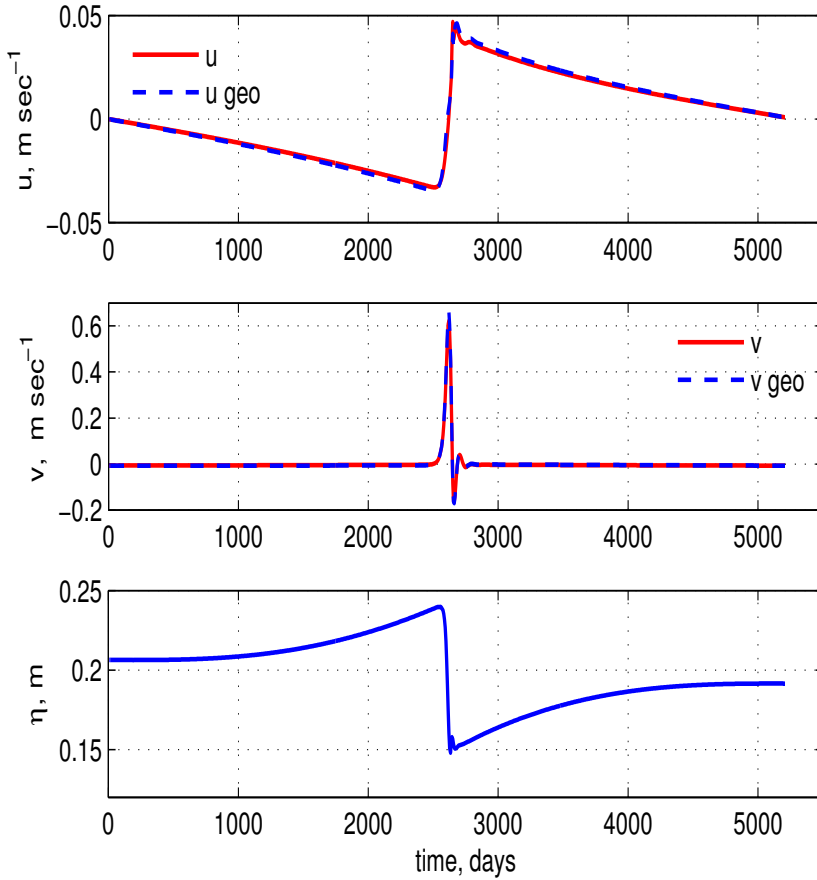


Figure 23: Velocity components along the trajectory of Fig. (22). **(upper)** East velocity (red line) and the geostrophic velocity estimated from the layer thickness (dashed blue line). **(middle)** North component of velocity. Note the very large change in the scale compared to the east component above. The actual velocity and the geostrophic velocity are close enough that the lines are difficult to distinguish. **(lower)** The SSH anomaly along the trajectory. While within the interior region, the parcel slowly climbs the SSH high of the subtropical gyre. While in the wbc, it descends comparatively very rapidly.

1301 $X(t; (X_o, Y_o)), Y(t; (X_o, Y_o))$ by integrating the velocity along the path of a specific parcel,

$$1302 \quad X(t) = \int_0^t U(x, y) dt + X_o, \quad \text{and,} \quad Y(t) = \int_0^t V(x, y) dt + Y_o, \quad (71)$$

1303 where (X_o, Y_o) is the initial position and the $t = 0$ here is the time this integration starts (not the starting
 1304 time of the numerical integration as in Sec. 3). The key thing is that the (x, y) dependence of the velocity
 1305 field is continually updated as the integration proceeds, i.e., the (x, y) in the integrand is set $= (X, Y)$
 1306 at each time step. Since the velocity field is available only at the 20 km resolution of the numerical model,
 1307 the evaluation of velocity at an arbitrary parcel position requires an interpolation of the discrete model
 1308 data, which is bound to incur some error, much like the finite difference evaluation of a derivative.

1309 The initial position may be chosen anywhere in the model domain; the trajectory shown in red in Fig.
 1310 (22) was started in the center, $(X_o, Y_o) = (0, 0)$. The initial position is, in effect, the tag on the parcel
 1311 that happened to be there at the time t_o . Not surprisingly, different initial positions result in different

1312 trajectories. In this circulation, small initial position differences yield only rather small trajectory
1313 differences (some examples to follow). A flow having this property may be described as 'laminar'.¹⁵

1314 A complete trip around the subtropical gyre from this starting position $(X_o, Y_o) = (0, 0)$ requires a
1315 little more than 5000 days and extends over about 11,000 km. If the circulation was exactly steady (it
1316 isn't quite), and if the integration method used to construct the trajectory was without error (it can not be),
1317 then the parcel would return to its starting point. Notice that this parcel didn't quite make it (Fig. 22).
1318 However, the interesting changes in parcel properties along the track are considerably larger than the
1319 starting point/ending point mismatch, and so the semi-quantitative inferences that we can make from this
1320 trajectory are reliable.

1321 Assuming that the fluid is not at rest, then there is no Lagrangian steady state comparable to the
1322 steady state of an Eulerian frame. Rather, fluid parcels continuously change position and generally all
1323 other properties with time. To find say the potential vorticity of the parcel, we can either evaluate the
1324 (presumably known) $q(x, y)$ field at the parcel position, or, integrate the q conservation equation along the
1325 trajectory.

1326 4.3.1 Momentum balance and energy exchanges

1327 The relationship of parcel motion to the local slope of the SSH anomaly (the pressure or geopotential
1328 anomaly) is closely analogous to the motion of a dense parcel on a slope studied in Part 1. Differences in
1329 detail include that the slope changes quite a lot along the trajectory, especially near the western boundary,
1330 and, there is an additional external force, the wind stress, which is essential for compensating the slow
1331 but inexorable effects of friction.

1332 During the first several hundred days, the parcel moved very slowly toward the south, which is
1333 consistent with the meridional Sverdrup flow at the starting latitude. Eventually, the parcel turned toward
1334 the southwest (Fig. 23) and began to pick up some speed. The trajectory was roughly parallel to the SSH
1335 lines with higher SSH to the right. Thus the parcel motion was, to a first approximation, geostrophic.

1336 An important departure from strict geostrophy is that the parcel had a rather small but systematic
1337 component of motion across the SSH lines. While the parcel was in the interior, it slowly climbed up the

¹⁵If instead the sensitivity to initial position was large, then the flow would be characterized as chaotic or turbulent. Most large scale fluid flows, and including the real ocean circulation, are turbulent in this sense.

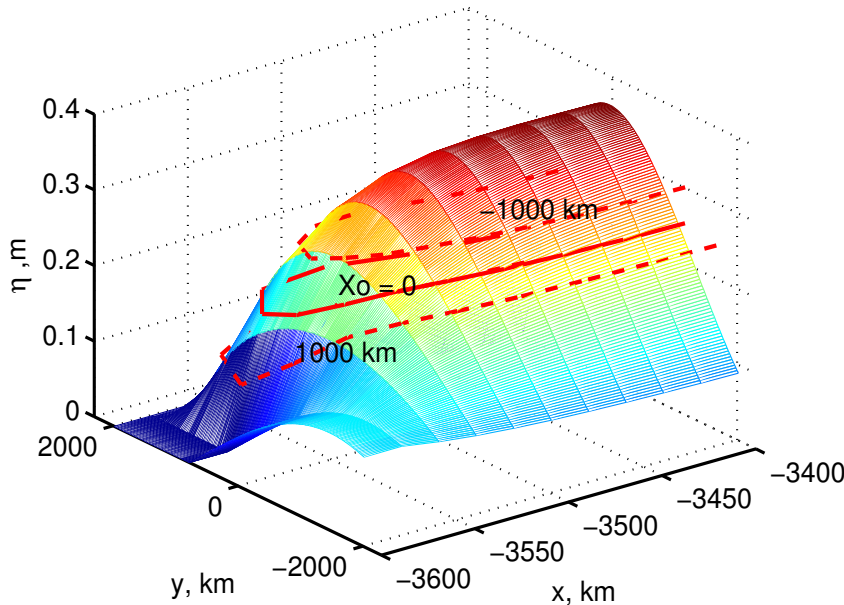


Figure 24: Three trajectories superimposed on the SSH anomaly, η , of the western side of the subtropical gyre. The trajectories differ in their starting points, X_o , that is noted. The solid red trajectory has $X_o = 0$ and is shown also in Fig. (22). Notice that the x scale is greatly expanded compared to the y scale so that the very large zonal slope of SSH within the wbc and its relationship to these trajectories is apparent.

1338 SSH high of the subtropical gyre. The damping effect of friction causes the parcel to descend the local
 1339 SSH slope, though at a very small angle consistent with the small Ekman number, E is $O(0.01)$. We can
 1340 therefore infer that the small component of motion toward higher SSH is a consequence of the wind
 1341 stress. From an energy perspective, the positive wind work that occurred while the parcel was in the
 1342 interior was stored as potential energy.

1343 After several thousand days, the parcel began to approach the western boundary, where the SSH
 1344 topography was by comparison, very steep, about two orders of magnitude greater than in the interior. As
 1345 the parcel neared the western boundary it accelerated to the north, reaching speeds of $O(1 \text{ m sec}^{-1})$, or
 1346 about two orders of magnitude greater than the speeds that characterize the slow, Sverdrup flow of the
 1347 interior. The parcel motion never showed any significant inertial motion, and the momentum balance
 1348 remained almost geostrophic (Fig. 23, middle). This implies that the acceleration associated with the
 1349 steep wbc topography was slowly-varying compared to the rotation time, $1/f$. The kinetic energy
 1350 associated with the rapid northward flow came from the potential energy that was released as the parcel
 1351 descended about 0.1 m while within the western boundary current (Fig. 23, lower). There was also some
 1352 energy loss to friction. After about 200 days, the parcel left the western boundary current and entered the
 1353 slow eastward flow along the north side of the subtropical gyre. While moving eastward, it slowly
 1354 climbed back up the high SSH of the subtropical gyre and returned close to its starting value of SSH
 1355 anomaly.

1356 4.3.2 Potential vorticity balance

1357 Potential vorticity conservation provides another way to think of the Sverdrup relation. Given that the
 1358 field of q is presumed to be steady at fixed locations, $\partial q/\partial t = 0$, then the q of the moving parcel is just
 1359 the q at it's present position (this sounds both profound and trivial at the same, but be sure to understand
 1360 this before going on) . Moreover, the spatial variation of Q is due mainly to the spatial variation of f , at
 1361 least in the subtropical gyre interior, where the circulation is very slow. The parcel was subject to the
 1362 overlying wind stress, whose curl was negative, and thus would tend to reduce the q of the parcel (Fig.
 1363 25, upper). Since the q of the parcel had to be consistent with the q of the presumed steady field, the
 1364 parcel must move southward toward lower q , assuming that the q field is dominated by the meridional
 1365 variation of f . Said a little differently, the southward motion of the parcel must be just sufficient to keep
 1366 the q of the parcel consistent with the steady field of potential vorticity, $(\nabla \times v + f)/h$. In the subtropical
 1367 gyre, the spatial variation of q is due mainly to the latitudinal variation of f , and hence we are led to the
 1368 Sverdrup relation. This is a rigorous argument for the Sverdrup relation, given the assumptions of a
 1369 steady, linear q balance. However, it feels awfully thin as an explanation for existence of the circulation
 1370 in the first place. And of course, so does the usual (Eulerian) Sverdrup relation.

1371 It is a fair surmise that a parcel can not be subject solely to a negative wind stress curl, or else the
 1372 basin-wide average of q would surely decrease with time, which is not consistent with the steady state of
 1373 the Eulerian circulation. It must be the case that parcels occasionally experience a process that increases
 1374 q — a (relatively) quick pass through the western boundary current where there is a very strong, positive
 1375 curl of the drag. This positive drag curl resets the parcel's q to a value that is consistent with the interior q
 1376 (Fig. 25) where it reenters the Sverdrup interior. Thus the western boundary current is a crucial part of
 1377 the gyre-scale circulation with respect to potential vorticity.

1378 4.3.3 Depth dependence*

1379 The shallow water form of the Sverdrup relation implies that the wind stress acts upon the entire layer of
 1380 thickness h that participates in the Sverdrup transport. That is indeed exactly what happens in a shallow
 1381 water model, but not within the real ocean. Instead, the Sverdrup transport occurs within an Ekman layer
 1382 of thickness d_{Ek} that is typically $O(100\text{ m})$ that absorbs all of the direct wind stress, i.e., $\tau(z < -d_{Ek}) = 0$,
 1383 and a geostrophic layer that is much thicker, $O(1000\text{ m})$. If the wind stress penetrates no deeper than 100
 1384 m, say, then how is the much thicker geostrophic layer affected by the wind? The answer is vortex
 1385 stretching contained within the z -dependent vorticity equation, (20), but not in the integrated Sverdrup
 1386 relation. Just to be specific, consider the subtropical gyre where the wind stress curl is negative, and so

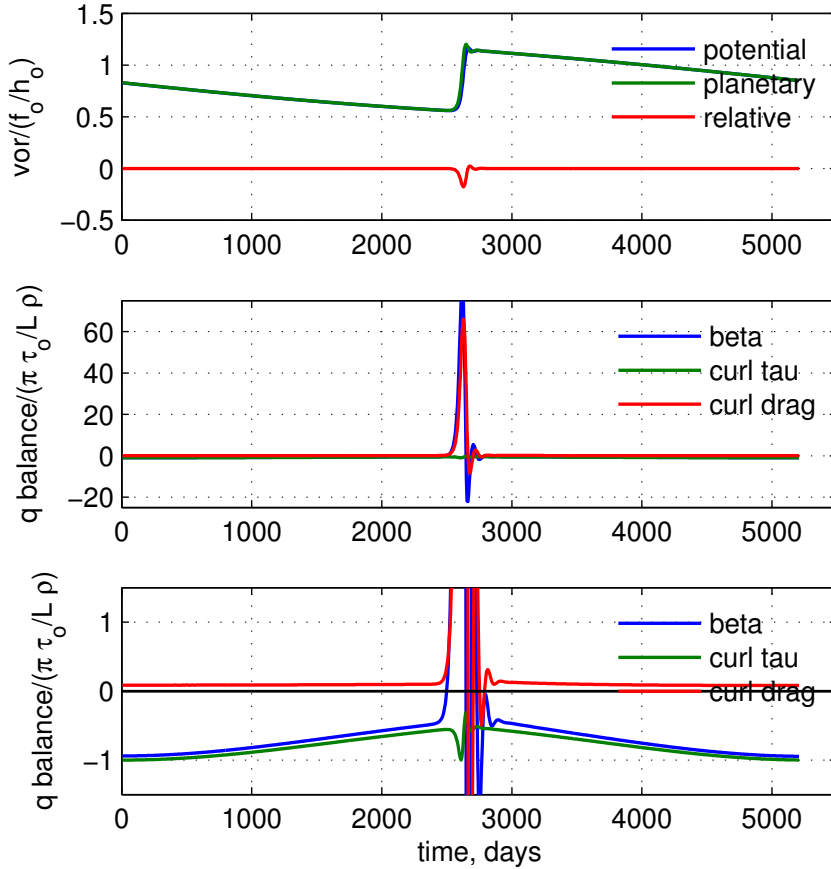


Figure 25: Potential vorticity along the trajectory of Fig. (22). **(upper)** The full potential vorticity (blue line), the planetary vorticity (green line) and the relative vorticity (red line). These are normalized by f_o/h_o . Notice that the relative vorticity is very small except when the parcel is within the western boundary current where it has a maximum magnitude of $-1/4$ (normalized). **(middle)** Leading terms in the potential vorticity balance, Eqn. (63). These data are normalized by a nominal wind stress curl, $8 \times 10^{-8} \text{ m sec}^{-2}$. When plotted at this scale, about all that can be told is that the beta term is approximately balanced by the drag curl term while the parcel is within the western boundary current. **(lower)** Same data as above, but with a clipped ordinate that reveals the interior balance between the beta term and wind stress curl.

1387 that the Ekman layer transport is convergent. The vertical velocity at the base of the Ekman layer due to
 1388 wind stress curl alone is just $\frac{1}{f} \nabla \times \tau$ and the beta effect acting upon the meridional component of Ekman
 1389 transport contributes another $\frac{\beta}{f} \tau^x$. The net vertical velocity is then

1390
$$W(-d_{Ek}) = \frac{1}{\rho_o} \nabla \times \left(\frac{\tau}{f} \right).$$

1391 Only the stress at the sea surface appears here, and letting $d_{Ek} \rightarrow 0$ does not alter the Ekman transport or
 1392 its divergence. Thus, while it is unphysical, it is not incorrect to imagine that this vertical velocity is
 1393 present at the sea surface (though in practice it is largest at the base of the Ekman layer). This
 1394 Ekman-induced vortex stretching is expected to accompany a meridional, geostrophic transport,

1395
$$\beta \int_{-d}^0 V_{geo} dz = f W(-d_{Ek}) = \frac{f}{\rho_o} \nabla \times \left(\frac{\tau}{f} \right), \quad (72)$$

1396 which is the same as Eqn. (24).

1397 There is an important distinction between the shallow water version of Sverdrup transport and the
 1398 vortex stretching induced transport described above insofar as in the former, all of the water in the
 1399 Sverdrup layer follows a forced q balance, $dq/dt = \nabla \times \tau / \rho_o$. In that event, all of the water that
 1400 participates in the Sverdrup transport must go through the western boundary current in order to reset q
 1401 (this is a Lagrangian description so we use q vs. Q). In the vortex-stretching case, the water that makes
 1402 up the geostrophic Sverdrup transport follows the linearized q conservation, i.e., $dq/dt = 0$, or in the
 1403 z -dependent case, $\beta v = f \partial w / \partial z$. In that event, the water that circulates within the gyre need not go
 1404 through the western boundary current to reset q to larger values, since q is not changed by the wind stress.
 1405 The real ocean is somewhere between these two extremes: some fraction of the water that participates in
 1406 the Sverdrup transport is directly wind-forced, but not all, or even most.¹⁶

1407 4.4 Another way to view the Sverdrup relation

1408 The Sverdrup relation implies or requires a steady state not only of potential vorticity but also of
 1409 momentum, energy, and of the stratification (layer thickness). Consideration of this latter yields what I
 1410 believe is the most insightful view of the Sverdrup relation.

1411 The east-west tilt of SSH over the subtropical gyre interior implies a meridional geostrophic current
 1412 that is equatorward and that is divergent (thinning) on account of the beta effect (Sec. 1.3),

$$1413 \quad \frac{\partial h_{geo}}{\partial t} = \frac{\beta h}{f} V_{geo} < 0.$$

1414 Thus a meridional geostrophic current on a beta plane can not, by itself, be steady. Something more must
 1415 be present, and of course we know that that could be a wind stress and an associated, convergent Ekman
 1416 transport,

$$1417 \quad \frac{\partial h_{Ek}}{\partial t} = - \left(\frac{\partial h_{U_{Ek}}}{\partial x} + \frac{\partial h_{V_{Ek}}}{\partial y} \right) = \nabla \times \left(\frac{\tau_o}{\rho_o f(y)} \right) > 0.$$

1418 Assuming that the current is the sum of geostrophic and Ekman currents only, then

$$1419 \quad \frac{\partial h}{\partial t} = \frac{\partial h_{geo}}{\partial t} + \frac{\partial h_{Ek}}{\partial t}$$

¹⁶To follow up on this requires a depth-dependent model and some means to specify the depth of the Ekman layer, d_{Ek} . These are outside the present scope, but note that a landmark advance on the theory of wind-driven circulation was developed along this line by Jim Luyten, Joe Pedlosky and Hank Stommel, 'The ventilated thermocline', J. Phys. Oceanogr., Feb. 1983, [https://doi.org/10.1175/1520-0485\(1983\)013;0292:TVT;2.0.CO;2](https://doi.org/10.1175/1520-0485(1983)013;0292:TVT;2.0.CO;2).

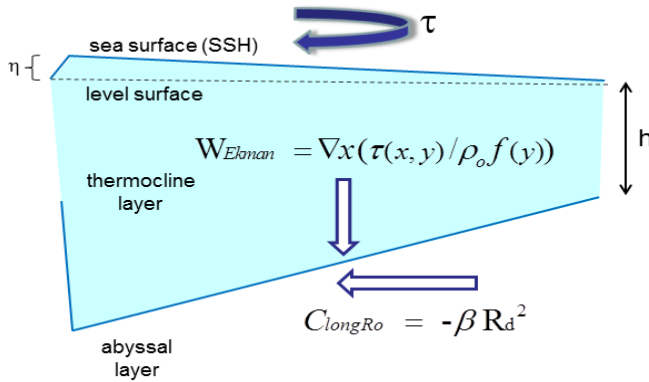


Figure 26: A schematic cross section of the North Atlantic subtropical thermocline, sliced east-west and viewed looking toward the north as in Fig. (1). The wind stress over the subtropical gyre produces an Ekman transport that is convergent and that would tend to thicken the thermocline layer. The Sverdrup relation may be viewed as a steady balance between this positive thickness tendency and the negative thickness tendency associated with the beta effect acting upon the equatorward geostrophic flow.

1420 and a little rearranging gives

$$1421 \quad \frac{\partial h}{\partial t} = \frac{\beta h}{f} (V_{geo} + V_{Ek}) - \frac{1}{\rho_o f} \nabla \times \tau.$$

1422 This is the wind-forced version of the first order wave equation (13) that contains both the Rossby wave
 1423 propagation mechanism, a balance of the left side and the first term on the right side, and the Sverdrup
 1424 relation, if the layer thickness is steady.

1425 The large scale thickness field of the subtropical gyre interior may thus be viewed as an arrested,
 1426 long Rossby wave. The westward translation expected from the β -effect and the first order wave equation
 1427 is balanced by a wind stress-induced convergence of the Ekman transport. Wind-driven gyres and
 1428 mesoscale eddies are closely related in as much as they have the same β -effect acting upon meridional
 1429 flows (this seems obviously true), the difference is that wind stress does not vary appreciably on the
 1430 horizontal scale of a mesoscale eddy and hence the westward propagation.

1431 5 Experiments with other wind fields and basin configurations

1432 The idealized, steady, zonal wind field considered up to here is, of course, just one possibility. In this
 1433 section we will consider briefly some other, equally idealized wind fields and basin configurations that
 1434 help reveal several important aspects of the wind-driven circulation.

1435 5.1 Annually-varying winds and circulation

1436 The model experiments of Sections 3, 4 and 5 assumed that the wind field was steady, once switched on.
 1437 That is a reasonable starting point for a study of the wind-driven circulation. However, almost everyone
 1438 with experience living in a coastal region will attest that the wind over the ocean varies with the seasons,
 1439 and in some regions it varies quite a lot. For example, the annual variation of the westerlies over the
 1440 northern North Atlantic is very roughly $\pm 50\%$ of the annual mean, with the highest winds during winter.
 1441 The annual variation of easterly wind magnitude is somewhat less, though the annual migration of the
 1442 Inter-Tropical Convergence Zone (furthest north in summer) produces a large annual variation in the
 1443 local wind stress curl.^{3,11} Meridional winds (not included in this study) show an especially marked
 1444 annual variation that also contributes significantly to the annual variation of stress curl. Given this large
 1445 amplitude annual variation, and the day-to-day variation of winds with weather, one might argue that the
 1446 time-mean wind scarcely exists, outside of our climatologies. This raises an obvious question — what
 1447 have we missed by considering only the long-term average winds?

1448 Given what we have learned about the response time of the western boundary current, we might
 1449 guess that an annually varying wind will not have a large effect on at least the western boundary current
 1450 of the subtropical gyre. But to find out more, let's calculate the solution for an idealized,
 1451 annually-varying wind stress,

$$1452 \quad \tau^x(x, y, t) = (0.1 + 0.05 \sin(2\pi t/365)) \sin(\pi y/L),$$

1453 where t is the time in days. Note that this wind stress amplitude varies quite a lot, between 0.05 and 0.15
 1454 Pa. This annually-varying wind was applied from the start of an integration that was continued past
 1455 10,000 days. The solution never comes to a steady state, but the annual cycle in the ocean circulation
 1456 becomes stationary in the sense that it repeats from one year to the next and so the startup transient has
 1457 been minimized by 10,000 days.

1458 Snapshots of the resulting circulation at times that are near the minimum and maximum response in
 1459 the tropical gyre are in Fig. (27), and a series of slices through the center of the gyres shows the (inferred)
 1460 η (Fig. 28). The $\eta(x)$ from the steady wind experiment (red dashed line) runs through the center of the
 1461 envelope of the time-varying $\eta(x, t)$, indicating that the dynamics are effectively linear, i.e., the
 1462 time-mean of the solution computed with an oscillating wind stress is very nearly the same as the
 1463 solution computed with the time-mean of the wind stress. The first result of this experiment is that if the
 1464 steady or long time-mean of the ocean circulation was the only thing of interest, then we would not have
 1465 to be concerned with resolving explicitly the annual variation of the wind; the long term (yearly or more)
 1466 time-mean of the wind stress would evidently suffice, at least for this model.

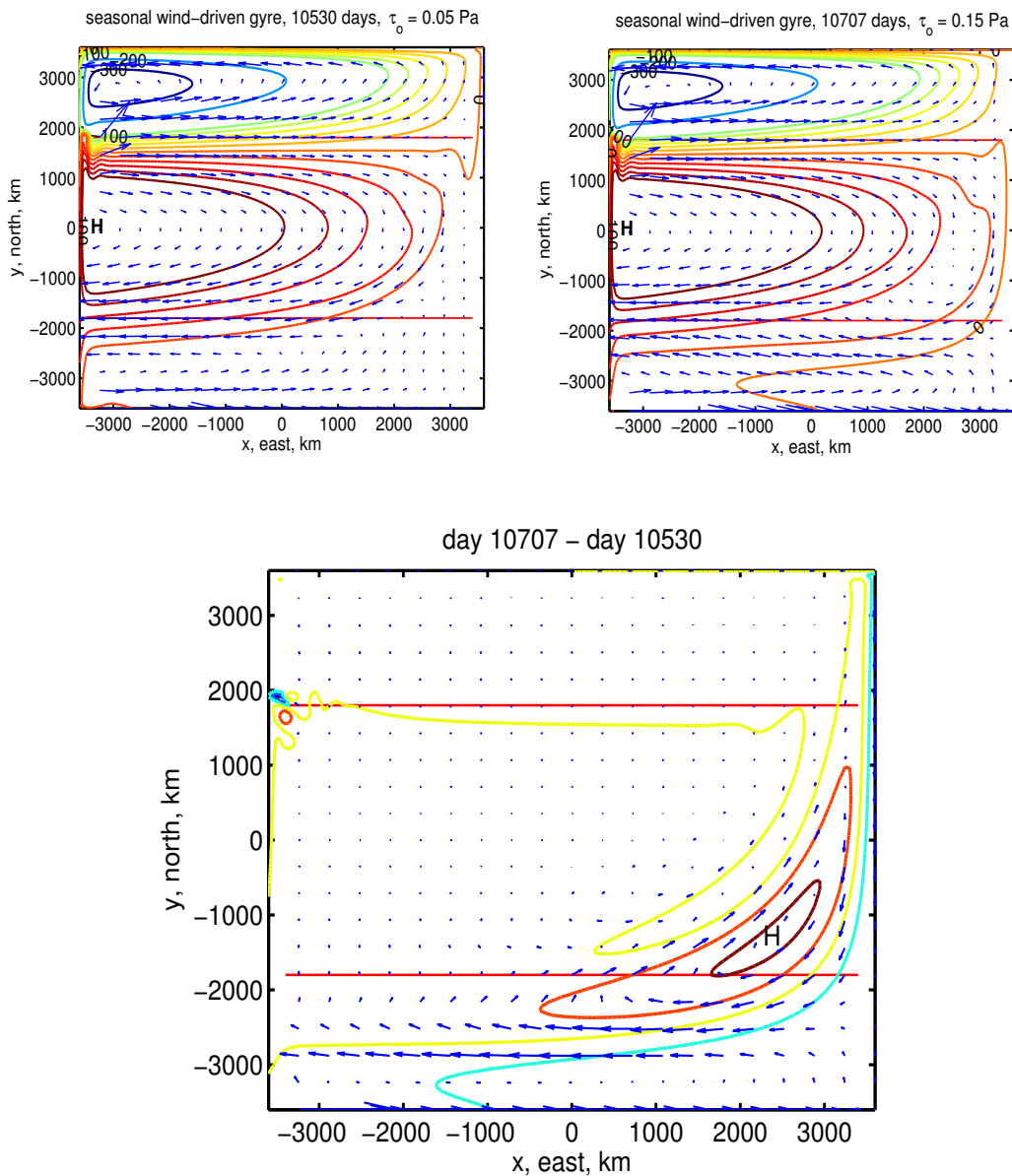


Figure 27: **(upper)** Two snapshots of the circulation taken 180 days apart and near a minimum (left) and maximum (right) of the tropical circulation. The latter occurs about one month after the maximum of the annually-varying wind stress amplitude. An animation of these data is available from www.whoi.edu/jpweb/seasonal-gyres.mp4 **(lower)** The difference of the two snapshots, showing the pattern of the annual cycle. Notice the small, intense eddies near the western boundary at about $y = 1800$ km, the confluence of the subpolar and subtropical western boundary currents. This kind of time-dependent eddy variability is present even with a steady wind stress.

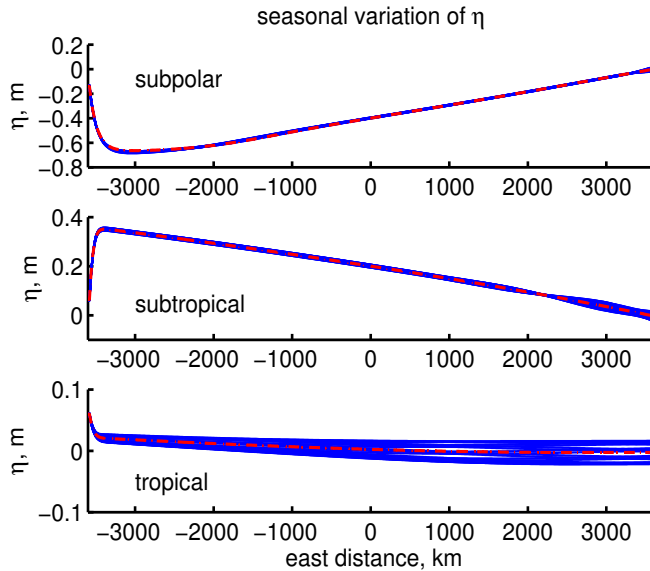


Figure 28: Zonal profiles of SSH, $\eta(x)$, from the annually-varying winds experiment. These profiles were taken through the centers of the three gyres noted. The blue lines were taken at 40 day intervals after time = 10,000 days when the solution appeared to be in a statistically steady state. The single red dashed line is a slice through the base case solution having steady winds, and notice that it goes through the center of the envelope of blue lines. Notice too that the η scale differs considerably between the three panels, consistent with the considerably larger η in the subpolar gyre.

1467 A second important result of this experiment is that the amplitude of the annual variation in the
 1468 ocean varies greatly with latitude. Specifically, the tropical gyre responds much more vigorously to the
 1469 annually-changing wind than does either the subtropical or especially the subpolar gyre. This is what we
 1470 should have expected from the start up experiment, which showed a much faster rise of the tropical gyre
 1471 vs. the subpolar gyre. The amplitude of the annual variation in the ocean depends very much upon the
 1472 variable of interest. For example, the zonal current sampled on the north side of the middle of the tropical
 1473 gyre (Fig. 29, solid red line) varies by $\pm 50\%$ in this experiment, or the same as the wind stress. The
 1474 explanation for this vigorous low-latitude response appears to be as simple and direct as the $\propto 1/f^2$
 1475 dependence of the local, wind-induced (Stage 2) geostrophic current, Eqn. (48). The observed annual
 1476 variation of zonal currents in the tropics is likely of this sort.³ There is also an annual period eastern
 1477 boundary wave that has an appreciable amplitude in the lower subtropics. This wave penetrates only
 1478 about one wavelength into the interior.

1479 Wbc transport is one measure of the gyre circulation (Rossby et al., 2010, footnote 2): in the
 1480 subpolar gyre, the wbc transport varies by about ± 0.3 Sv, in the subtropical gyre by about ± 0.7 Sv, and
 1481 in the tropical gyre, by about ± 1.2 Sv or only about $\pm 8\%$ (Fig. 30). The latter is much less than the
 1482 response of zonal current just noted. The western boundary current transport is a bulk property of a gyre,
 1483 and responds on the time scale of the basin-wide meridional (Sverdrup) flow, $2L/C_{longRo}$, Eqn. (51). The
 1484 long Rossby wave speed is $\propto 1/f^2$ and much faster within the tropical gyre, but nevertheless, the rise
 1485 time of the wbc transport of the tropical gyre is many hundreds of days (Fig. 16) and fairly long
 1486 compared to the time scale of the annually-varying wind, a few months. The response time of the
 1487 subtropical and subpolar gyres is much longer still, a thousand to many thousands of days, and hence the

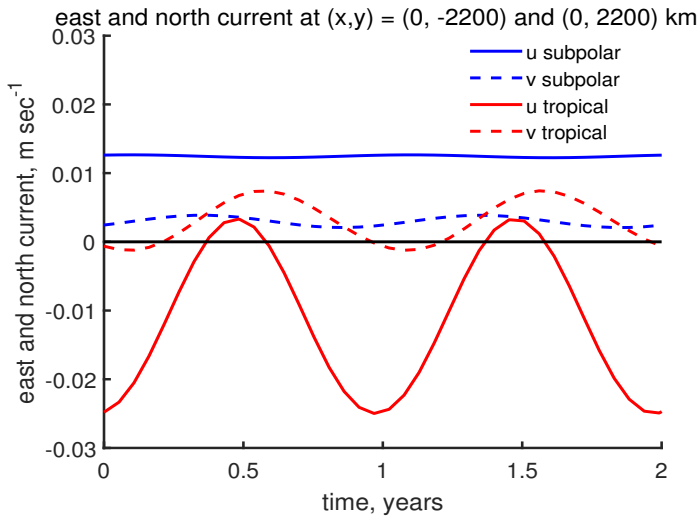


Figure 29: East and north component of the current from the annually-varying wind experiment. The current was sampled at two sites, on the south side of the subpolar gyre (blue lines) and the north side of the tropical gyre (red lines). The current at the high latitude site is almost constant in time despite the annually-varying wind stress. The current at the low latitude site oscillates by about $\pm 50\%$ around a mean which is very close to the steady state current found in the steady wind stress experiment of Sec. 3.

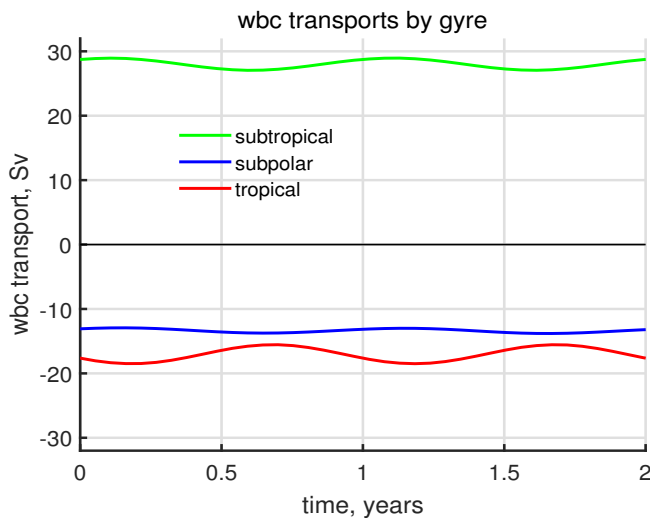


Figure 30: Transports of the western boundary current in each of the gyres from the annually-varying wind experiment. Colors are as in Fig. (16). Notice that the annual variation of the wbc transport in the tropical gyre (red line) is modest when compared to the very large annual variation of especially the zonal current in the interior of that gyre, cf. the red, solid line of Fig. (29).

1488 wbc transport of higher latitude gyres varies even less in response to annually-varying wind.

1489 5.2 A stress field with no curl*

1490 The discussion of wind stress has emphasized importance of the curl of the wind stress curl, rather than
 1491 the stress itself. And yet, the Ekman transport depends only upon the stress, and the Stage 2 response

1492 includes a term proportional to the β -induced divergence of the Ekman transport, and thus the stress.
 1493 This raises the question, can there be a steady circulation driven by wind stress alone, that is, by a stress
 1494 field with no curl?

1495 To find out we can conduct an experiment in which a spatially uniform stress is imposed over the
 1496 ocean basin. To avoid troublesome instances of vanishing layer thickness near boundaries, the stress is
 1497 made very small, 0.01 N m^{-2} . The amplitude of the resulting currents and layer thickness are also very
 1498 small, but our interest will be the structure of the response, rather than it's amplitude.

1499 If the spatially uniform stress is eastward, say, then the Ekman transport is southward throughout the
 1500 basin, and divergent, Eqn. (45). For short times, $t \leq 1000$ days, this produces a thinning of the active
 1501 layer (low pressure) that is most pronounced at lower latitudes, while also causing a pileup of water near
 1502 the equatorial boundary where there is a growing high pressure. The resulting zonal current near the
 1503 equatorial boundary is thus eastward, and there is a weaker, more distributed westward flow at higher
 1504 latitudes, evident at $y > -2000$ km in Fig. (31) (upper and middle).

1505 Just as we have seen before, these zonal currents are necessarily turned into the meridional direction
 1506 along the eastern boundary, and the result is to initiate a long Rossby wave-like front that propagates
 1507 westward across the basin. This eastern boundary Rossby wave signals the adjustment toward a steady
 1508 state, and not too long after the Rossby wave passage the stratification (layer thickness) and flow are
 1509 indeed quasi-steady. The steady state sea surface (inferred from the layer thickness) slopes up toward the
 1510 east so that a zonal pressure gradient opposes the wind stress. Most notably, the current in the adjusted
 1511 steady state vanishes. Absent a curl of the wind stress, there is a vanishing meridional flow in the interior,
 1512 which comes as no surprise if we have already accepted the Sverdrup relation. Since this applies within a
 1513 closed basin, neither can there be a steady zonal flow. (see Sec. 8.2, 12)

1514 **5.3 Meridional winds over a basin without sidewalls (a channel)***

1515 One last experiment: consider a basin with dimensions as before, but now replace the no normal flow
 1516 boundary condition on the eastern and western boundaries with a reentrant boundary condition, i.e., for
 1517 the zonal velocity,

$$1518 \quad u(x = -L) = u(x = L),$$

1519 as if the basin was a channel that wrapped all the way around a cylinder. Similar boundary conditions are
 1520 applied to h and v . We have had occasion to think about a zonal wind stress acting on a channel of this

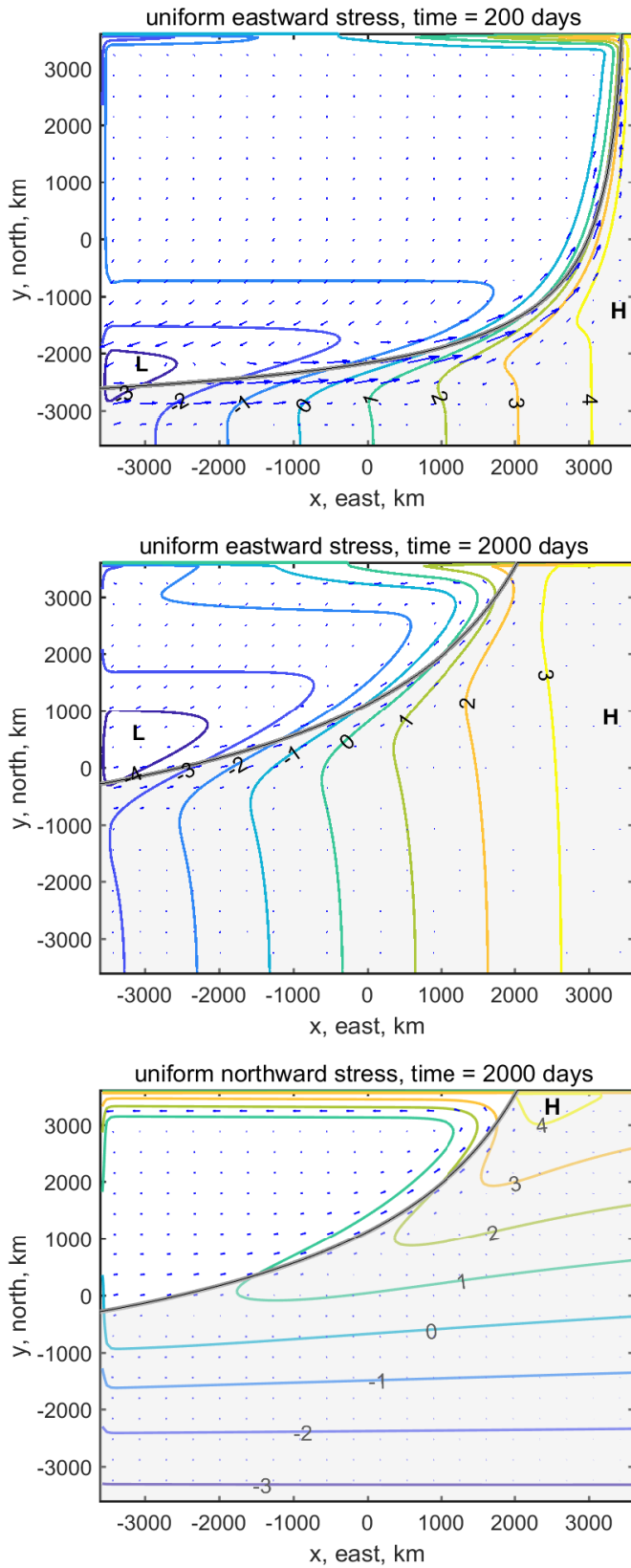


Figure 31: **(upper)** and **(middle)** Two snapshots from a wind-driven experiment in which the wind stress was spatially uniform and eastward at a very small value, 0.01 N m^{-2} . The times were 200 and 2000 days after the stress was switched on. The contours are of the anomaly of layer thickness, in meters. The blue arrows are the current, though with the comparatively very large currents within boundary currents omitted. The gray shading extends westward from the eastern boundary at the y-dependent speed of a long Rossby wave. **(lower)** A snapshot at 2000 days from an experiment in which the wind stress was spatially uniform and northward.

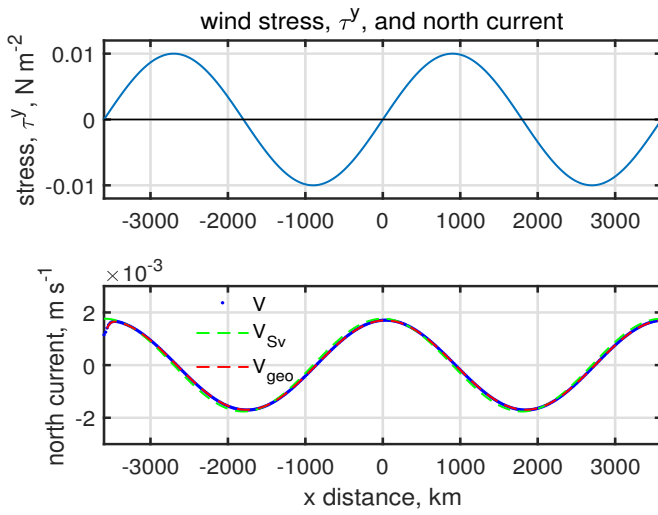


Figure 32: **(upper)** The x profile of the northward wind stress field applied in the channel experiment. The stress was independent of y . **(lower)** The north component of current across $y = 0$ at time = 10,000 days (blue dotted line) along with the expected Sverdrup current (green dashed line) and the meridional, geostrophic current estimated from the thickness field (red dashed line). These are almost identical, and hence the steady meridional flow in this experiment is both geostrophic and Sverdrup, there being no meridional Ekman flow.

1521 sort (Sec. 3.3) and so for this experiment the wind stress is presumed to be in the *meridional* direction.
 1522 To be consistent with the channel configuration and the reentrant boundary conditions,

$$1523 \quad \tau^y(x) = \tau_0 \sin(2\pi x/L), \quad (73)$$

1524 (Fig. 32, upper) so that $\tau^y(-L) = \tau^y(L)$ and independent of y . The stress amplitude is made very small,
 1525 $\tau_0 = 0.01 \text{ N m}^{-2}$, to avoid vanishing layer thickness in boundary currents. Meridional winds certainly do
 1526 occur over the oceans, especially near boundaries, but a basin-wide, meridional wind stress field of this
 1527 sort is not realistic of any wind stress field observed in nature. Regardless, it does help to make an
 1528 important point regarding the role of an eastern boundary vis-à-vis the Sverdrup relation. Given the
 1529 boundary condition (73) the zonal length scale of the stress field will be written

$$1530 \quad L_\tau^x = 2\pi/L,$$

1531 to distinguish from the distance to the eastern boundary that plays such a prominent role in the closed
 1532 basin cases considered to now.

1533 The Ekman transport that accompanies this meridional wind stress is zonal, and is divergent. The
 1534 resulting Stage 2 thickness anomaly grows linearly with time as

$$1535 \quad h_{S2} = \frac{\tau_0}{\rho_o f L_\tau^x} \cos(2\pi x/L) t,$$

1536 and forms alternate highs and lows, Fig. (33). The Stage 2 meridional geostrophic current is

$$1537 \quad v_{S2} = \frac{\tau_0 g'}{\rho_o f^2 L_\tau^{x2}} \sin(2\pi x/L) t$$

1538 where f is $f(y)$, and so v_{S2} is much bigger at lower latitudes (smaller y) as we have seen before. Like the
 1539 Stage 2 response of the closed basin cases, this steadily accelerating current persists for only a finite time,
 1540 hundreds or thousands of days depending upon y , after which it is supplanted by a steady or nearly steady
 1541 Sverdrup balance,

$$1542 \quad v_{Sv} = \frac{\tau_o}{\rho_o L_\tau^x \beta H} \cos(2\pi x/L).$$

1543 In this experiment, where there is no eastern boundary, the near-steady Sverdrup balance develops
 1544 first at low latitude, and then spreads northward. At a given y , the adjustment occurs in the time required
 1545 for a long Rossby wave to propagate westward over the distance L_τ^x , the length scale of the wind stress.
 1546 The northward extent of the adjusted region is then estimated by

$$1547 \quad L_\tau^x = \frac{\beta C^2}{f^2} t, \quad (74)$$

1548 where f is $f(y)$. Using the beta-plane representation of $f(y)$ and solving for the northward extent of the
 1549 adjusted region, Y , gives

$$1550 \quad Y = \sqrt{\frac{C^2}{\beta L_\tau^x}} t^{1/2}, \quad (75)$$

1551 which is used to define the gray shading of Fig. (33). This makes a plausible estimate of the y that
 1552 separates the Stage 2 response to the north from the quasi-steady Sverdrup regime to the south. Of course,
 1553 L_τ^x is proportional to the basin scale, and so this one case is not completely convincing. The test is that
 1554 when the east-west scale of the wind stress is made smaller, say $L_\tau^x = L/4\pi$ and thus
 1555 $\tau^y(x) \propto \sin(4\pi x/L)$, while holding the basin width L constant, the adjustment to Sverdrup balance at a
 1556 given y occurs in half the time seen in this case. Thus the relevant east-west scale for adjustment to
 1557 Sverdrup balance is the zonal scale that is imposed on the meridional flow. In the case of a closed basin
 1558 with zonal winds that are independent of x , that scale is the distance to the eastern boundary; in the
 1559 present experiment, this zonal scale comes directly from the wind field itself.

1560 **6 Barotropic and baroclinic circulation of the three layer, free** 1561 **surface model, 3l-fs**

1562 The reduced gravity model is contained within the new three layer model - let $h_2 \rightarrow 0$, and $h_3 \rightarrow \infty$. Thus
 1563 the phenomena of the reduced gravity model are a part of the new model, though with somewhat different

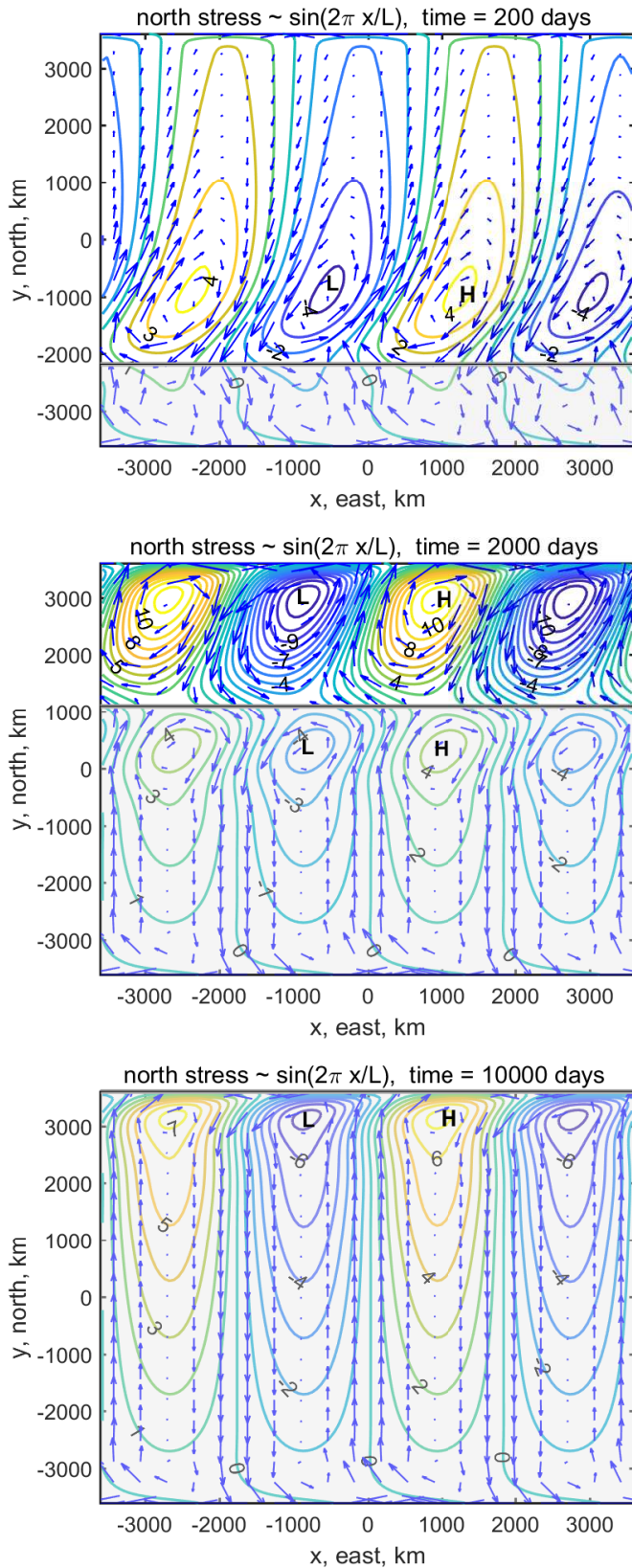


Figure 33: Snapshots from a wind-driven experiment in which the basin is a channel, and the wind stress was northward and x -dependent (Fig. 32, upper). The stress was set to a very small value, 0.01 N m^{-2} . Times were 200, 1000 and 10000 days (upper, middle, lower) after the stress was switched on. The contours are the anomaly of layer thickness in meters and the blue arrows are the current, though with boundary currents omitted. The gray shading extends northward from the southern boundary to a distance Y determined by the time, the y -dependent long Rossby wave speed and the zonal scale of the wind, L_τ , via Eqn. (75). Poleward of Y the flow is in Stage 2. Notice that there is clear evidence of westward propagation in especially the southern part of this region. Equatorward of Y the flow is adjusted to a near steady state Sverdrup balance (Fig. 32, lower). At a given y , the progression from Stage 2 to Sverdrup flow occurs at the same time across the entire channel (independent of x).

1564 amplitudes. The important thing to note is that everything we learned from the reduced gravity model
 1565 makes a useful contribution towards understanding the more comprehensive model results described next.

1566 The solution of the multi-layer model contains additional phenomenon, and especially barotropic
 1567 phenomena, and in general the new solution is more complex since $u = u(x, y, z, t)$ in place of
 1568 $u = u(x, y, t)$. Though the z dimensionality is strongly truncated by a three layer representation, it is
 1569 nevertheless challenging to display the full solution in a manuscript. We have to make choices. To start,
 1570 we are going to emphasize one 'latitude', $y = -1000$ km, which is on the south side of the subtropical
 1571 gyre. At this latitude there is both an appreciable wind stress, $\tau^x = -0.075$ Pa toward the west, and a
 1572 significant stress curl, $\nabla \times \tau = -5.8 \times 10^{-8}$ Pa m⁻¹, which implies clockwise turning. The data from this
 1573 latitude are shown in three forms. 1) At the basin center 'longitude', $(x, y) = (0, -1000)$ km, the current
 1574 east and north components for each layer are shown for the first 30 days in Fig. (34). 2) The meridional
 1575 component of the transport at the same site but for short and long times is in Fig. (35). 3) The meridional
 1576 volume transport across the interior of the basin is in Fig. (36).

1577 6.1 Inertial motion and Ekman transport in the surface layer

1578 For short times, a few tens of days, the surface layer current and transport is familiar from the reduced
 1579 gravity model, or for that matter, a purely local model, viz., near-inertial currents in both components,
 1580 and Ekman transport in the meridional component, (the surface layer is represented by the red lines of
 1581 Figs. (34) - (36). At the site sampled in these figures, $y = -1000$ km, the wind stress is westward, hence
 1582 the Ekman transport is positive (northward) and has the magnitude expected for the wind stress at this
 1583 site. This Ekman transport occurs throughout the model domain, though of course with varying
 1584 amplitude and sign depending upon the local wind stress (Sec. 3.2).

1585 6.2 Transient, barotropic flows

1586 Over the region of negative stress curl that becomes the subtropical gyre, the Ekman transport is
 1587 convergent. If that was all that was relevant, this Ekman convergence would thicken the surface layer at a
 1588 rate of about 3 cm per day. In the context of a reduced gravity model, this produces a slowly growing
 1589 baroclinic pressure gradient, and consequently a slowly increasing baroclinic, geostrophic current. By
 1590 slowly we mean that it takes hundreds of days for this purely baroclinic process to produce an
 1591 appreciable response. The presence of an active (or free) sea surface and an active abyssal layer in the

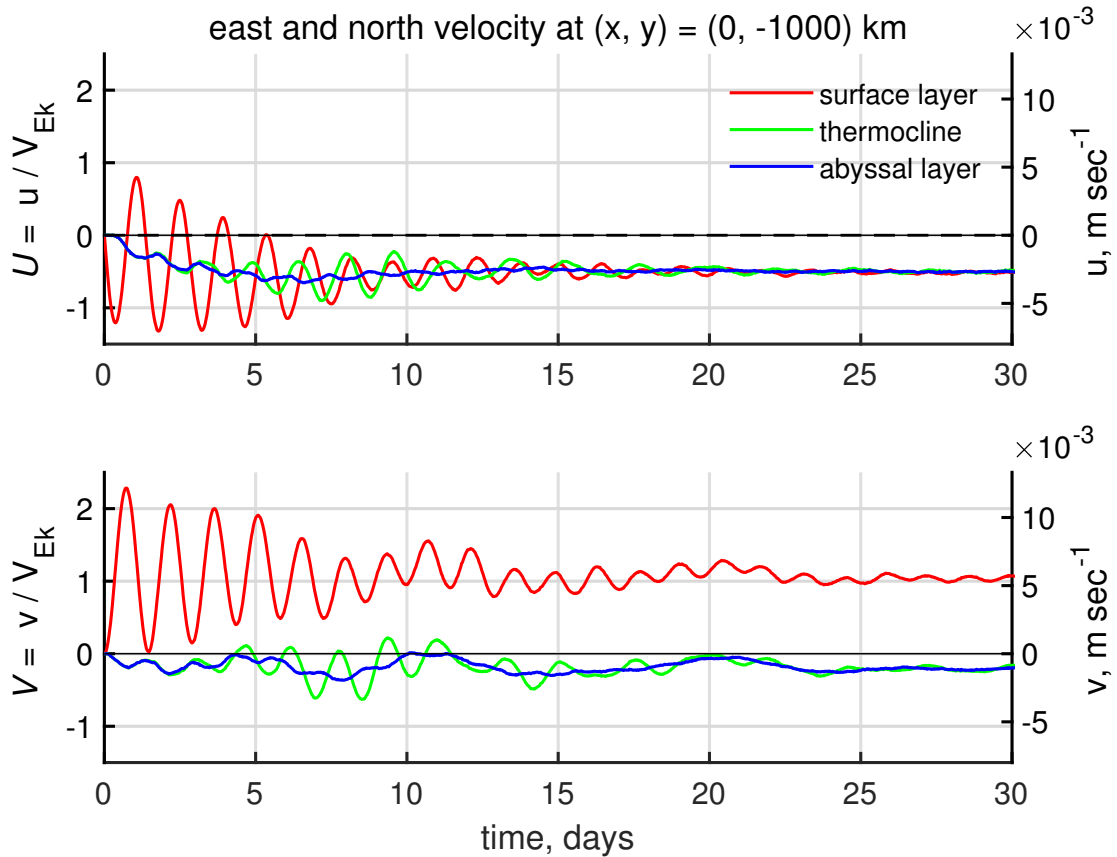


Figure 34: The short time evolution of the east and north components of the current computed by the three-layer model and sampled on the southern side of the subtropical gyre, $(x, y) = (0, -1000)$ km. Currents are normalized by the Ekman velocity scale, Eqn. (40), evaluated at this location, $V_{Ek} = 5 \times 10^{-3}$ m sec^{-1} . **(upper)** East currents in each of the the three layers; surface layer currents are in red, etc. The high frequency oscillations seen here are near-inertial motion. The time-mean of u is associated with barotropic Sverdrup flow discussed in the main text of the Appendix. **(lower)** North currents. The time mean dimensional current is about 5×10^{-3} m sec^{-1} and the non-dimensional value is about 1. This is as expected if the surface layer current is mainly Ekman flow. Layers 2 and 3 are unaffected by the direct wind stress, but nevertheless evidence a small, southerly barotropic Sverdrup flow that is modulated by barotropic Rossby waves having a period of about five days. The barotropic (depth independent) motions are much more prominent in the transport, bext figure.

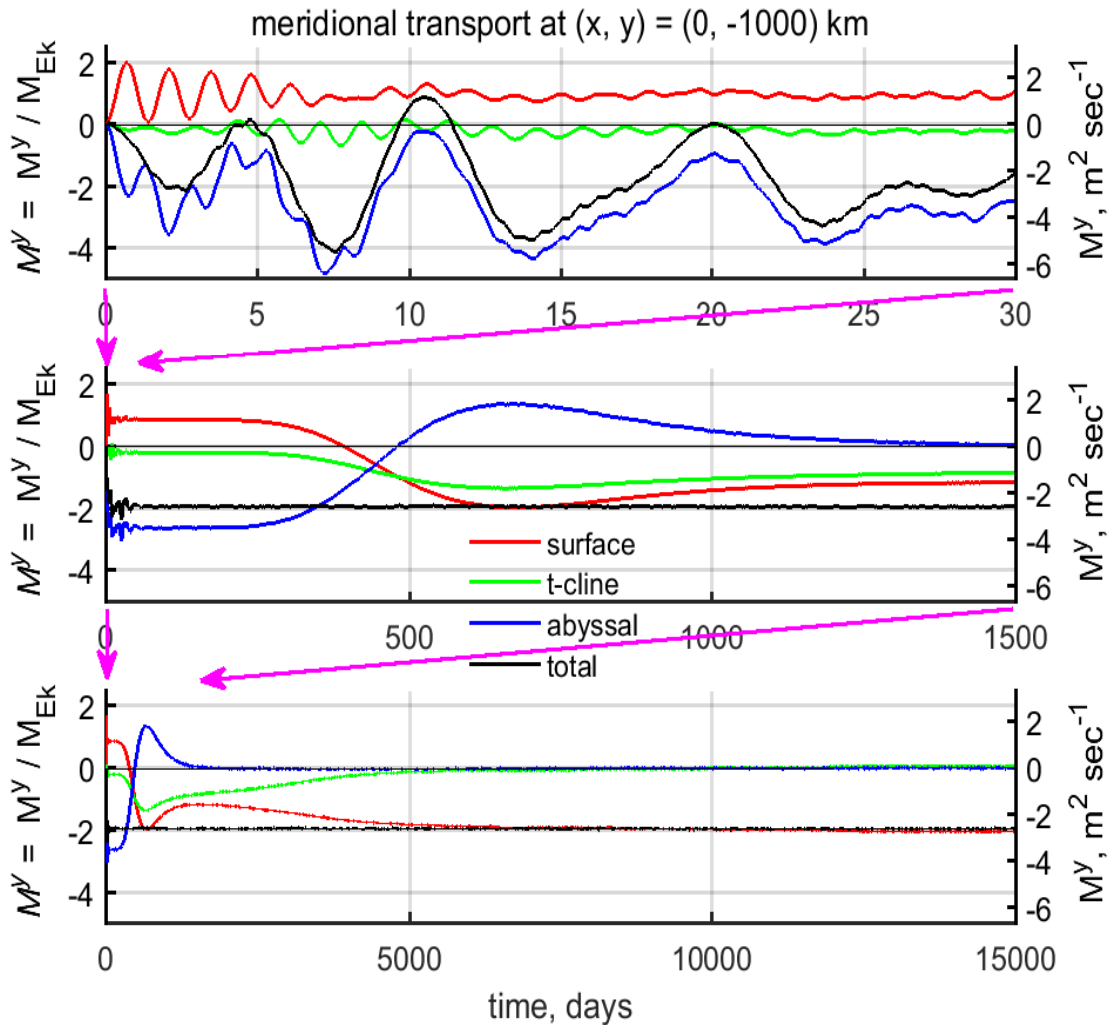


Figure 35: The meridional component of the transport at $(x, y) = (0, -1000)$ km. The data are shown on three time scales, (**upper**) 0 - 30 days, (**middle**) 0 - 1500 days, and (**lower**) 0 - 15000 days. Dimensional scale is shown at right, and nondimensional scale is at left. In this figure the transport is normalized with the expected Ekman transport magnitude at this y , $M_{Ek} \approx 1 \text{ m}^2 \text{ sec}^{-1}$. The surface layer transport (red line) is mainly Ekman transport and is northward. The total transport (all three layers) is the black line, which notice, has a very large contribution from the abyssal layer at short times, and is southward.

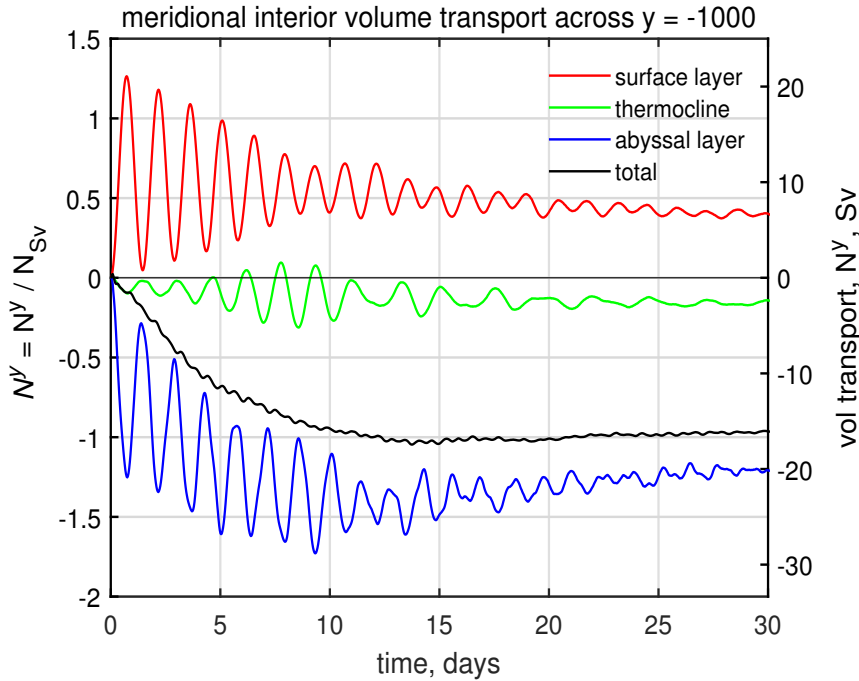


Figure 36: Meridional volume transport in the basin interior across $y = -1000$ km. The transport has been integrated from the eastern boundary to within 200 km of the western boundary. The volume transport within the surface layer (red line) is mainly Ekman transport and is northward as in the previous figure. The volume transport in the thermocline and abyssal layers is shown by green and blue lines; the sum over the three layers (the full water column) is the total volume transport shown as the black line. The dimensional scale is at right, and a nondimensional scale based upon the expected Sverdrup transport magnitude at this y , $N_{Sv} = 17$ Sv, is at left. Notice that the total transport appears to be quasi-steady from day 10 onward, and is -1 in these nondimensional units. Hence, the total transport is consistent with Sverdrup transport at this y .

1592 present model gives a much quicker barotropic response. A thickening of the surface layer by a few
 1593 centimeters will tend to cause a positive displacement of the sea surface by a few centimeters/2. A
 1594 displacement of the Layer 2 interface by this amount is hardly noticeable, but a displacement of the sea
 1595 surface by a few centimeters is significant insofar as it produces a significant pressure gradient and thus
 1596 flow within the thick abyssal layer. The resulting abyssal and thermocline layer currents are small
 1597 amplitude, but the associated transport (current times thickness) is significant since the abyssal layer is
 1598 very thick, (Fig. 35). For short times, a few weeks or even just a few days (Fig. (36, upper) the
 1599 meridional transport at the observation site $(x, y) = (0, -1000)$ km shows a time mean to the south, and
 1600 a pronounced oscillation having a period of about five days. These oscillations are associated with short,
 1601 barotropic Rossby waves, which like higher frequency inertial oscillations, are an unintended byproduct
 1602 of the impulsive start of the wind stress.

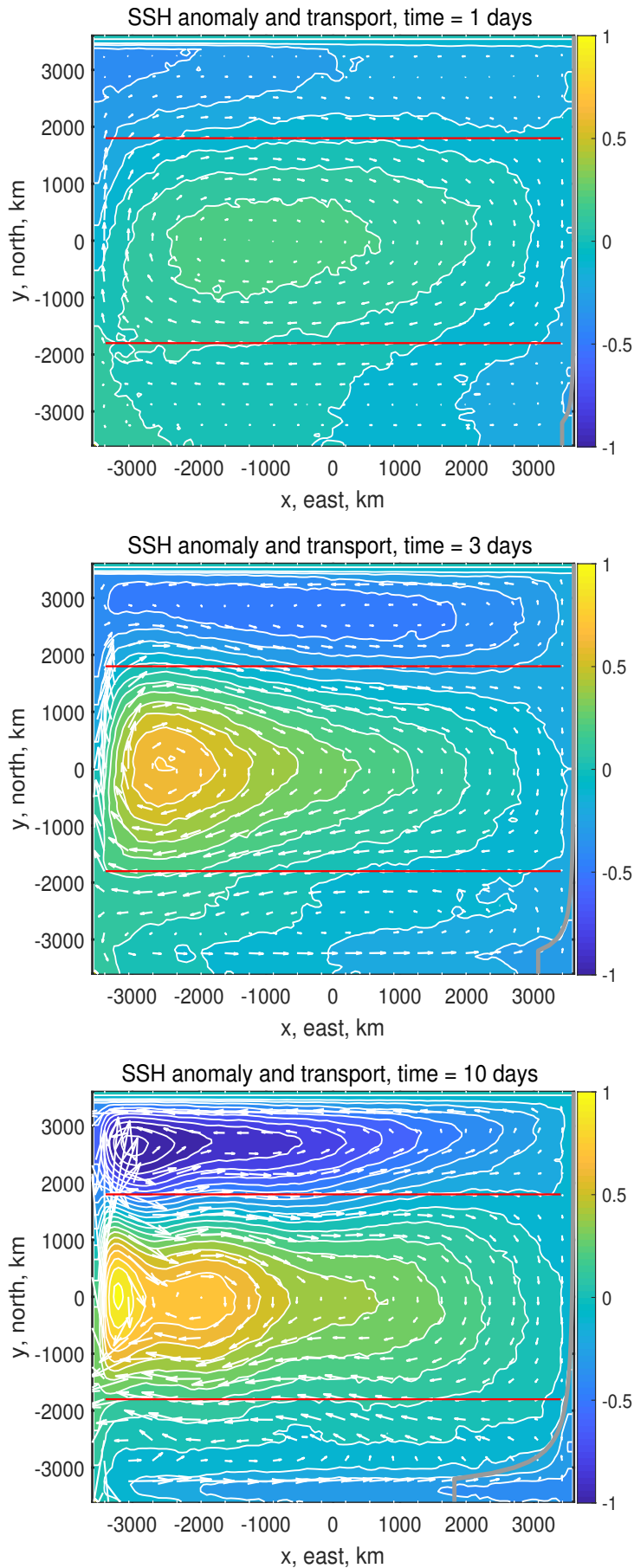


Figure 37: Three snapshots of SSH anomaly from a wind-driven, three-layer experiment at 1 day, 3 days and 10 days (top to bottom) after wind stress was switched on. The thin red horizontal lines are the axis of the westerly and easterly wind stress (Fig. 5). The small white arrows are the transport, though with the comparatively very large transports within the wbc omitted. The contours and colors are the SSH anomaly normalized with the barotropic Sverdrup SSH scale, Eqn. (77), evaluated at 30° N $\eta_{Sv-btr} = 0.06m$. The largest positive SSH anomaly at day 10 is (dimensional units) $\eta \approx 0.06$ m in the western central subtropical gyre, and the greatest negative value is ≈ -0.09 m in the western subpolar gyre. The basin scale pattern evident here, *viz*, three highly asymmetric gyres, persists with minor changes for hundreds of days. An animation of these data is at www.whoi.edu/jpweb/BaroSver.mp4

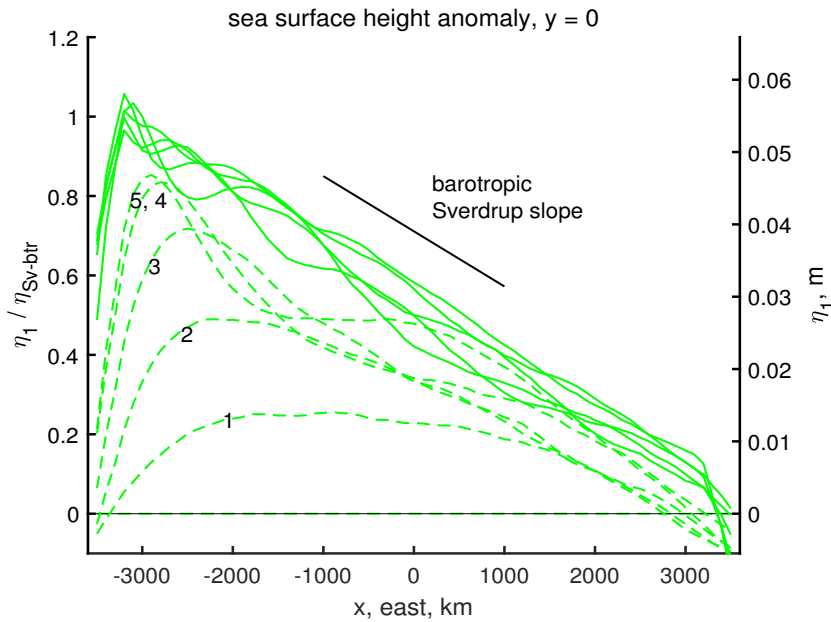


Figure 38: Successive cross-basin profiles of SSH anomaly along $y = 0$. The first five days are the dashed green lines at 1 day intervals, and the next 25 days are solid green lines at 5 day intervals. The amplitude is scaled with the barotropic scale, Eqn. (76) which, for the parameters of this experiment, $\eta_{Sv-btr} = 0.05$ m. Note that on day 1 the SSH was a fairly symmetric mound. By day 3 this mound had shifted noticeably to the west, implying very rapid westward propagation, $O(1000 \text{ km day}^{-1})$. After only about a week, the SSH slope over the interior region was close to the slope expected for a barotropic Sverdrup flow in geostrophic balance.

1603 6.3 Basin scale circulation; barotropic Sverdrup flow

1604 The convergence of Ekman transport in the middle of the model domain leads to a small positive SSH
 1605 anomaly and thus a high pressure, Figs. (37) and (38). On day 1, SSH was a fairly symmetric mound
 1606 with an amplitude of about 1 cm, centered in the model domain, and accompanied by geostrophic
 1607 currents that flowed clockwise around the high pressure. These currents were subject to the beta-effect,
 1608 divergence where the flow was southerly and convergent where it was northerly. The result is that the
 1609 growing SSH anomaly had a tendency for a beta-induced westward translation, just like we have seen for
 1610 a mesoscale eddy. A key difference is the rate, $O(1000 \text{ km day}^{-1})$, which is much, much faster than
 1611 westward translation of baroclinic mesoscale eddies and baroclinic Rossby waves. This speed is in the
 1612 range of long, barotropic Rossby waves. By day 3, the positive η_1 was compressed up against the western
 1613 boundary, and by day 10 the slope over the interior of the subtropics was an almost uniform tilt down
 1614 from west to east. The plan view of the SSH shows cyclonic gyres in the tropics and subpolar regions and
 1615 an anti-cyclonic gyre that fills the subtropics. Thus within the first ten days of the experiment, the ocean
 1616 circulation develops as three gyres that in many respects — save for their depth-independence and small
 1617 amplitude — are a foretelling of the baroclinic circulation that will follow in the next several years of this
 1618 integration, and that was the major topic of the main essay.

1619 If the barotropic flow in the interior is consistent with the Sverdrup relation, then the barotropic

1620 meridional velocity is

$$1621 \quad V_{Sv-btr} = \frac{1}{\rho_o H \beta} \nabla \times \tau.$$

1622 Along $y = 0$, the center of the subtropical gyre, the expected Sverdrup flow has a dimensional amplitude
 1623 $V_{Sv-btr} = 1.0 \times 10^{-3} \text{ m sec}^{-1}$. In the gyre center $y = 0$, the wind stress and Ekman flow vanish, and so
 1624 this V_{Sv-btr} is nearly geostrophic. The sea surface slope is thus expected to be

$$1625 \quad \frac{\partial \eta_{Sv-btr}}{\partial x} = \frac{f}{g} V_{Sv-btr} = \frac{f}{\rho_o g H \beta} \nabla \times \tau. \quad (76)$$

1626 If this holds across the entire basin, then the SSH amplitude across the basin is just

$$1627 \quad \eta_{Sv-btr} = 2L \frac{\partial \eta_{Sv-btr}}{\partial x} = \frac{2fL}{\rho_o g H \beta} \nabla \times \tau. \quad (77)$$

1628 For the present experiment at $y = 0$, $\eta_{Sv-btr} \approx 0.06 \text{ m}$. These estimates are very close to the slope and
 1629 SSH amplitude found in the numerical experiment, Fig. (38), but are much, much less than the amplitude
 1630 found in the western subtropical North Atlantic, which is about 1 m east-to-west, Fig. 1. At this time the
 1631 volume transport within the subtropics was very close to that expected from the Sverdrup relation (Fig.
 1632 39, left), and of the expected sense in the tropics and subpolar regions. As we saw before with the
 1633 reduced gravity model, there is a rather wide region adjacent to the northern and southern boundaries
 1634 within which the meridional transport goes to zero as it must to satisfy the no normal flow condition on
 1635 the solid boundaries. At this short time, the Sverdrup transport occurred throughout the water column,
 1636 and in fact was mainly in the abyssal layer, Fig. (39, right).

1637 **6.4 Baroclinic adjustment to a surface intensified, steady state**

1638 After the first week, the SSH slope over the interior appeared to be quasi-steady. However, there was also
 1639 evidence that SSH was continuing to evolve, albeit slowly. Sea level was rising very slowly over the
 1640 entire subtropics, and, there was a region of much steeper SSH slope developing close to the eastern
 1641 boundary and spreading slowly westward. This was the start of a baroclinic adjustment toward a
 1642 surface-intensified, steady state.

1643 The currents at $(x, y) = (0, -1000) \text{ km}$ continued to evolve, albeit very slowly compared to the very
 1644 rapid onset of the barotropic state. The abyssal layer transport, which early on made up most of the total
 1645 Sverdrup transport, began to weaken at about 400 days, and then oscillated once and settled to nearly
 1646 zero at about 1400 days, Fig. (35, middle). The total transport remained consistent with Sverdrup

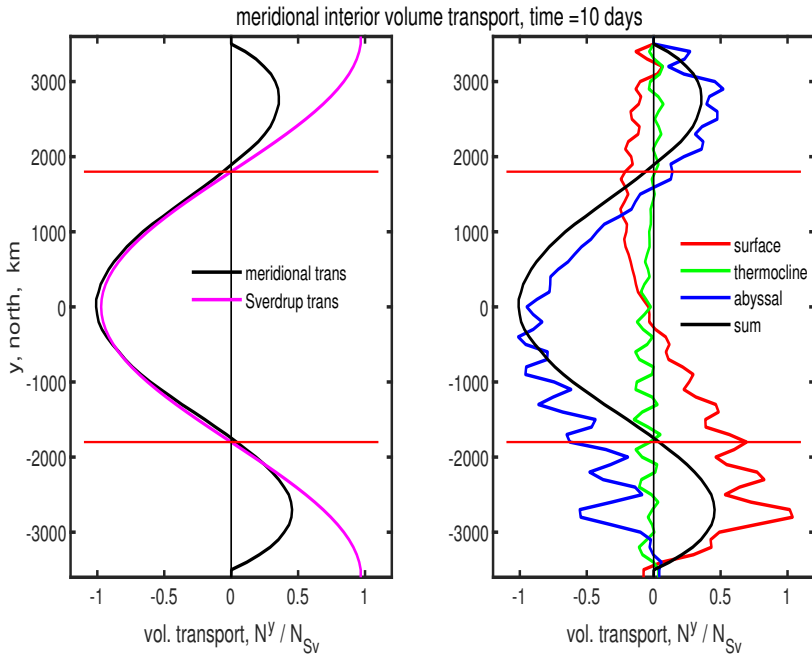


Figure 39: Meridional volume transport across the interior portion of the basin for all y and at time = 10 days. **(left)** Total transport (black line) and the expected Sverdrup transport (magenta). These are very similar over the subtropical gyre, but differ considerably near the northern and southern boundaries where the actual meridional transport must vanish. **(right)** Meridional transport in each of the layers of the three layer model, and summed to give the total transport, the black line, which is the same as at left.

1647 transport, but thereafter, the Sverdrup transport was contained within the thermocline and surface layers.
 1648 At about 1500 days, the thermocline layer transport started a slow decrease and then nearly vanished by
 1649 about 7000 days, Fig. (35, lower). Thereafter, the Sverdrup transport was contained almost entirely
 1650 within the surface layer. These times, very roughly 1000 days and 5000 days, are very broadly consistent
 1651 with the expected transit time of the first and second baroclinic modes from the eastern boundary to the
 1652 basin center, about 700 days and 2700 days for the first and second baroclinic modes at this y which is
 1653 equivalent to about latitude = 22° . Consistent with this, and perhaps more convincing of a modal
 1654 description is that the change of the current profile over time looks a lot like the first and second
 1655 baroclinic modes (Fig. 41), e.g., from 1500 days to 7000 days the change in the current is consistent with
 1656 the arrival of a second mode (the abyssal layer remains at rest, while the thermocline and surface layers
 1657 accelerate in opposite directions). If you look closely you can see that the change in the current profile is
 1658 not exactly like a second mode in that the decrease of the thermocline layer is greater in amplitude than
 1659 the is the evident increase of the surface layer. The size of the change is inversely proportional to the
 1660 layer thicknesses, which at this time had changed quite a lot from the initial values; the surface layer was
 1661 considerably thicker and the thermocline significantly thinner than in the initial state, Fig. (42).

1662 The total transport — Sverdrup transport — is unchanged as these baroclinic waves pass by, but the
 1663 distribution of the transport becomes increasingly surface intensified. In the final, steady state, the
 1664 Sverdrup transport occurs entirely within the surface layer. At one level this is not surprising, as the
 1665 surface layer absorbs all of the wind stress and stress curl. Thus, only the surface layer can sustain a

1666 steady meridional flow in the presence of a beta effect. The deeper layers can be set into motion during
1667 the transient stage of the response, since they are subject to pressure gradients, and hence can sustain
1668 geostrophic motion. They are also subject to being compressed and stretched, Fig. (43), and so can
1669 display some of the consequences of potential vorticity conservation, i.e., there can be a q-conserving
1670 flow in the deep and thermocline layers so long as they are being stretched. However, this can not
1671 continue into a steady state in which stretching (time changing thickness) vanishes.

1672 7 Summary and closing remarks

1673 7.1 O1: East-west asymmetry of the subtropical and subpolar gyres

1674 **Sverdrup flow over most of the interior of a basin.** The basin-scale, horizontal structure of the
1675 wind-driven ocean circulation, including western intensification and several of the qualitative differences
1676 between tropical, subtropical and subpolar gyres, have a plausible analog in solutions of the shallow
1677 water model. Over the subtropical North Atlantic, where the wind stress curl is negative, the interior
1678 meridional flow is southward as expected from the Sverdrup relation. Over the tropical and subpolar
1679 regions, the stress curl is positive and the meridional flow is northward, also as expected from the
1680 Sverdrup relation. This general result — that the Sverdrup relation provides a plausible and useful
1681 explanation of the major wind-driven gyres — has been accepted since at least the 1940s, and has been
1682 tested and validated quantitatively in modern, field data-based studies⁵.

1683 The Sverdrup relation is expected to be valid provided that the dominant processes of the potential
1684 vorticity balance are just two: the beta effect acting upon a very gentle and thus linear meridional current
1685 balanced by the curl (torque) of the wind stress. In practice, this holds in the majority of interior regions
1686 that are well away from zonal or meridional boundaries.

1687 **Departures from Sverdrup flow in zonal and meridional boundary regions.** In a steady
1688 circulation, the meridional Sverdrup transport across every zonal, cross-basin section must be returned in
1689 the opposite direction by some other process. In the shallow water model and in the real ocean, this
1690 return flow occurs in a comparatively narrow and thus very intense western boundary current (wbc). The
1691 wbc is northward in the subtropical gyre where the Sverdrup transport is southward, and reversed in the
1692 subpolar and tropical gyres. The width of the western boundary region is observed to be very narrow,
1693 $O(100 \text{ km})$. In the present shallow water model, the width of the wbc is the baroclinic radius of

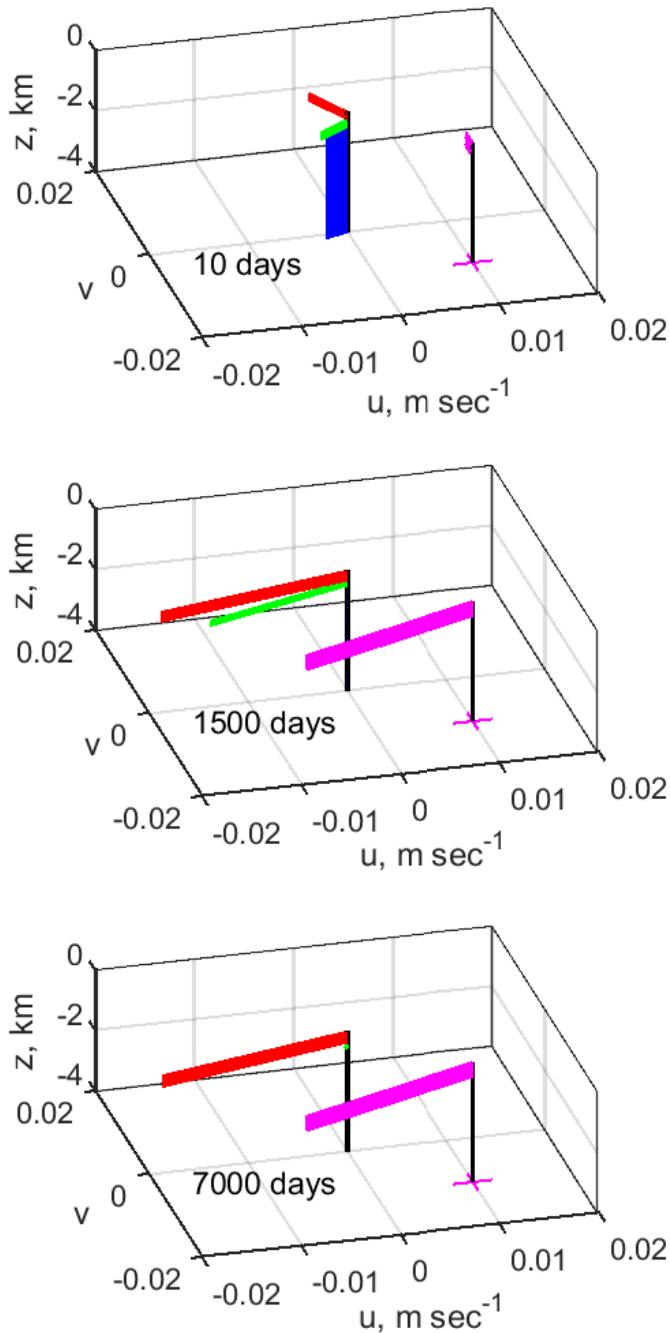


Figure 40: Current profiles from the site $(x,y) = (0, -1000)$ km, shown at three times, **(top)** to **(bottom)**, 10 days, 1500 days and 7000 days. Red, green and blue are the surface layer, thermocline and abyssal layers, respectively. An abyssal layer flow is appreciable only in the top panel. The view is towards the north-northeast. Notice that the profile goes from being barotropic with a small Ekman flow in the surface layer at 10 days, to entirely surface trapped at 7000 days. At this site the flow in the steady Sverdrup regime at 7000 days is somewhat stronger in the zonal direction than in the meridional direction, cf. Fig. (44). The magenta vectors are from the reduced gravity model, and offset by $(u,v) = (0.01 - 0.01)$ m sec⁻¹. They are very similar to the three layer model currents except at very short time.

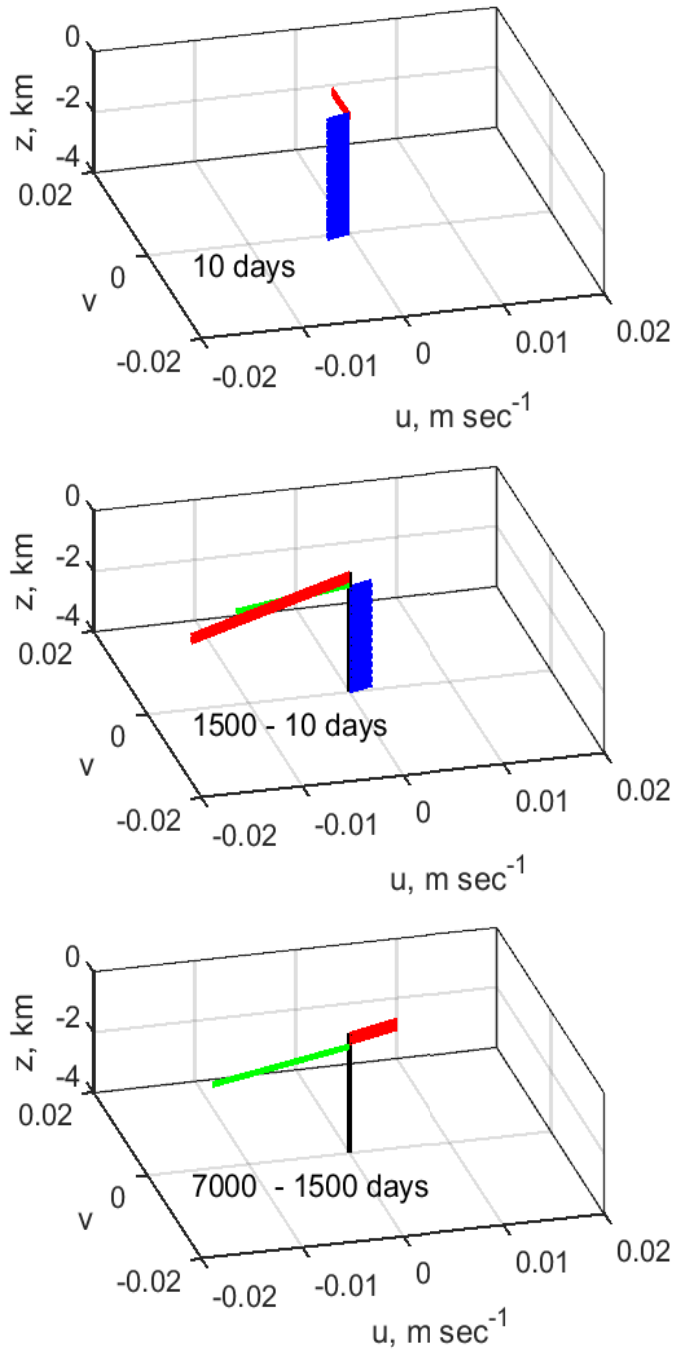


Figure 41: Current difference profiles from the site $(x,y) = (0, -1000)$ km, shown at three times, **(top)** to **(bottom)**, 10 days, 1500 days and 7000 days. In the top panel, the red arrows are the Ekman flow, and blue vectors are the depth independent barotropic flow at 10 days. The middle panel is the velocity difference, $u(t = 1500) - u(10 \text{ days})$. Red, green and blue are for the surface, thermocline and abyssal layers as in the previous figure. Notice that velocity difference at this time is qualitatively much like the first baroclinic mode (Fig. 7). The bottom panel is the velocity difference $u(t = 7500) - u(1500 \text{ days})$. There is essentially no signal from the abyssal layer, while the surface and thermocline layers are in approximately opposite directions. This shape is much like the second baroclinic mode.

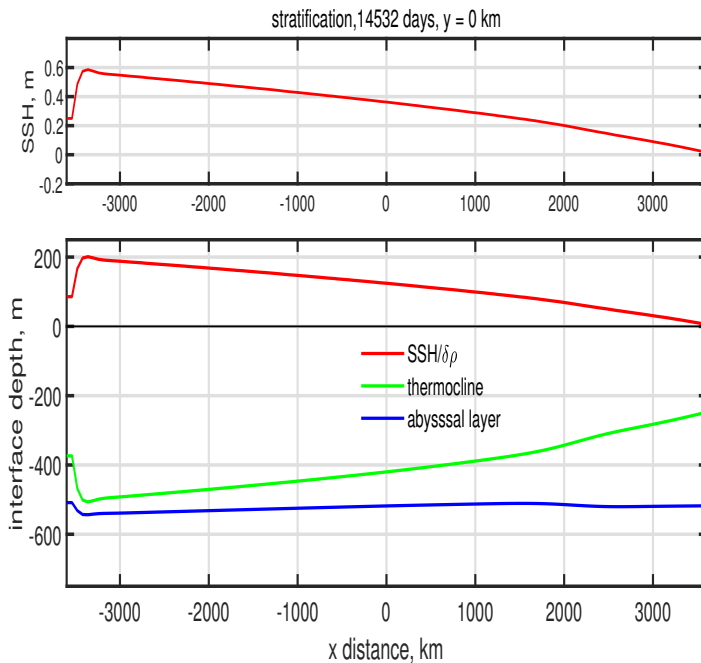


Figure 42: The SSH (upper panel, red line) and the interface between layers across the basin at $y = -1000$ km (red, green and blue; lower panel). Notice that the interface between the abyssal and thermocline layers (blue line) is essentially flat; there is almost no flow in the abyssal layer or the thermocline at this time. Also, note that the surface layer thickens markedly to the west and is generally much thicker than it was in the initial condition (250 m). The thermocline is generally much thinner.

1694 deformation, the natural length scale of a shallow water model. The inviscid, linear Sverdrup interior fills
 1695 the rest of the basin, 7000 km, and hence the westward intensification (east-west asymmetry) of the major
 1696 ocean gyres is very pronounced, about 7000/100 in a North Atlantic-size basin.

1697 The meridional flow must vanish on zonal boundaries. In the present model, the zonal boundary
 1698 dynamics includes a significant contribution from linear friction, which is dubious as a model of
 1699 dissipation in the real ocean. The width (north-south extent) of the affected zonal boundary region is
 1700 rather wide, $O(1000$ km) and thus the meridional flow in the northern half of the subpolar region is
 1701 somewhat less than would be expected from a Sverdrup balance.

1702 7.2 O2: Time scales of the wind-driven circulation

1703 **Startup time of the baroclinic circulation.** A wind-driven, start-up experiment in the 1l-rg (one layer,
 1704 reduced gravity) model shows that the baroclinic circulation at a given point in the interior reaches an
 1705 approximate, steady, Sverdrup flow some time after the passage of what amounts to a long, baroclinic
 1706 Rossby wave starting from the eastern boundary. The long Rossby wave speed, $\beta C^2/f^2$, which has a
 1707 strong dependence upon latitude, is thus a crucial parameter in the time-dependent response of a

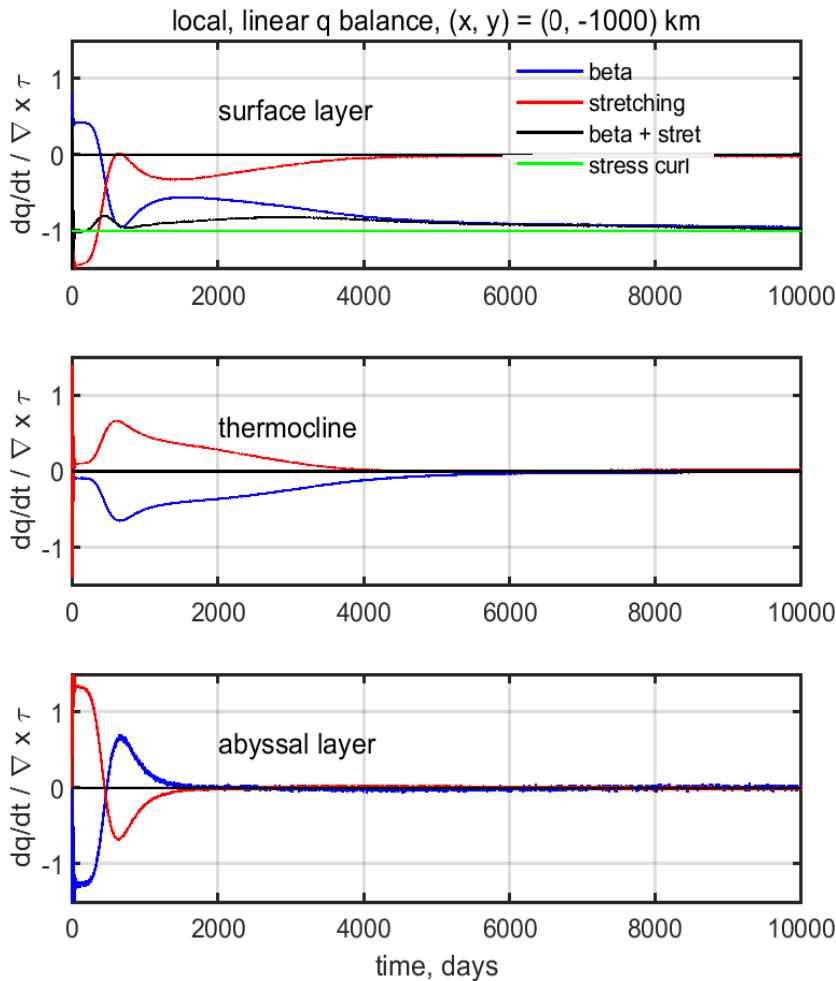


Figure 43: The linear balance of potential vorticity in, top to bottom, the surface layer, the thermocline and the abyssal layer.

1708 wind-driven gyre. For a North Atlantic-sized basin, the elapsed time required to reach full steady state is
 1709 about thirty years at a subpolar latitude, about five years in the subtropics, and much less, about a year, in
 1710 the tropics.

1711 **Annually-varying winds.** This marked latitudinal variation in the rise time of the baroclinic
 1712 wind-driven circulation is relevant to understanding the observed response to an annually-varying wind
 1713 stress. Model experiments that assumed a $\pm 50\%$ annual period variation of the wind stress find that the
 1714 subpolar circulation varies almost not at all, the subtropical gyre varies only a little, while some aspects
 1715 of the tropical circulation vary quite a lot. The transport of the tropical wbc varies by only about $\pm 10\%$,
 1716 but the zonal flow in the eastern half of the tropical gyre varies by $\pm 50\%$. This latter variation is mainly a
 1717 local a response to the annually-varying stress curl, and partly a Sverdrup flow. Thus a seasonally varying

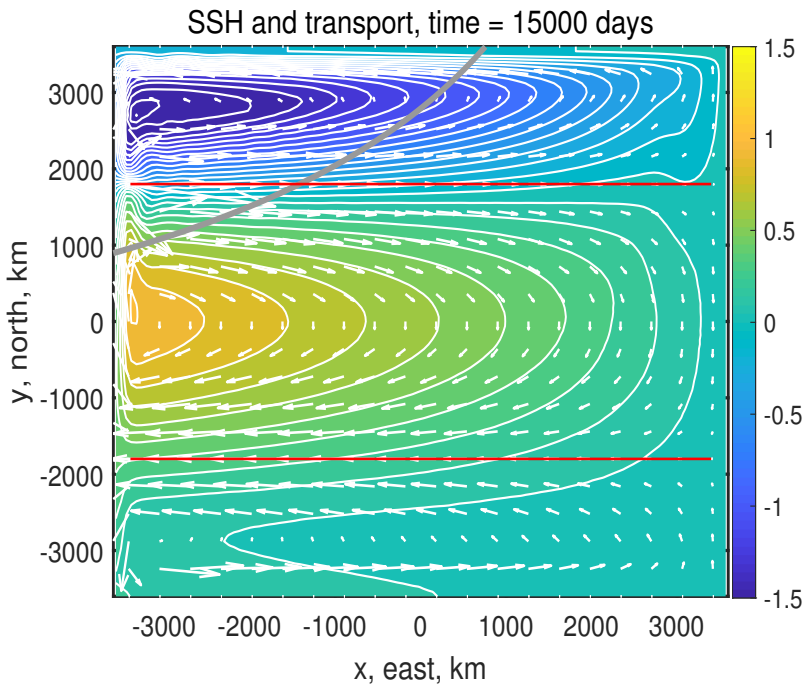


Figure 44: SSH anomaly from the three layer model experiment at time 15000 days. The thin red horizontal lines are the axis of the westerly and easterly wind stress (Fig. 5). The small white arrows are the transport, though with the comparatively very large transports within the wbc omitted. The SSH anomaly is nondimensionalized by the baroclinic scale, $\eta = 0.9$ m. The parabola at upper left is the second baroclinic eastern boundary wave, which notice, has still not swept the entire basin.

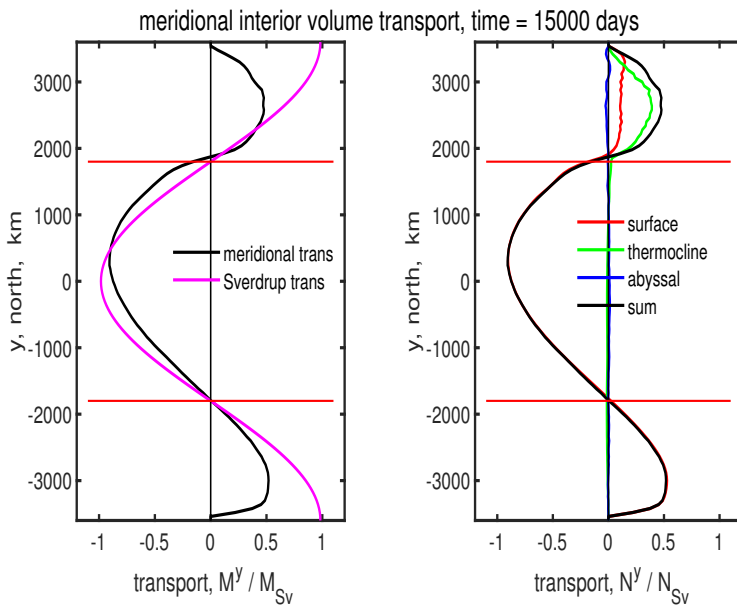


Figure 45: Meridional volume transport across the interior portion of the basin for all y and at time = 15000 days. **(left)** Total transport (black line) and the expected Sverdrup transport (magenta). These are similar over the subtropical gyre, but differ considerably near the northern and southern boundaries where the actual meridional transport must vanish. **(right)** Meridional transport in each of the layers of the three layer model, and summed to give the total transport, the black line, which is the same as at left. Notice that the total transport is mainly in the surface layer except in the subpolar gyre where there is still considerable transport in the thermocline, cf. Fig. (44).

1718 wind stress that will have almost no effect on the subpolar or subtropical circulation (interior or wbc) and
1719 yet will produce a fairly pronounced response of especially the zonal, open ocean SSH and currents
1720 within the eastern tropical ocean.

1721 **Barotropic circulation.** This essay emphasizes the baroclinic circulation because that is what we
1722 can see in the kinds of observations that are most widely available — SSH from satellites and upper
1723 ocean density from a variety of *in situ* methods, e.g., Figs. (1) and (2). As well, baroclinic circulation
1724 contributes the majority of meridional heat transport by the oceans. However, we shouldn't dismiss out of
1725 hand the possibility and importance of a barotropic circulation (which is inaccessible to the 1l-rg model).
1726 To get a sense of the barotropic circulation requires a model with a free (moving) sea surface and that
1727 supports very fast barotropic waves (here, 3l-fs). Now let's ask the question — how long does it take to
1728 establish a quasi-steady Sverdrup regime after the onset of a wind field? The answer is about one week, if
1729 we acknowledge the barotropic response. The currents associated with the barotropic response are
1730 distributed throughout the water column, and hence the upper ocean current is very small. Similarly, the
1731 SSH signature is about 10% of that observed.

1732 7.3 What's gone missing?

1733 This essay has emphasized the basin-scale horizontal structure and the time scales of the wind-driven
1734 circulation in no small part because that is what the shallow water model can do without misleading us.
1735 What does the shallow water model miss?

1736 **Amplitude and vertical structure.** The amplitude of the circulation is very important too, of course,
1737 and here the assessment of the Sverdrup relation in the present idealized solutions is problematic. The
1738 SSH anomaly in the numerical subtropical gyre (Fig. 11) is about 0.4 m, while the SSH anomaly of the
1739 North Atlantic subtropical gyre Fig. (1) is considerably greater, more like 1.1 m. The underestimate
1740 made by the shallow water model is likely contributed by several sources. In the first place, the shallow
1741 water model gives the meridional volume transport and not SSH *per se*. The gradient of SSH is
1742 diagnostic of the surface geostrophic velocity, not the water column integral that is volume transport. The
1743 transport in the numerical model is not sensitive to the stratification. Thus if the model's layer thickness
1744 is made smaller, say $h_o = 250$ m, then the current speed is roughly doubled, as is the predicted SSH
1745 anomaly and slope. The comparatively large initial value of h_o used here, 500 m, was necessitated by the
1746 numerical (non-physical) requirement that h could not be allowed to vanish anywhere in the model
1747 domain. This is especially at issue for the subpolar gyre where the change in layer thickness was very
1748 large. This need for a large h_o is a kluge that betrays a physical deficiency of the present shallow water

1749 model: a more complete and realistic model physics should include multiple layers in the vertical, as well
1750 as a vertical mixing process that would serve to keep the directly wind-driven surface layer of the ocean
1751 finite and realistic no matter what the upwelling might be.

1752 **The overturning circulation and eddy variability.** The discrepancy in SSH amplitude involves much
1753 more than just a detail of the vertical structure. There is known to be considerably larger transport in the
1754 observed Gulf Stream than is predicted by the Sverdrup relation in numerical ocean models that have
1755 much better vertical resolution and fully realistic wind fields.⁴ The larger-than-Sverdrup western
1756 boundary current transport in the North Atlantic likely arises from two very different sources. We have
1757 already had occasion to note that a global scale, meridional overturning circulation contributes about 20
1758 Sv to the poleward-going, upper ocean transport at the latitude of the subtropical gyre. Deep, cold
1759 currents, well below the thermocline, provide mass balance across zonal sections. These are completely
1760 missing from the present shallow water model. As well, the vigorous eddying of the Gulf Stream
1761 (subtropical western boundary current) is known to produce an intense, and nearly depth-independent
1762 recirculating gyre which also adds significantly to the poleward transport of the western boundary current
1763 and so contributes to the large positive SSH anomaly of the observed subtropical gyre. The Sverdrup
1764 relation applied to the North Atlantic basin certainly isn't wrong, but neither is it the complete story of
1765 the ocean circulation.

1766 7.4 Acknowledgements

1767 Thanks to Iam-Fei Pun of WHOI for careful comments on a previous draft of this essay, and to Jiayan
1768 Yang of WHOI for encouraging the inclusion of barotropic dynamics.

1769 8 Supplemental material

1770 8.1 Links to models and updated manuscripts

1771 The code used to solve the wind-drive circulation problems discussed here is very similar to that used in
1772 the Parts 2 and 3 treatments of geostrophic adjustment and eddy propagation. However, the data required
1773 to specify the configuration of the wind-driven experiments is sufficiently different that a dedicated

1774 program was written:

1775 **gyre.for** is a Fortran code that solves the shallow water equations for the wind-driven
 1776 circulation in an enclosed ocean basin. A variety of wind stress forms and time histories may
 1777 be specified. The numerical methods are not highly sophisticated or complex, and the code
 1778 should be fairly amenable to modification. The longest integrations shown here will run in a
 1779 few hours on a fairly capable, PC workstation. Output goes to a Matlab.mat file which may
 1780 be read by a Matlab script,

1781 **gyre_plot.m** makes several kinds of diagnostic plots from the data generated above.

1782 This model and the most up to date version of these essays may be downloaded from the author's web
 1783 page, <https://www2.whoi.edu/staff/jprice/>

1784 8.2 Homework problems

- 1785 1. At 30° N, $f = \Omega$, and the inertial period is $2\pi/\Omega = 23$ hrs, 56 min, or less than a day by $\approx 1/365$
 1786 days. Can you explain where this small difference with a day comes from?
- 1787 2. Starting with Eqns. (5) and (8), eliminate v to derive the corresponding governing equation for h . Is
 1788 it significant that this wave equation is first order vs. the more common second order equation, e.g.,
 1789 shallow water gravity waves? What is the consequence of the beta effect in the case that the zonal
 1790 gradient of thickness is positive? Is it relevant that the momentum balance Eqn. (5) is geostrophic?
- 1791 3.
- 1792 4. The steady solution Fig. (37) includes three gyres, tropical, subtropical and subpolar. Contrast the
 1793 model-computed tropical and subpolar gyres with respect to the magnitude of their currents, layer
 1794 thickness anomaly, and transports. Compare the solution Fig. (37, lower) with the observed SSH of
 1795 Fig. (2). Why does the tropical gyre (or region) have a comparatively small SSH anomaly? The
 1796 subpolar and tropical gyres have roughly comparable anti-clockwise circulations, and yet the wind
 1797 over the subpolar gyres is westerly, and the wind over the tropical gyre is easterly. But haven't we
 1798 been saying all along that these gyres are wind-driven?
- 1799 5. Explain the signs and the comparative magnitudes of the current components of Fig. (12). Notice
 1800 that the Sverdrup meridional flow at the three sites is not identical. Why is there a small but
 1801 systematic difference?

- 1802 6. The overall pattern of SSH (Fig. 6, lower) and of the transport streamfunction (Fig. 11, left) are
1803 similar but not identical. Why is there a difference?
- 1804 7. The potential vorticity derivation of the Sverdrup relation in Sec. 5.1 omitted some important
1805 details. 1) Can you show that the drag term in the q -balance equation for the interior is proportional
1806 to the Ekman number times L_{Earth}/L_{tau} , where L_{tau} is the horizontal scale of the wind stress field.
1807 2) Given speed and space scales of the interior (Sverdrup) flow, show that the relative vorticity of
1808 the Sverdrup flow is indeed very, very small compared to planetary vorticity, f , and so to an
1809 excellent approximation the potential vorticity in the interior is given by $q \approx f/h$. 3) The advective
1810 term of Eqn.(34) may be approximated as Eqn. (13) because the geostrophic flow does not advect
1811 layer thickness. What evidence can you find in the steady solution, Fig. (37), that supports this
1812 (highly plausible) assertion?
- 1813 8. The real ocean thermocline is continuously stratified in the vertical, and so the best one layer
1814 baroclinic model representation of the thermocline will likely have to compromise on something.
1815 The values used here, $H = 500$ m, and $\delta\rho = 2 \text{ kg m}^{-3}$ are round numbers that give an appropriate
1816 gravity wave speed. What thickness slope is consistent with the Rossby wave view of the
1817 subtropical gyre developed in Sec. 4.4, and where is that slope found in the water column of Fig.
1818 (1)?
- 1819 9. Assuming that the boundary current will have a maximum current adjacent to the boundary (and so
1820 a single sign of relative vorticity), show that the mode $\beta = drag$ can obtain also for the case of
1821 an equatorward western boundary current as occurs in the tropical and subpolar gyres. Can you
1822 envision this balance for an eastern boundary current of either sign?
- 1823 10. In the discussion of the Stage 3 transient response we noted that the change in the current from
1824 Stage 2 zonal flow to meridional Sverdrup flow occurs at a time that is proportional to the transit
1825 time of a long Rossby wave starting from the eastern boundary. This suggests an interesting
1826 derivation of the Sverdrup relation (albeit for a slightly special wind field) that makes especially
1827 clear the crucial role of the eastern boundary in a problem in which there is no other imposed zonal
1828 scale. Assume that the wind stress is purely zonal, and is switched on at $t = 0$ and then held
1829 constant, as in the base case. The Stage 2 zonal flow u_{S2} then grows linearly with time until the
1830 arrival of the eastern boundary wave. How does the then extant zonal flow compare with Sverdrup
1831 zonal flow? In general, the $u_{S2}(x, y)$ current is not the same as the steady state Sverdrup zonal
1832 flow, since the former depends upon $\partial^2(\tau/f)/\partial y^2$ and not $f^{-1}\partial^2\tau/\partial y^2$ as does the Sverdrup zonal
1833 current (and see Figs. 10 and 13). To remedy this, suppose that the y scale of the wind stress field is
1834 much less than R_E . This will result from setting $n = 6$ in the wind stress Eqn. (27), and thus
1835 $\tau^x(y) \propto \sin(6\pi y/L)$. Can you show that the zonal transport at $t = T_{ebw}$ is then approximated well

1836 by

$$1837 \quad hu_{S2}(t = T_{ebw}) \approx -\frac{(L-x)}{\rho_o\beta} \frac{\partial^2 \tau^x}{\partial y^2} = \frac{\partial \Psi_{Sv}}{\partial y},$$

1838 where the last step used Eqn. (61). Why does the zonal transport increases in magnitude in
1839 proportion to distance from the eastern boundary, $L - x$?

1840 11. Can you show that the vorticity balance form of the Ekman number appropriate to a western
1841 boundary current, Eqn. (66), is related to the usual, momentum balance form $E = r/f$, by

$$1842 \quad E_Q = E \frac{L\tau}{R_d}.$$

1843

1844 12. Assume a steady, wind-driven circulation. What would you expect to follow if the wind stress
1845 suddenly vanished? Check your intuition against www.whoi.edu/jpweb/wind-off.mp4 Now
1846 Imagine an experiment in which the wind stress is spatially uniform over the entire basin, and
1847 northward. What would you expect for Stage 2 and Stage 3? (Major hint: consider the stress curl.)
1848 What is the steady response? Once you have formed your answer, take a look at the circulation
1849 computed from such an experiment shown in Fig. (31, lower).

Index

- 1850 beta effect, 14

- 1851 eastern boundary
 - 1852 blocking, 43
 - 1853 Rossby wave, 43
- 1854 Ekman pumping and suction, 38

- 1855 gyre
 - 1856 exchange, 52

- 1857 Rossby wave
 - 1858 arrested, 70
 - 1859 long wave speed, 44

- 1860 seasonality
 - 1861 subpolar and subtropical gyres, 9
 - 1862 tropical, 9
- 1863 shallow water model equations, 25
- 1864 Stokes drag, 24
- 1865 streamfunction, 54
- 1866 Sverdrup q balance, 57
- 1867 Sverdrup relation
 - 1868 eastern boundary effect, 97
 - 1869 range of validity, 11
 - 1870 thickness balance, 69
- 1871 Sverdrup transport, 10
 - 1872 streamfunction, 55

- 1873 thermocline, 1

- 1874 western boundary current, 59
 - 1875 width, 60
- 1876 western intensification, 8
- 1877 wind stress, 22
 - 1878 seasonality, 71

- 1879 zonal boundary region
 - 1880 q balance, 61
 - 1881 width, 62